Design and Development of Two Terminal Electrical Devices for Lighting and Sensing

A dissertation submitted in partial fulfilment of requirements

for the degree of

Doctor of Philosophy

by

Ramesh Babu Yathirajula

Roll No. 156153002

Centre for Nanotechnology

Indian Institute of Technology Guwahati

Guwahati-781039, Assam, India

March 2024

Statement

I do hereby declare that the work incorporated in this thesis entitled, "**Design and Development of Two Terminal Electrical Devices for Lighting and Sensing**" is the result of investigations carried out by me under the guidance of Prof. Parameswar Krishnan Iyer, at the Centre for Nanotechnology, Indian Institute of Technology Guwahati, Guwahati, Assam, India.

In keeping with the general practice of reporting scientific observations, due acknowledgements have been made wherever the work described is based on the findings of other investigators. I further declare that this work has not been submitted in part or full to any other university or institute for the award of any degree or diploma.

IIT Guwahati
March 2024

Ramesh Babu Yathirajula

Dr. Parameswar K. Iyer
Professor, Department of Chemistry and Center for Nanotechnology
Indian Institute of Technology Guwahati
Guwahati-781039, Assam, India
http://www.iitg.ac.in/chemistry/fac/pki/

Phone : +91-361-2582314
Fax : +91-361-2690762
:+91-361-2582349
E-mail : pki@iitg.ac.in

Certificate

This is to certify that the work included in this thesis entitled "**Design and Development of Two Terminal Electrical Devices for Lighting and Sensing**" by Mr. Ramesh Babu Yathirajula, Centre for Nanotechnology, Indian Institute of Technology Guwahati has been carried out under my supervision. I further certify that this work has not been submitted to any other University or Institution in part or full for the award of any degree or diploma.

IIT Guwahati
March 2024

Parameswar Krishnan Iyer
Thesis supervisor
Department of Chemistry
Indian Institute of Technology Guwahati
Guwahati – 781039, Assam, India

Table of Contents

Acknowledgement		i
Thesis Synopsis		iv
Chapter 1: Introduction		**1-24**
1.1	Introduction	3
1.2	Perovskite Light Emitting Diodes (PeLEDs)	5
	1.2.1 History of Perovskite LED	5
	1.2.2 Working principle of Perovskite LED	6
	1.2.3 Structure of Perovskite LED	8
1.3	Parameters to define Perovskite LED performance	10
1.4	Conjugated polymer-based sensors	11
	1.4.1 Introduction	11
	1.4.2 Sensors	12
	1.4.3 Conjugated polymers for electrical sensors	13
	1.4.4 Working principle of chemiresistive sensors	14
1.5	Parameters to define electrical sensor performance	15
1.6	Objectives and summary of the thesis work	16
References		19
Chapter 2: Modulating carrier injection through rational control of hole transport layer for perovskite light emitting diodes		**25-48**
Abstract		27
2.1	Overview	28
2.2	Experimental Section	30
	2.2.1 Materials	30
	2.2.2 Device Fabrication	30
	2.2.3 Characterization	31
2.3	Results and Discussions	31
2.4	Conclusions	38
References		40
Appendix		45
Chapter 3: Dual hole transport layer facilitated efficient perovskite light emitting diode		**49-71**
Abstract		51
3.1	Overview	52
3.2	Experimental Section	54
	3.2.1 Materials	54
	3.2.2 Device Fabrication	54
	3.2.3 Characterization	55
3.3	Results and Discussions	55
3.4	Conclusions	62

References		63
Appendix		66
Chapter 4: Conjugated polymer-based electrical Ammonia sensor with Schottky barrier diode modelling		**72-94**
Abstract		74
4.1	Overview	75
4.2	Experimental Section	77
	4.2.1 Materials	77
	4.2.2 Synthesis of PFIM	77
	4.2.3 Device Fabrication with Photolithography	78
	4.2.4 Characterization	79
4.3	Results and Discussions	79
4.4	Conclusions	87
References		88
Appendix		92
Chapter 5: Printed conjugated polymer based CO electrical sensor with schottky barrier diode mathematical modelling		**95-116**
Abstract		97
5.1	Overview	98
5.2	Experimental Section	100
	5.2.1 Materials	100
	5.2.2 Synthesis of PFPT	100
	5.2.3 Device Fabrication with Material Printing System (MPS)	101
	5.2.4 Characterization	101
5.3	Results and Discussions	102
5.4	Conclusions	109
References		111
Appendix		113
Outcomes		117
Conferences & Workshops		119

Acknowledgement

I am immensely grateful to everyone who has contributed to the completion of this thesis. Many individuals have supported me on this remarkable journey, and I wish to acknowledge each one of them from the bottom of my heart.

First and foremost, I extend my deepest gratitude to my supervisor and mentor, Prof. Parameswar Krishnan Iyer, for providing me with the precious opportunity to work in his group. His continuous support, valuable suggestions, scientific guidance, deep insights, and motivation have encouraged me to take up tasks and introduced me to a field about which I knew little. I am fortunate to have him as my guide, and I thank him for trusting me and giving me the freedom to choose the direction of my research.

Besides my supervisor, I am deeply indebted to my doctoral committee members, Prof. Harshal B. Nemade, Dr. Arun Tej Mallajosyula, and Dr. Partho S. G. Pattader, for regularly assessing my research work. Their invaluable suggestions and critical comments during all my seminars have helped me broaden my research from various perspectives and improve my thesis.

I sincerely express my gratitude to all my teachers, especially Mr. T. Jannadha Rao, Mr. L. Jagga Rao, Mr. Abdul Rahaman, Mr. Applanaidu, and all my teachers at Sir C. R. Reddy College of Engineering, Eluru, as well as JNTU, Kakinada, for instilling good values and knowledge in me.

I am also thankful to all the research scholars and staff of the Center for Nanotechnology and Department of Chemistry, IIT Guwahati for their kind cooperation and support. Further, I am also grateful to the Centre for Nanotechnology and Central Instrument Facility, IIT Guwahati for allowing me access to their facility for various experiments as required. I am indebted to the staff of the Student Affairs, Academic Affairs and Finance sections of IIT Guwahati for their advice and help in their respective roles.

I had the best of times working with Adil Ji and Dipjyoti Ji who were my core research team members. Both of them deserve the best and utmost respect for their hard work, diligence and indispensable input into the overall research work. Further, the research experience gathered along with Arvin, Suresh, Bhim, Ashish, Radha, Anwesha, Rabi, Retwik, and Maimur is also worth mentioning.

I would also like to acknowledge all my other lab mates including Subba Rao bhaiya, Sameer, Priyanka Mam, Dip, Anamika Dey, Anamika Kalita, Gopi, Sayan, Rahul, Raman Ji, Subrata, Nehal, Paromita, Biki, Anita, Raj, Priyam, Debika, Tamal, Soumalya, Kavita, Mayur, Sushant, Geetmani, Himangshu, Tapashi, Ramkrishna, Deepak, Manab, Mizanur, Dhiraj, Mirinalini and Antim for their timely assistance and support. I would also like to thank each one of them for creating a pleasant and vibrant laboratory atmosphere and making my days memorable.

I was also fortunate to be working in the Organic Electronics Laboratory of IIT Guwahati which houses all the sophisticated instruments. I have learnt a lot to keep these instruments in working conditions through proper maintenance. During all the maintenance activities, I have received ample support from various engineers. I would like to thank Mr. R. K. Tripathi, RVL Scientific & Engineering Pvt. Ltd., Mr. T. P. Kundu, IKA India Pvt. Ltd., and Mr. M. Nandan, Bat-Sol Equipments & Technology.

I extend my sincere thanks to my IIT Guwahati friends Nirmal, Thomas, Vimal, Himangshu Gogoi, Abinash, and Atanu. I would also like to thank my friends K.V. Ramana Rao, Ch. Jay Dev, B. S. Kamal, M. Suresh, M. Raja Rao, and M. Lakshmi from the bottom of my heart. All the discussions beyond work with all these friends helped me focus more on the research. Thank you, guys, for helping me right from the beginning of knowing each other and providing all the moral support and time.

Finally, I would like to express admiration towards my spouse, Hemalatha, and my children Rushi and Unnathi who have always supported me, especially in the tough phases of my life. At the end, I want to thank my parents, younger brother and sister, and my entire family for their prayers, sacrifices, and struggles. It is because of them that I am able to live my dream and complete my higher education from a prestigious institute. They have always given me the strength to chase my dreams, which was immensely needed.

I express gratitude towards each individual for extending their support, encouragement and remembering me in their prayers.

Ramesh Babu Yathirajala

[This page was intentionally left blank]

Synopsis

The content of this synopsis report entitled **"Design and Development of Two Terminal Electrical Devices for Lighting and Sensing"** is divided into five chapters. *Chapter1* give brief introduction about the respective research area where the scope and significance of the subsequent chapters are discussed. *Chapter 2* discussed the stable $MAPbBr_3$-based Perovskite LEDs (PeLEDs) with high brightness is fabricated by strategically selecting the Hole Transport Layer (HTL) for efficient hole injection and charge balance in the emissive layer. The crucial effects of hole injection barrier and the hole transport properties of different HTLs on the charge transport, luminescence and current efficiency are presented. *Chapter 3* discussed the simple method by using PEDOT: PSS and NPD as dual HTLs, and we are able to demonstrate that a PeLED based on PEDOT: PSS/NPD will perform the best and offer a high efficiency PeLED. Through careful dual HTL selection, high brightness PeLEDs based on $MAPbBr_3$ are fabricated, enabling efficient hole injection and charge balance in the emissive layer. *Chapter 4* discussed the fabrication of PFIM polymer based electrical ammonia sensor with lithography technique and have achieved a significant milestone by developing a good sensitive ammonia sensor capable of detecting minute concentrations (LOD) down to 87.3 parts per billion (ppb) at room temperature. This sensor's selectivity is thoroughly assessed, demonstrated its robust performance. It is showed remarkable response (%) when detecting ammonia, highlighting its efficacy in this specific application with mathematical modeling. *Chapter 5* discussed fabrication and characterization of printed electrical CO sensor with good transient response, and this sensor capable of detecting minute concentrations (LOD) down to 0.047 parts per billion (ppb) at room temperature and also studied the mathematical modeling. And subsequently the senor's response and recovery times are calculated from transient studies.

Chapter 1: Introduction

At the peak of demand for energy conservation, the light emitting diodes (LEDs) have become a power savior compared to the incandescent and fluorescence technologies. Both inorganic and organic LEDs have been well explored for various applications including displays, lighting, communications and laser sources. However, the inorganic LEDS require high temperature and the organic ones offer very low quantum efficiency. Recently, perovskites after gaining much importance in the field of photovoltaics are being now explored for LED applications as well. The material offers series of advantages such as high crystallinity, direct bandgap, easily color tunable, long carrier lifetimes, high quantum yield, and higher

carrier mobilities. It offers good film forming property making it suitable for fabrication of perovskite LED (PLED) through solution-processing technique even on flexible and large area substrates The researches on PLEDs have now garnered some pace and quantum efficiency of over 23% has been achieved. Further significant development has been taking place to address the short lifetime of the PLEDs through various methodologies including incorporation of hydrophobic interlayer.

Two types of perovskite materials are being used in the fabrication of PLEDs: (i) all inorganic such as cesium lead bromide ($CsPbBr_3$) and (ii) hybrid organic inorganic perovskite (HOIP) such as methyl ammonium lead bromide ($MAPbBr_3$). Among, these two, the all inorganic PLED has impacted more compared to the HOIP. However, at the same time the processing temperature of the same is much higher. Hence, significant developments are being carried out using HOIP PLEDs, especially with $MAPbBr_3$. Further, $MAPbBr_3$ facilitates easy crystallization compared to other perovskite having similar opto-electronic properties. The defects present in the perovskite layer are passivated using various organic and inorganic additives similar to ones done for solar cell application. This has resulted in better perovskite film with improved coverage through uniform nucleation. The passivation of defect traps on the perovskite surface is also performed by coating these materials on top of the emissive layer to improve the charge injection Further, anti-solvent dripping of low boiling point solvents has been also performed to control the crystallization kinetics of the perovskite layer to obtain smooth films. The anti-solvents are expected to remove the excess processing solvents in the perovskite films that prevent the device degradation. Another unique method of nano-crystal pinning has been developed where organic additives are added along with the anti-solvent to not only remove the excess solvents but also passivate the defects of the surface of the perovskite films. It is well-known that any surface defects or non-smooth film coverage of the perovskite leads to serious leakage problem leading to mitigated device performance and stability.

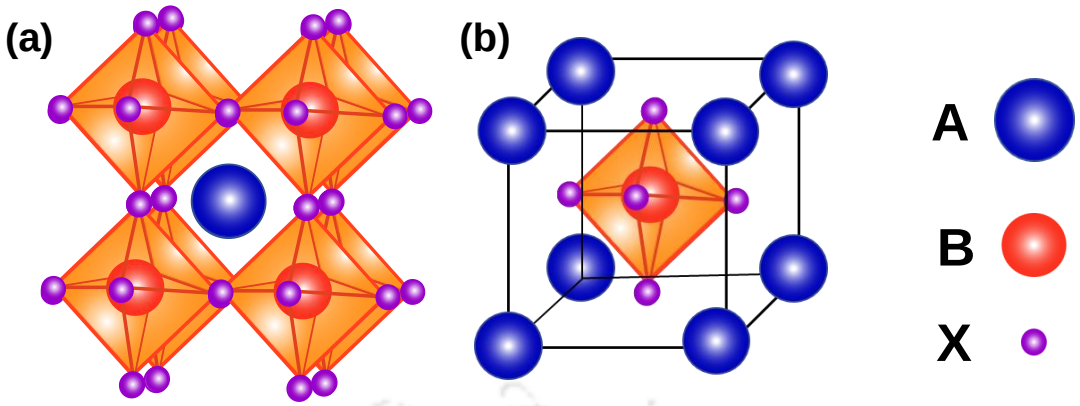

Figure 1: Scheme of perovskite crystal unit cell (a) A-cation centered and (b) B-cation centered.

Figure 1, illustrates the perovskite crystal unit cell, these perovskite materials shows the good crystallinity in perovskite emissive layers, which will enhances the mobilities in the LED emissive layer compared to organic semi-conductive EML. To further confirm the crystallinity of the perovskite emissive layer coated on top of various HTLs, X-ray diffraction (XRD) study is performed (Fig. 4e). In cubic $MAPbBr_3$, the XRD spectra exhibits two distinct and strong diffraction peaks at 14.95°, 30.15° and 33.90° and which correspond to (100), (200) and (210) planes, respectively.

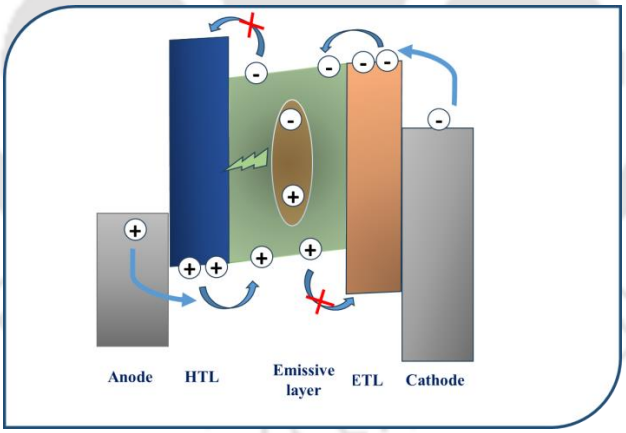

Figure 2: Schematic illustration of working principle of PeLED.

Figure 2, illustrates the working principle of perovskite LED with multiple layers to achieve the better radiative recombination at inside the emissive layer. Perovskite emissive layer gets lit up by radiative recombination of high energy electrons residing at conduction band and low energy holes at valance band. The energy gap between these two bands dictates the colour of LEDs. A LED consists of several layers which make radiative combination of electron and hole possible. Hence role of HTL (hole transporting layer) which is adjacent to emissive layer and

anode is very important for device performance. Surface morphology of HTL also influence the hole injection as well as active layer morphology. Efficient hole injection and electron blocking by hole transport layers improves the LED performance. Role of the interfacial engineering is come into play to obtain the improved LED device performance.

Introduction of conjugated polymers:

Conjugated polymers (CPs) are categorised as a unique type of organic macromolecules formed by alternate σ (single) bond and highly delocalized π (multiple) bond along its backbone. The research on CPs began in the late 1970's and has gained a tremendous attention since the discovery of polyacetylene's electrical properties after halogen doping. After 23 years of progress, such an initial step of switching plastic insulator like polyacetylene into an electrically conductive metal was honoured in 2000 with Novel Prize in Chemistry jointly to the three pioneered Scientist Alan J. Heeger, Alan G. Mac Diamond, and Hideki Shirakawa. Since then, there have been massive advancement in the interdisciplinary research of material science, biological science and optoelectronic devices.

Conjugated polymers (CPs) are gaining popularity as a promising material for sensing and biological application due its high absorption coefficient, intense emission, super sensitivity, low detection limits, ease of solution process ability etc.

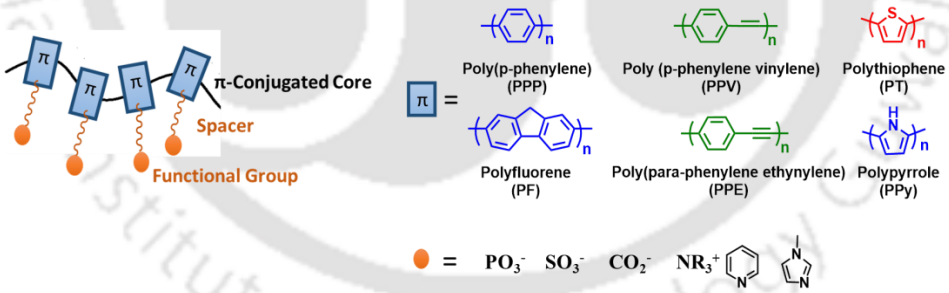

Figure 3: Chemical structures of some well-known conjugated polymer systems.

CP-based sensors with signal amplification features can be implemented into a variety of transduction schemes depending on the need or requirement. CP with diverse type of backbone structures have been extensively explored; the most prominent type includes poly (p-phenylene) (PPP), poly(p-phenylene vinylene) (PPV), polythiophene (PT), polyfluorene (PF), polypyrrole (PPy), poly(para-phenylene ethynylene) (PPE), etc. (Figure 3) The incorporation of functional groups at the side chain of the CP backbone imparts solubility in a high dielectric

solvent such as water while tuning the chemical interaction with the analyte of interest.

Applications of conjugated polymers as sensors:

In recent years CPs with different conjugated structures and side-chain functionalities have been tremendously explored as sensory materials for various chemical and biological species such as metal ions, explosives, small biomolecules, proteins, DNA, etc. CP-based sensors are implemented into a variety of signal transduction such as fluorometric sensors, colorimetric, conductometric, potentiometric, and amperometric sensors, etc. Due to amplified response, the CP-based sensor device exhibits a low detection limit in the range of ppb to ppt level. The enthralling properties such as transport of charge, rate of energy migration, and electrical conductivity make the CPs, very attractive for chemo and biosensing applications.

Chapter 2: Modulation of carrier injection through rational control of hole transport layer for perovskite light emitting diodes

Chapter 2 discusses the fabrication and characterization of single hole transporting layers (HTLs) based $MAPbBr_3$-based Perovskite LEDs. In this chapter, four hole transporting layers (HTLs) have been used to regulate the hole injection in the emissive layer. The HTLs have varying HOMO levels aligning with the work function of FTO and HOMO of the emissive layer. Among the four HTLs, NPD-based perovskite LED device demonstrated the best performance with highest brightness of 24343 cd m^{-2}, current efficiency of 16.2 cd A^{-1}, and turn-on voltage of 4.7 V. The main reason for such improved results was the well-match HOMO of NPD with both the anode and emissive layer supporting enhanced hole injection. Both the photoluminescence and electroluminescence studies confirm pure green emission with CIE coordinates (0.22, 0.75). Best quality film morphology for NPD-based perovskite film supported efficient transport of the charges. The crystallinity of the NPD-based perovskite film was also found to be optimum. Finally, stability of the working PLEDs is tested and superior stability with 79% of the retention of initial brightness is observed for NPD-based device. (Figure 4)

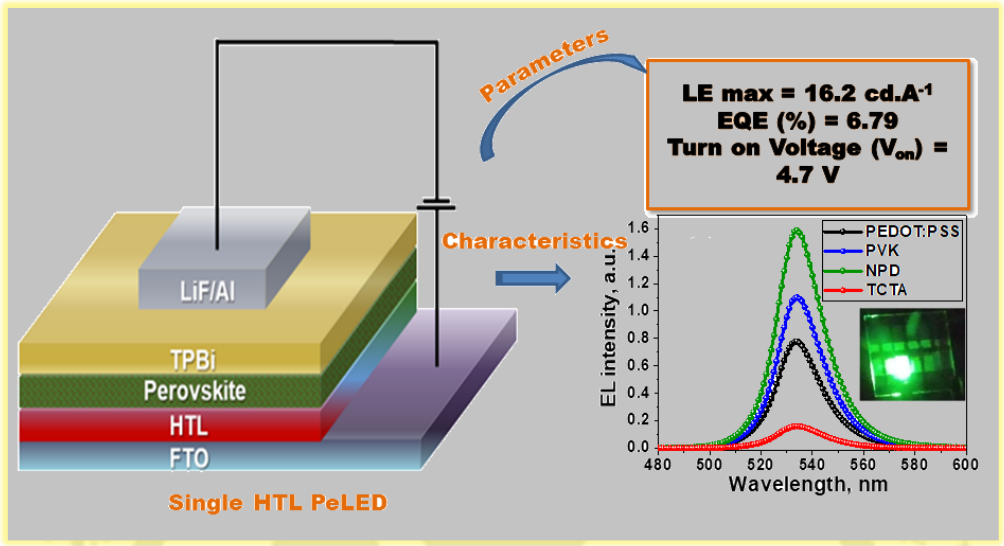

Figure 4: Schematic representation of rational study of single HTL based $MAPbBr_3$ LED.

Chapter 3: Dual hole transport layer facilitated efficient perovskite light emitting diodes

Chapter 3 discusses the fabrication and characterization of dual hole transporting layers (HTLs) based $MAPbBr_3$-based Perovskite LEDs. In this chapter, a straightforward method for fabricating dual hole transport layers (HTLs) in green-emitting perovskite light emitting diodes (PeLEDs), which significantly helps and charge balance in the emissive layer (EML). By achieving charge balance in the emissive layer, with well-matched energy levels, and lowered charge injection barrier of the transport layers, maximum radiative recombination can be obtained (HTLs). The varying HOMO levels of the HTLs used in the device are in alignment with the work function of the FTO and HOMO of the emissive layer. The PEDOT:PSS/NPD-based PeLED device showed outstanding performance with a maximum brightness of 19625 cd m−2, the highest current efficiency of 19.2 cd A-1, and turn-on voltage of 3.8 V among the all three HTL combination. The reason for these higher results was the well-match HOMO of PEDOT:PSS and NPD with both the anode and emissive layer facilitating better hole injection and charge balance. CIE coordinates (0.22, 0.74) for pure green emission are supported by studies utilizing photoluminescence and electroluminescence. The best film morphology and

crystallinity with less pinholes were found in perovskite films made on top of PEDOT:PSS/NPD, which allowed for efficient charge transport. (Figure 5)

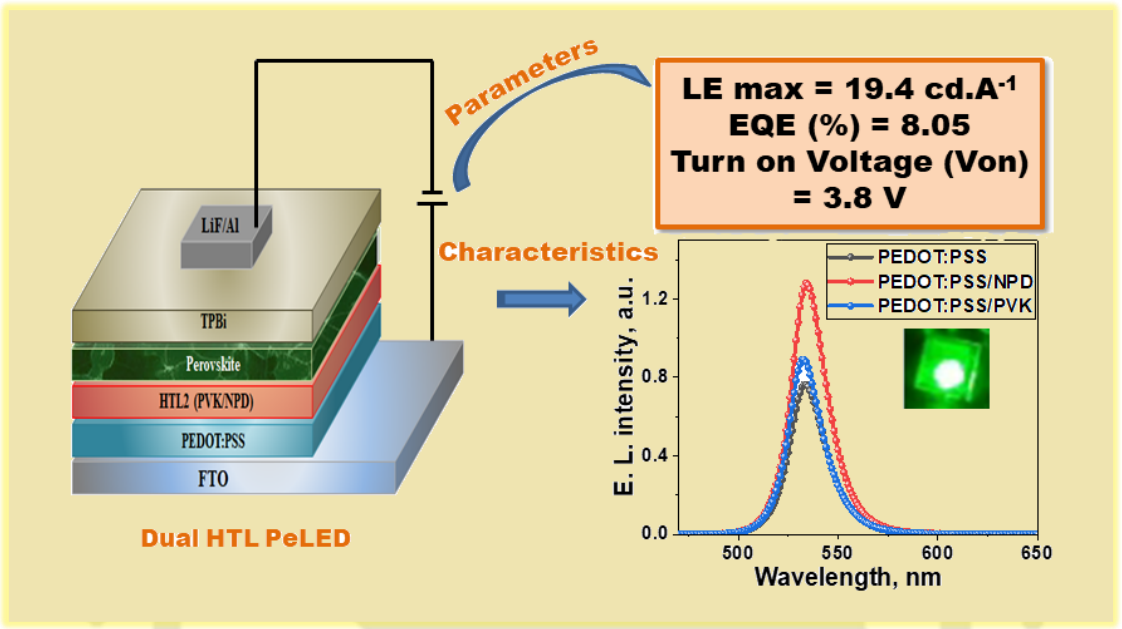

Figure5: Schematic representation of rational study of dual HTL based $MAPbBr_3$ LED.

Chapter 4: Conjugated polymer PFIM-based ammonia electrical sensor fabricated using lithography and Schottky barrier diode modeling

Chapter 4 discusses the conjugated polymer PFIM based ammonia sensor fabricated using photo-lithography technique Organic semiconductors can significantly increase the performance of photolithography based electrical sensing device. In this chapter, we describe a unique PFIM polymer-based two-terminal electrical device for ammonia detection. The gas sensing device is fabricated on a silicon wafer support, with a 4.7 µm length micro-channel separating the two aluminium (Al) electrodes. Drop-casting is done, the active material PFIM onto the micro-channel connecting the two electrodes. In selectivity testing, the PFIM effectively distinguishes ammonia from a pool of volatile organic compounds (VOCs). Response of 64.5% and 87.3 ppb Limit of Detection (LOD), the PFIM had the best response with ammonia. Additionally, we are performed the humidity and zeta potential studies. Moreover, utilizing mathematical modeling, the photolithography schottky barrier diode displayed a remarkable schottky barrier height of 2.39 eV, an ideality factor of 1.92, and a series resistance of 625 kΩ at ambient temperature. This increases the two terminal sensor's electrical performance. (Figure 6)

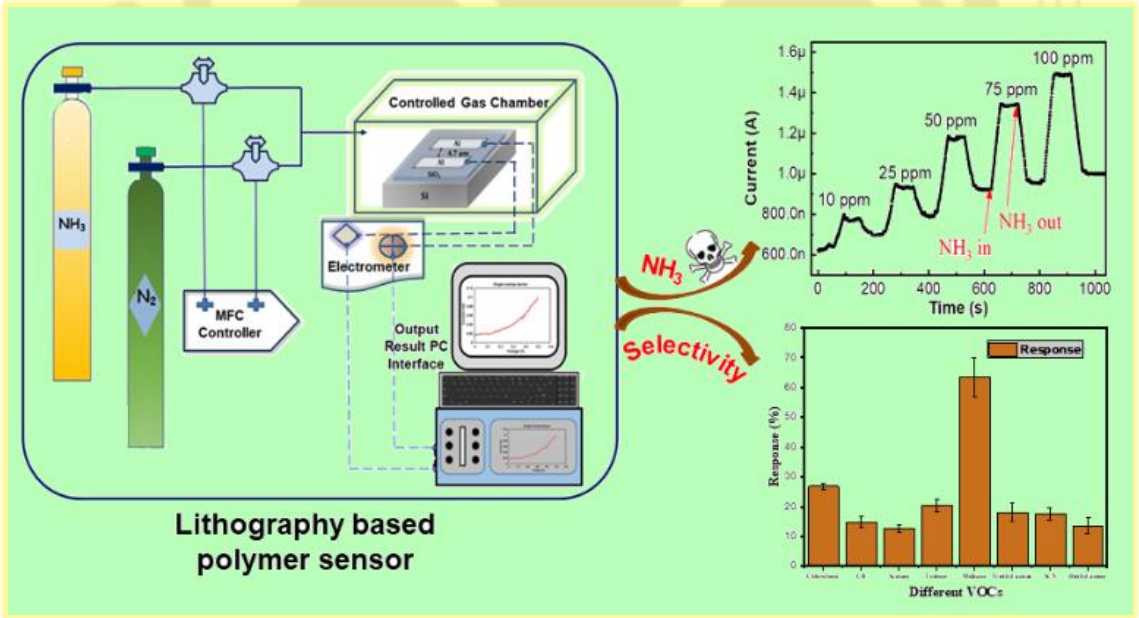

Figure 6: Schematic representation sensing and selectivity studies of lithography based polymer ammonia sensor.

Chapter 5: Printed PFPT conjugated polymer based CO electrical sensor with Schottky diode mathematical modeling

Chapter 5 discusses the conjugated polymer PFPT based electrical CO sensor fabricated using printing technique. Organic semiconductors can significantly increase the performance of printing based electrical sensing device; in future easily extend to flexible and wearable sensors. In this chapter, we describe a unique PFPT polymer-based two-terminal electrical device for CO detection. The gas sensing device is fabricated on a silicon wafer support, with a 15 µm length micro-channel separating the two AgNP electrodes. Drop-casting is done, the active material PFPT onto the micro-channel connecting the two electrodes. In selectivity testing, the PFPT effectively distinguishes CO from a pool of volatile organic compounds (VOCs) and gases. Response of 43.2% and 0.047 ppb Limit of Detection (LOD), the PFPT had the best response with CO. Additionally, we are performed the AFM and EIS studies with and without analyte gas (CO). Moreover, utilizing mathematical modeling, the printed schottky barrier diode displayed a remarkable schottky barrier height of 0.57 eV, an ideality factor of 1.7, and a series resistance of 5978 kΩ at ambient temperature. This increases the two terminal sensor's electrical performance. (Figure 7)

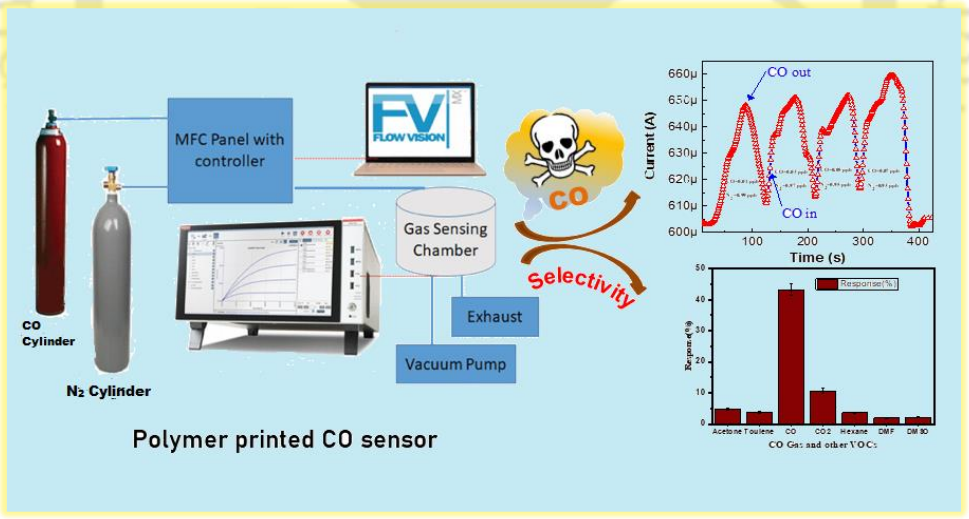

Figure 7: Schematic representation sensing and selectivity studies of printed PFPT polymer based CO sensor.

Thesis Overview and Future Perspective

In conclusion, our research encompassed the fabrication and characterization of various devices, including single Hole Transporting Layer (HTL) $MAPbBr_3$ perovskite LEDs and dual HTL $MAPbBr_3$ perovskite LEDs. In both investigations, the careful selection of HTLs aimed to achieve superior energy alignment with the anode and Emissive Layer (EML). The comprehensive analysis covered various aspects such as electrical characteristics, morphology, topology, crystallinity, and photo-physical properties. The subsequent chapters focused on the development of novel sensors. Firstly, we employed a photo-lithography-based approach to fabricate a PFIM polymer for ammonia detection. Concurrently, we conducted studies on a PFPT polymer for carbon monoxide (CO) sensing. Both studies involved a thorough investigation of humidity effects, zeta potential, topology, and Electrochemical Impedance Spectroscopy (EIS).

Additionally, to enhance our understanding, we incorporated a thermionic emission–based diode current model for mathematical modeling. This enabled us to extract critical parameters such as ideality factor, series resistance, and Schottky barrier height. These insights contribute to a comprehensive understanding of the behaviour and performance of the fabricated devices and sensors, fostering advancements in the field of electronic and sensor technologies.

Moreover, employing the aforementioned approach opens avenues for further advancement, particularly by incorporating amine-based passivation layers and innovative Electron Transport Layers (ETLs) in the realm of Perovskite LED research. This strategic enhancement holds the potential to optimize device performance and efficiency. In the sensor domain, there is untapped potential for improvement by introducing reduced Graphene Oxide (rGO) to augment response and recovery times, along with enhancing overall stability. This modification is anticipated to have a transformative impact across various applications, ultimately contributing to innovations that benefit humanity.

Chapter 1

Introduction

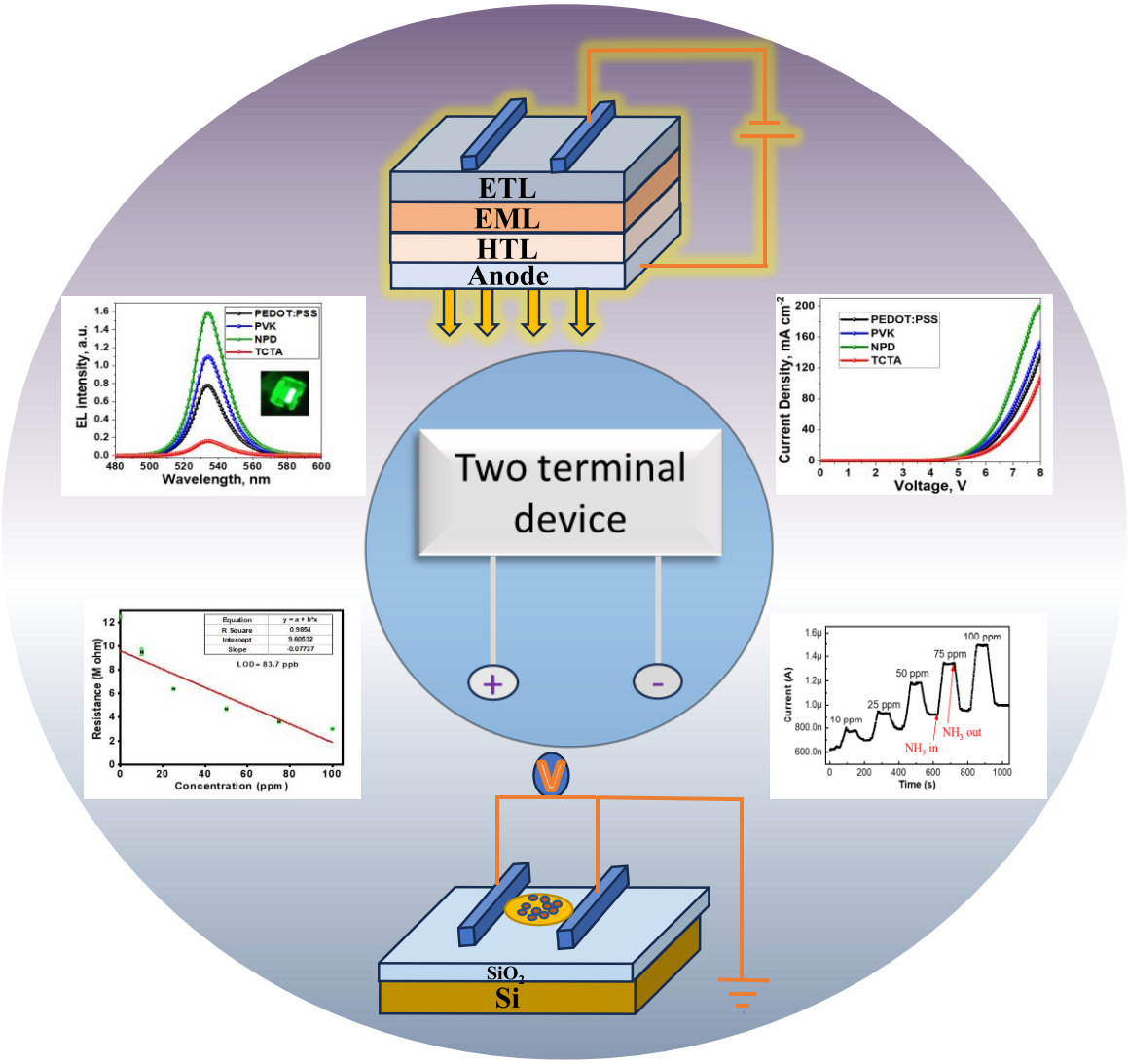

[This page was intentionally left blank]

1.1 Introduction

Two terminal electrical devices are the basic building blocks of electronics, the development of which has revolutionized the field of electronic circuits. The invention of organic materials for these devices has added a new dimension to diodes and other electronic devices by paving the way for low cost, solution-processable, and flexible electronics.[1, 2] Polymers have been present in our daily life for ages and also in electronic devices as insulating materials. However, it was only in the late nineties that the outstanding discovery of oxidation enhanced conductivity of polyacetylene opened a new avenue of organic electronics.[3] Since then, intense research and tremendous progress have been achieved by developing various organic materials, synthesis techniques, and device engineering approaches. An Organic Light Emitting Diode (OLED) is a type of light-emitting diode (LED) where the emissive electroluminescent layer is composed of an organic compound that emits light in response to an electric current. OLEDs are thin, flat, and flexible light sources that can emit light across the visible spectrum. Also, OLEDs offer a compelling combination of high performance and energy efficiency, making them well-suited for a wide range of applications, including smartphones, televisions, automotive displays, wearable devices, and architectural lighting.[4-6] In OLEDs, low photoluminescence yield and quantum efficiencies stem from the amorphous nature of the organic semiconductor emissive layer. However, this challenge has found a solution through the utilization of perovskite materials. Perovskites offer a crystalline structure, providing enhanced efficiency and control over light emission. Additionally, their tunability and cost-effectiveness surpass those of OLEDs, making them a promising alternative for optoelectronic applications.[7,8]. Perovskite LED (PeLED) is a two terminal device where the perovskite emissive layer sandwiched between anode and cathode. When an electric current is applied to the device, it stimulates the perovskite material to emit light. Perovskite LEDs have shown promising performance in terms of high efficiency, narrow emission spectra, and tunable emission colors. **(Figure 1.1)** Tremendous research is carried out on increasing the efficiency and stability of PeLEDs.[9,10] Recent, research in PeLEDs are driven by the goal of addressing key technical challenges and unlocking the full potential of this emerging technology for a wide range of applications, including displays, lighting, and optoelectronic devices. PeLEDs are an emerging technology with promising applications across various fields. Some potential applications of PeLEDs include, display technology, solid-state lighting,

biomedical imaging, visible light communication (VLC), wearable electronics, and automotive lighting.[11-15] Research is already in progress for PeLEDs-based lasers and optical sensors paving the way for the energy-efficient fabrication of electronic circuits.

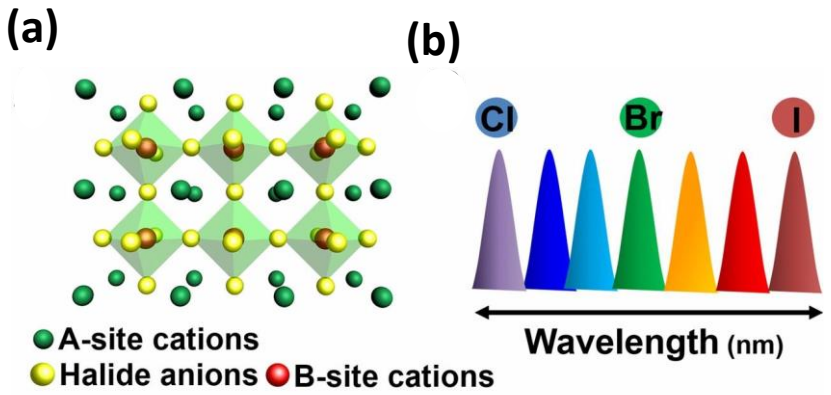

Figure1.1: (a) Schematic illustration of perovskite crystal structure and (b) schematic of emission of metal halide perovskites. The figure is reprinted (adapted) with permission from Ref. 10. Copyright 2016 PNAS.

Conjugated polymer (CP)-based gas and volatile organic compounds (VOCs) sensors utilize the unique properties of CPs to detect and analyze various gases and vapors.[16,17] CPs are organic materials with alternating single and double bonds along the polymer chain, resulting in extended π-electron delocalization and semiconducting behavior. These polymers exhibit sensitivity to changes in their environment, including interactions with gas molecules, making them suitable for gas sensing applications.[18,19] CP-based gas sensors offer a combination of high sensitivity, tunability, selectivity, and cost-effectiveness, making them valuable tools for gas detection and monitoring in various industrial, environmental, healthcare, and consumer applications.[20-23]

Ongoing research aims to further optimize sensor performance, stability, and integration capabilities, unlocking new opportunities for sensing technology. CP-based gas sensors can be fabricated in miniaturized formats, allowing for compact sensor designs and integration into small-scale electronic devices. This miniaturization enables the development of wearable sensors, point-of-care diagnostics, and IoT-enabled smart sensors for distributed sensing networks.[24-27] **(Figure 1.2)** Therefore, considering the current demand for printable and energy-efficient electronic devices, improving

selectivity, limit of detection and sensitivity has become one of the most important research topics as they can be implemented in different printed circuit designs.[28,29]

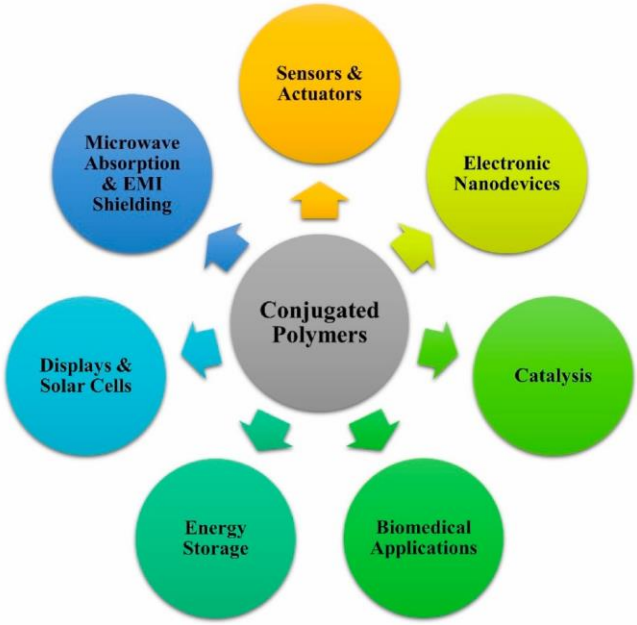

Figure 1.2: Different applications of CPs. The figure is reprinted (adapted) with permission from Ref. 27 Copyright 2022 Elsevier.

1.2 Perovskite Light Emitting Diodes (PeLEDs)

Perovskite LED is a type of LED that utilizes perovskite materials as the active light-emitting layer. Perovskite materials are a class of crystalline materials with a specific crystal structure. These materials have gained significant attention in recent years due to their remarkable optoelectronic properties, including high photoluminescence quantum efficiency, tunable band gap, and ease of fabrication).[30]

1.2.1 History of Perovskite LED

The history of perovskite LEDs is relatively short compared to other types of LEDs, as perovskite-based optoelectronic devices gained significant attention only in the past two decades. The use of metal halide perovskite materials in optoelectronic devices gained prominence following the seminal work by Tsutomu Miyasaka and his team at Toin University of Yokohama in 2009.[31,32] They demonstrated high-efficiency perovskite solar cells, marking a breakthrough in photovoltaic research. Subsequent studies by Henry Snaith at the University of Oxford and others further explored the potential of perovskite

materials in various optoelectronic applications. In 2014, researchers began investigating the possibility of using perovskite materials in LEDs. A team led by Qihua Xiong at Nanyang Technological University reported the first perovskite-based LED with red emission.[33,34] Around the same time, researchers at the University of Cambridge and University of Oxford demonstrated blue-emitting Perovskite LEDs, marking significant progress in the development of PeLEDs Since the initial demonstrations, researchers worldwide have focused on improving the efficiency, stability, and scalability of PeLEDs.[35] Efforts have been made to enhance the luminous efficiency, color purity, and operational stability of PeLEDs through material optimization, device engineering, and fabrication techniques. Significant advancements have been made in achieving green, blue, and even near-infrared emission from PeLEDs, making them increasingly competitive with conventional LED technologies. While PeLEDs have shown great promise in laboratory settings, commercialization efforts are still underway. Several companies and research institutions are actively working on scaling up production, optimizing device performance, and addressing challenges related to stability, reliability, and cost. Collaborative research initiatives, partnerships, and investment in PeLED technology continue to drive innovation and bring PeLEDs closer to commercial viability.[36, 37]

1.2.2 Working principle of Perovskite LED

The conduction mechanism in perovskite materials involves the movement of charge carriers (electrons and holes) through the crystal lattice, which can occur through various processes depending on the specific properties of the material. Perovskite materials are typically semiconductors, meaning their conductivity lies between that of insulators and conductors. Here, the main conduction mechanisms observed in perovskite materials are band conduction, intrinsic charge carrier generation, defect-mediated conduction and ionic conduction. The working principle of a PeLED is based on the electroluminescence phenomenon, where the application of an electric current results in the emission of light from the device. PeLEDs utilize perovskite materials as the emissive layer to generate light efficiently. **(Figure 1.3)**

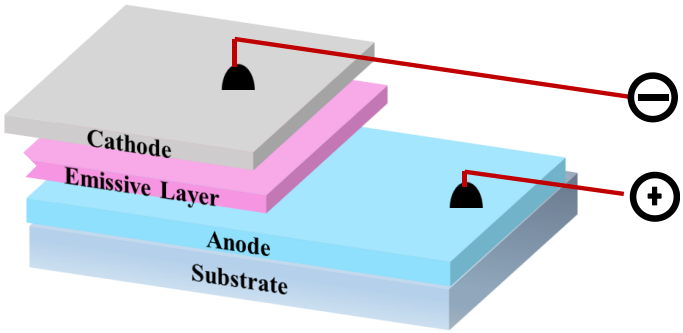

Figure 1.3: Simple PeLED device architecture.

When a forward bias voltage is applied to the PeLED, electrons are injected from the cathode into the electron transporting layer (ETL), while holes are injected from the anode into the hole transporting layer (HTL). These charge carriers (electrons and holes) are then transported through the respective transport layers towards the perovskite emissive layer (EML). In the emissive perovskite layer, electrons and holes are recombine to form excitons (electron-hole pairs), releasing energy in the form of photons. The energy of the emitted photons corresponds to the band gap of the perovskite material, which can be tuned by adjusting its chemical composition. The photons generated by exciton recombination exit the device through the transparent anode, producing visible light.**(Figure 1.4)** The color of the emitted light depends on the band gap of the perovskite material, allowing to produce different colors, including blue, green, red, and near-infrared emissions. The efficiency and color purity of the emitted light in a PeLED depend on various factors, including the properties of the perovskite material, device architecture, charge carrier injection and transport, and external factors such as temperature and operating conditions. Optimization of these parameters is essential for achieving high-efficiency and stable light emission.

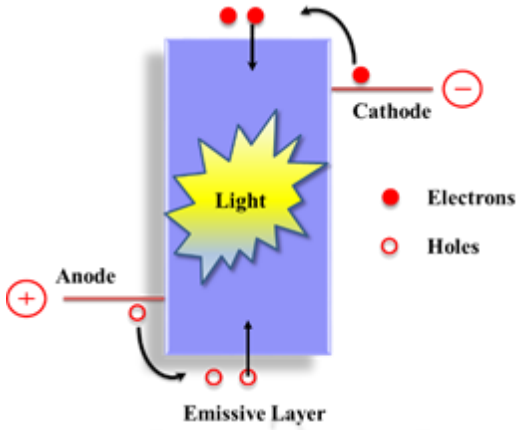

Figure 1.4 The process of light generation in PeLED.

1.2.3 Structure of Perovskite LED

The efficiency of a PeLED usually depends on the number of electron hole pairs that are formed in the emissive layer of a PeLED and decay radiatively. Therefore, the confinement of electrons and holes injected from the cathode and the anode of the devices into its emissive layer has been the main driving force while designing the structure of a PeLED. This has led to the multilayer device structure of PeLEDs where apart from the emissive layer; several other layers are incorporated into the device to confine the injected electrons and holes into the emissive layer. **Figure 1.5,** shows the basic schematic of a multi-layered PeLED.[38]

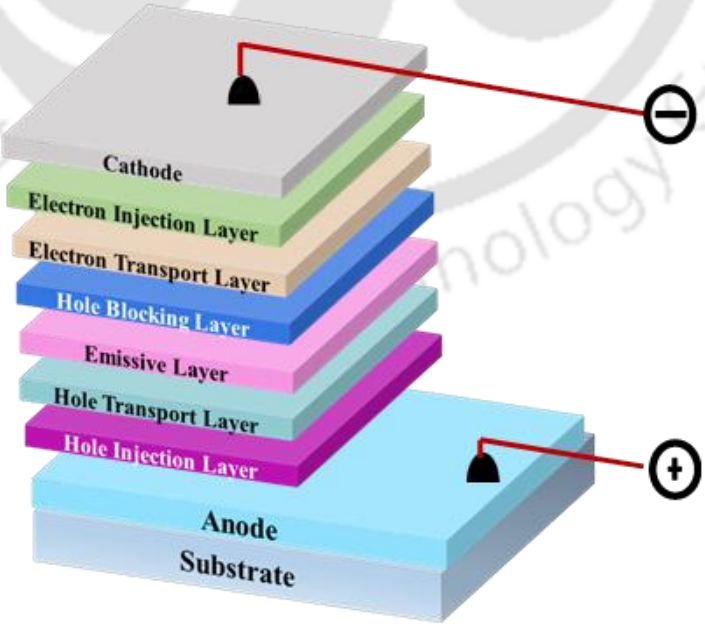

Figure 1.5 The basic schematic of a multi-layered PeLED.

The roles of the different layers of a multi-layered PeLED are described in the following section.

i) Substrate: The main role of the substrate is to provide mechanical support to the device. Usually it is a rigid glass substrate or flexible plastic substrate and most likely made upon of transparent materials.

ii) Anode: In its most common form, the anode of a PeLED should be transparent so that the light generated inside the device due to the exciton decay can escape the device. The primary function of the anode is to inject holes to the organic layers. Usually the material used as anode in PeLED should have high work function, good transparency and low electrical resistivity. Indium tin oxide (ITO) and fluorine-doped tin oxide (FTO) is the most commonly used anode in PeLED.

iii) Hole injection layer (HIL): HIL is inserted between anode and the hole transporting layer (HTL) in order to enhance hole injection from the anode. Strong electron acceptors or p-type doped organic molecules are the most common choices for HIL. Some of the commonly used HIL are Copper phthalocyanine (CuPc), m-MTDATA, etc.

iv) Hole transport layer (HTL): HTL is used to facilitate hole transport into the emissive layer and the materials used as HTL have high hole mobility and low electron mobility. Sometimes this layer also acts as electron blocker and helps confining the electrons in the emissive layer. Some of the commonly used HTL are PEDOT:PSS, PVK, PPV, TPD, NPD, TCTA, etc.

v) Emissive layer (EML): EML is also termed as the active layer of the PeLED and defines the color emitted from the device. The materials used as emissive layer should possess high quantum yield and good charge balance. Here, perovskite layer is used as an EML.

vi) Hole blocking layer (HBL): Hole blocking layer is used to block the hole from flowing towards the cathode and to confine them inside the emissive layer thereby enhancing the recombination and the efficiency. BCP, BPhen, TPBi are some of the widely used hole blocking layer.

vii) Electron transport layer (ETL): ETL is used to facilitate electron transport into the emissive layer and the materials used as ETL have high electron mobility. Usually n-type-doped materials are used in this layer. Alq3 is the most commonly used ETL.

viii) Electron injection layer (EIL): EIL is inserted between cathode and the ETL in order to enhance electron injection from the cathode.

ix) Cathode: The primary function of the cathode is to inject electrons to the organic layers. Usually the material used as anode in OLED should have low work function and high reflectivity. Some of the widely used cathodes are lithium (Li, 2.90 eV), cesium (Cs, 2.14 eV), calcium (Ca, 2.87 eV), magnesium (Mg, 3.66 eV), aluminium (Al, 4.2 eV) etc.

1.3 Parameters to define Perovskite LED performance

The performance of any light source is determined by the following parameters

(a) Efficiency*:* The efficiency of PELEDs is characterized by its luminous efficiency (LE), quantum efficiency (QE), and power efficiency (PE). Of which, LE and QE are important for material evaluation while PE is important for device evaluation and engineering design.

Luminous efficiency (LE): LE is measured in candela per ampere (cd A^{-1}) and obtained on the basis of measurement of luminous intensity (in candela, cd), or luminance (L, in candela per meter square cd m^{-2}) at a given current density (J). i.e.

$$EQE = \frac{Luminous\ intensity}{Current\ density} cdA^{-1}$$

Quantum efficiency (QE): QE of a device is defined as the ratio between generated photons and the injected electron–hole pairs in the device. Of which, photons emitted outside the device are correlated to external quantum efficiency (EQE) while all the photons generated in the device contribute to its internal quantum efficiency (IQE),

$$EQE = \frac{No.of\ photons\ emitted\ outside\ the\ device}{No.of\ e-h\ pair\ injected\ into\ the\ device}$$

$$IQE = \frac{No.of\ photons\ generated\ inside\ the\ device}{No.of\ e-h\ pair\ injected\ into\ the\ device}$$

Power efficiency (PE): This is the most important parameter describing the performance of any light source and is typically measured in lumen per watt. Artificial white light sources are usually evaluated in terms of PE, which is defined as the luminous flux output (in lumen) per input power of the device. It is also termed as luminous efficacy.

$$PE = \frac{luminous\ flux\ output\ (in\ lumen)}{input\ power\ to\ the\ device\ (in\ watt)}\ lmW^{-1}$$

(b) **Commission Internationale de l'Eclairage or International commission on illumination (CIE):** The CIE coordinates describes how the human eye perceives the emission color of any light using a pair of two numbers (x,y). For pure white light, the CIE coordinates are (0.33, 0.33).

(c) **Correlated color temperature (CCT):** The correlated color temperature of a light source is defined as the temperature [usually measured in Kelvin (K)] at which the heated black-body radiator matches the color of the light source. Higher Kelvin temperatures (5,000 K or more) are said to be "cool" (green–blue) colors whereas lower color temperatures (2,700–3,000 K) are called "warm" (yellow–red) colors. Cool-colored light is considered better for visual tasks and warm-colored light is preferred for living spaces because it is considered more flattering to skin tones and clothing.

(d) **Color rendering index (CRI):** The color rendering index (CRI) is a quantitative measure of the ability of a light source to reveal the colors of various objects genuinely in comparison with an ideal or natural light source. It is represented by a number between 0 and 100. Natural sunlight is assumed to have a CRI value of 100. To be used for indoor lighting, a light source should have a minimum CRI value greater than or equal to 80.

1.4 Conjugated polymer-based sensors

1.4.1 Introduction

CPs are typical organic macromolecules that consist of alternative single and double bonds in their backbone chains. The extended delocalized electronic framework along the CP backbone imparts characteristics optoelectronic properties such as absorption or emission of light and transport of electrical charge.[39] The interest in π-CP sparked in the 1970s when three renowned scientists, Alan MacDiarmid, Hideki Shirakawa, and Alan Heeger, discovered for the first time that the electrical conductivity of polyacetylene is increased by 10 million times upon electrochemical doping.[40] This breakthrough research in making plastics electrically conductive led them to win the 2000 Nobel Prize in Chemistry. Since then, CP has become the preferred material choice in the arena of photonics and plastic electronics such as light emitting diode (LED), field effect transistor (FET), photovoltaic cells, and sensors.[41-45] Moreover, they are also explored in

the sensing field as novel and promising materials due to their unique electrochemical and optical properties, good processability, photo/thermal stability, and signal amplification features.[46,47] Depending upon the application, these conjugated backbones can be further modified with different donor acceptor monomers, alkyl side chains, and pendant functional groups to attain desirable optical or electrical properties as well as solubility and processibility.[48]

1.4.2 Sensors

A sensor can be defined as an analytical device that converts physical or chemical information into measurable output signals. Typically, a sensor consists of two main components i.e., recognition unit (receptor) and signaling or transducing unit. The recognition unit detects or responds to the external stimulus via chemical or physical interaction while the transducer unit converts such physical or chemical events into a useful output signal. There is great demand for highly sensitive and selective sensors in various fields such as environmental monitoring, food safety, public health, medical and healthcare products, agriculture industry, and cyber and national security. Although sensors can be classed into various schemes, however, depending on the transduction mechanism, sensors can be categorized into several types such as optical, electrical, magnetic, thermometric, electrochemical and gravimetric, etc. In the case of an optical and electrical sensor, the transducer unit converts physical or chemical response with foreign substance into optical (absorbance or photoluminescence) and electrical signal (conductivity or resistivity) respectively. In the same manner, gravimetric, magnetic, electrochemical, and gravimetric sensors respond to the external stimulus and convert it into the change in the mass, magnetic, thermal, and electrochemical properties of the material, respectively.[49-51] Among various types, optical and electrical sensors are widely explored due to their low cost, high sensitivity, rapid response, and portable features. Moreover, while designing chemo or biosensors, various parameters needs to be considered, such as sensitivity, selectivity, stability, response time, portability and water solubility, etc., depending upon its implementation and application field. In the diverse sensing field, various materials such as metal oxides, carbon nanoparticles, small organic molecules, and polymers are designed and explored for the selective and sensitive detection of environmental and biological species. However, CPs represents promising sensing material due to their outstanding photo-physical properties, chemical and thermal

stabilities, biocompatibility, and amplified signal generation. The basic design strategy for developing a CP-based chemo/biosensor is to connect the recognition element (receptor) with the signaling or transducer unit (conjugated backbone) such that these two components communicate with each other. The analyte triggers variation in measurable properties of the material during the binding event and is quantified as an amplified signal response. Therefore, the functionalization of a conjugated backbone with a specific receptor not only tunes the desired physical property but also improves the solubility, specificity, and sensitivity of CP towards the analyte of interest.[52, 53] A key feature of CP that has received significant attention as a transducer is its ability to transform an analyte-binding event into an amplified optical or electrical signal. This unique signal amplification feature is derived from the efficient migration of charge carriers or exciton throughout the conjugated backbone after analyte receptor chemical interaction.[54]

1.4.3 Conjugated polymers for electrical sensors

To meet the rising demands of portable and wearable sensor for environmental or healthcare monitoring, flexible electronic devices have emerged as one of the most promising technologies that can be used for several applications, such as wireless hazardous gas monitoring, point-of-care devices, on-field explosive sensor, and implantable biomedical devices.[55] Semiconducting polymers are the preferred choice of material in organic electronics due to their tunable opto-electrical properties, facile solution processability, high flexibility, thermal stability, and thin-film forming properties. Moreover, the π-electron distribution of conducting polymer is highly sensitive to the immediate polarization effect caused by proximate molecules or atom.39 This characteristic feature is particularly useful for the development of highly sensitive electrical sensors which transduce chemical interaction into an electrical signal. Generally, electrically conducting polymers are formulated into a variety of transduction schemes/sensor modes such as potentiometric, amperometry, and chemiresistive (conductometric) schemes. However, chemiresistive are most rigorously explored due to their superior sensitivity, ease of fabrication, and faster response time. A chemiresistive sensor typically consists of an organic semiconductor (OSC) as channel material that forms an electrical contact with two or more electrodes deposited on an insulating substrate such as plastic or glass and the analyte of interest is detected based on variation in electrical conductivity or resistivity of organic semiconductor (**Figure 1.6a**).[56,57] The

advantage of chemiresistive sensors over optical or electrochemical-based sensors is their ability to deliver label-free responses using a simple electronic circuit that can be further miniature into smart portable or wearable systems.

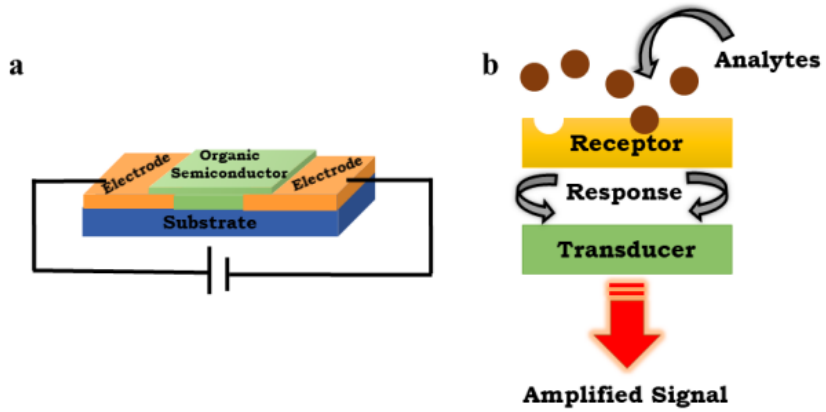

Figure 1.6: (a) Schematic representation of typical chemiresistive sensor and (b) working principle of CP based chemiresistive sensor.

1.4.4 Working principle of chemiresistive sensors

As discussed above, chemiresistive sensor is the simplest form of electrical sensor that integrates organic semiconductor as an active transport layer between a pair of the metal electrode. The sensing response of such a device is greatly related to the change in electrical properties of organic semiconductors after chemical interaction with analyte molecules. The analyte-induced conductivity change can be brought through direct chemical interaction between the semiconductor and analyte such as dipole–dipole, acid–base, hydrogen bonding, coulombic, etc. with the partial transfer of electronic charges between them leading to the variation in density or mobility of charge carriers of semiconductor. Moreover, the adsorption or diffusion of analyte molecules at the surface of organic semiconductors can also result in the trapping of charge carriers at the grain boundaries or an increase in inter grain charge transport resistance and subsequently variation in device current.[58] In the case of CP fabricated chemiresistive sensor, the chemical binding event between the analyte and recognition unit (receptor group) is converted into an amplified change in conductivity/ resistivity by the transducer unit (conjugated backbone), **Figure 1.6 b**. The amplified signal is a collective response of several conjugated units which allow the efficient transport of charges and any molecular

level hindrance in the charge carrier path by external stimuli can obstruct bulk mobility, resulting in higher sensitivity than the small molecule probe.

1.5 Parameters to define electrical sensor performance

The important analytical parameters that define the performance of electrical gas sensor are discussed below.[59-62] These analytical parameters are needed to be assessed prior to practical applications.

a) Sensitivity: The sensitivity is defined as the ability to distinguish small differences in mass or concentration of the target analyte and is generally calculated from the slope of the calibration curve. Hence, the high sensitivity of the sensor corresponds to the large change in output signal by the presence of a very small amount of analyte.

b) Selectivity: Selectivity refers to the capability of the sensor to discriminate the test analyte from other competing or interfering compounds. It is quite difficult to achieve 100% selectivity. However, to achieve selective detection, specific receptor groups should be incorporated while designing the molecular structure of organic semiconductors. The selectivity of the sensor is generally expressed as a percentage of variation in output signal in presence of various interfering analytes.

c) Response and recovery time: The response time is referred to the time taken by the gas sensor to reach 90% of the maximum output signal. Whereas, recovery time is defined as the time needed by a gas sensor to return back from 90% of signal change to its original value after the removal of the target gas.

d) Repeatability: Repeatability refers to the ability of a sensor to generate the same measurement (or response) repeatedly at the same concentration of target analyte under identical conditions.

e) Limit of detection: The limit of detection (LOD) or detection limit is defined as the minimum concentration of test analyte that can be detected; however, it may not necessarily be determined as an exact value. The LOD can be calculated by the equation as shown below:

$\boldsymbol{LOD = 3\sigma / K,}$ Where 'σ' corresponds to the standard deviation of output signal of sensor measured at 'n' time without analyte and 'k' is the slope of a calibration curve.

1.6 Objectives and summary of the thesis work

Considering the need for high performance solution processed perovskite LEDs and electrical sensors for advancement of future electronics, the inspiration of this thesis was the development of high performance, solution processed perovskite LEDs and electrical sensors for application in lighting and detection of toxic vapors and gases. The working chapters of this thesis are divided into four parts. The first part is concentrated on modulation of carrier injection through different single HTLs in PeLED. The second concentrated on modulation of carrier injection through different dual HTLs in PeLED, the third part is the CP based ammonia electrical sensor with Schottky barrier diode modelling and the fourth part is CP based carbon monoxide electrical sensor with Schottky barrier diode modelling. The results obtained during the course of this thesis work are divided into four chapters and in conclusion, thesis summary and future prospects are discussed. A brief overview of the chapters is given below:

Chapter 2 focuses on understanding the rational control of single HTL Perovskite LED. Charge balance in the emissive layer through well-match energy levels and reduced barrier of the transport layers can help to attain maximum radiative recombination. In this work, four-hole transporting layers (HTLs) have been used to regulate the hole injection in the emissive layer. The HTLs have varying HOMO levels aligning with the work function of FTO and HOMO of the emissive layer. Among the four HTLs, NPD-based perovskite LED device demonstrated the best performance with highest brightness of 24343 cd m^{-2}, current efficiency of 16.2 cd A^{-1}, and turn-on voltage of 4.7 V. The main reason for such improved results was the well-match HOMO of NPD with both the anode and emissive layer supporting enhanced hole injection. Both the photoluminescence and electroluminescence studies confirm pure green emission with CIE coordinates (0.22, 0.75). Best quality film morphology for NPD-based perovskite film supported efficient transport of the charges. The crystallinity of the NPD-based perovskite film was also found to be optimum. Finally, stability of the working PLEDs is tested and superior stability with 79% of the retention of initial brightness is observed for NPD-based device.

Chapter 3 focuses on understanding the rational control of dual HTL Perovskite LED. The luminescence and color purity of solution processable perovskite materials have significantly improved, which makes them a promising candidate for high performance lighting technologies. In this paper, we present a straightforward method for fabricating

dual hole transport layers (HTLs) in green-emitting perovskite light emitting diodes (PeLEDs), which significantly helps and charge balance in the emissive layer (EML). By achieving charge balance in the emissive layer, with well-matched energy levels, and lowered charge injection barrier of the transport layers, maximum radiative recombination can be obtained (HTLs). The varying HOMO levels of the HTLs used in the device are in alignment with the work function of the FTO and HOMO of the emissive layer. The PEDOT: PSS/NPD-based PeLED device showed outstanding performance with a maximum brightness of 19625 cd m^{-2}, the highest current efficiency of 19.2 cd A^{-1}, and turn-on voltage of 3.8 V among the all three HTL combination. The reason for these higher results was the well-match HOMO of PEDOT: PSS and NPD with both the anode and emissive layer facilitating better hole injection and charge balance. CIE coordinates (0.22, 0.74) for pure green emission are supported by studies utilizing photoluminescence and electroluminescence. The best film morphology and crystallinity with less pinholes were found in perovskite films made on top of PEDOT:PSS/NPD, which allowed for efficient charge transport.

Chapter 4 focuses on understanding the CP based NH_3 electrical sensor with Schottky barrier diode modelling. Organic semiconductors can significantly increase the performance of photolithography-based electrical sensing devices. In this work, we develop a novel poly(3,3'-((2-(benzo[c][1,2,5]thiadiazol-4-yl)-9H-fluorene-9,9-diyl)bis(hexane-6,1-diyl))bis(1-methyl-1H-imidazol-3-ium)) (PFIM) polymer-based two-terminal electrical device for Ammonia detection. The gas sensing device is fabricated on a silicon wafer using the photo-lithography technique, with a 4.7 µm long micro-channel separating the two Aluminum electrodes. The active material PFIM is drop-cast onto the micro-channel connecting the two electrodes; The PFIM-based sensor is highly selective and effectively distinguishes Ammonia from a pool of VOCs. With a response of 64.5% and a LOD of 87.3 ppb, the PFIM shows the best response with Ammonia. The stability of the sensor is analyzed under varying humidity conditions. The calculation of the Zeta Potential is conducted with and without Ammonia. A thermionic-emission-based transport model has been utilized to extract the important parameters of the photo-lithographically fabricated Schottky barrier diode. The diode shows a barrier height of 0.52 eV, an ideality factor of 1.92, and a series resistance of 75.6 kΩ at ambient temperature.

Chapter 5 focuses on understanding the CP based CO electrical sensor with Schottky barrier diode modelling. The performance of printed electronic devices can be greatly improved by using organic semiconductors. In this study, we describe a novel Poly [(9,9-bis(4'-sulfonatobutyl)fluorene-co-alt-1,4-phenylene) sodium], (PFPT) polymer-based micro cantilever (μC) printed device for the detection of CO. The gas sensing device is fabricated on a silicon wafer support with the micro-channel of ~15 μm length separating the two μC printed AgNP electrodes. The active material PFPT is drop-casted onto the channel connecting the two electrodes. For the selectivity study, the PFPT effectively discriminates CO gas over pool of volatile organic compounds (VOCs) and CO2 gas. With CO, the PFPT exhibits the best response of 43.25% and 0.447 ppb Limit of Detection (LOD). Furthermore, with mathematical modelling, the printed Schottky diode has showed remarkable barrier height of 0.57 eV, an ideality factor of 1.7, and a series resistance of 5978 kΩ at room temperature.

References

(1) N. K. Kumawat, A. Dey, K. L. Narasimhan, D. Kabra, Near infrared to visible electroluminescent diodes based on organometallic Halide perovskites: Structural and optical investigation, ACS Photonics 2 (2015) 349–354.

(2) D. Das, P. Gopikrishna, D. Barman, R. B. Yathirajula, P. K. Iyer, White light emitting diode based on purely organic fluorescent to modern thermally activated delayed fluorescence (TADF) and perovskite materials, Nano Converg. 6 (2019) 31.

(3) N. K. Kumawat, D. Gupta, D. Kabra, Recent advances in metal Halide-based perovskite light-emitting diodes, Energy Technol. 5 (2017) 1734–1749.

(4) W. Faschinger, J. Nürnberger, Green II–VI light emitting diodes with long lifetime on InP substrate, Appl. Phys. Lett. 77 (2000) 187–189.

(5) A. Ren, H. Wang, W. Zhang, J. Wu, Z. Wang, R.V. Penty, I.H. White, Emerging light-emitting diodes for next-generation data communications, Nat. Electron. 4 (2021) 559–572.

(6) R. Garai, R.K. Gupta, A.S. Tanwar, M. Hossain, P.K. Iyer, Conjugated polyelectrolyte-passivated stable perovskite solar cells for efficiency beyond 20%, Chem. Mater. 33 (2021) 5709–5717.

(7) M. A. Afroz, R. K. Gupta, R. Garai, M. Hossain, S. P. Tripathi, P. K. Iyer, Crystallization and grain growth regulation through Lewis acid-base adduct formation in hot cast perovskite-based solar cells, Org. Electron. 74 (2019) 172–178.

(8) G. Pacchioni, Highly efficient perovskite LEDs, Nat. Rev. Mater. 6 (2021) 108–108.

(9) Z. Xiao, R.A. Kerner, L. Zhao, N.L. Tran, K.M. Lee, T.-W. Koh, G.D. Scholes, B.P. Rand, Efficient perovskite light-emitting diodes featuring nanometre-sized crystallites, Nat. Photonics 11 (2017) 108–115.

(10) R. Garai, M.A. Afroz, R.K. Gupta, P.K. Iyer, Efficient trap passivation of MAPbI3 via multifunctional anchoring for high-performance and stable perovskite solar cells, Adv. Sustain. Syst. 4 (2020).

(11) M. Hossain, R. Garai, R.K. Gupta, R.N. Arunagirinathan, P.K. Iyer, Fluoroarene derivative based passivation of perovskite solar cells exhibiting excellent ambient and thermo-stability achieving efficiency >20%, J. Mater. Chem. C Mater. Opt. Electron. Devices 9 (2021) 10406–10413.

(12) A. Choudhury, R.K. Gupta, R. Garai, P.K. Iyer, Tailoring trap density of states through impedance analysis for flexible organic field-effect transistors, Adv. Mater. Interfaces 8 (2021).

(13) S. Chu, W. Chen, Z. Fang, X. Xiao, Y. Liu, J. Chen, J. Huang, Z. Xiao, Large-area and efficient perovskite light-emitting diodes via low-temperature blade-coating, Nat. Commun. 12 (2021) 147.

(14) Y.-H. Kim, S. Kim, A. Kakekhani, J. Park, J. Park, Y.-H. Lee, H. Xu, S. Nagane, R.B. Wexler, D.-H. Kim, S.H. Jo, L. Martínez-Sarti, P. Tan, A. Sadhanala, G.-S. Park, Y.-W. Kim, B. Hu, H.J. Bolink, S. Yoo, R.H. Friend, A.M. Rappe, T.-W. Lee, Comprehensive defect suppression in perovskite nanocrystals for high-efficiency light-emitting diodes, Nat. Photonics 15 (2021) 148–155.

(15) Q. Van Le, H.W. Jang, S.Y. Kim, Recent advances toward high-efficiency Halide perovskite light-emitting diodes: Review and perspective, Small Methods 2 (2018).

(16) X. Zhang, H. Liu, W. Wang, J. Zhang, B. Xu, K.L. Karen, Y. Zheng, S. Liu, S. Chen, K. Wang, X.W. Sun, Hybrid perovskite light-emitting diodes based on perovskite nanocrystals with organic–inorganic mixed cations, Adv. Mater. 29 (2017).

(17) Z. Wei, A. Perumal, R. Su, S. Sushant, J. Xing, Q. Zhang, S.T. Tan, H.V. Demir, Q. Xiong, Solution-processed highly bright and durable cesium lead halide perovskite light-emitting diodes, Nanoscale 8 (2016) 18021–18026.

(18) R.K. Gupta, R. Garai, P.K. Iyer, Dual-passivation strategy for improved ambient stability of perovskite solar cells, ACS Appl. Energy Mater. 4 (2021) 10025–10032.

(19) L.A. Frolova, A.I. Davlethanov, N.N. Dremova, I. Zhidkov, A.F. Akbulatov, E.Z. Kurmaev, S.M. Aldoshin, K.J. Stevenson, P.A. Troshin, Efficient and stable MAPbI3-based perovskite solar cells using polyvinylcarbazole passivation, J. Phys. Chem. Lett. 11 (2020) 6772–6778.

(20) H. Zhang, F. Ye, W. Li, J. Yao, R.S. Gurney, D. Liu, C. Xiong, T. Wang, Bright perovskite light-emitting diodes with improved film morphology and reduced trap density via surface passivation using quaternary ammonium salts, Org. Electron. 67 (2019) 187–193.

(21) H. Zhang, F. Ye, W. Li, R.S. Gurney, D. Liu, C. Xiong, T. Wang, Improved performance of perovskite light-emitting diodes by dual passivation with an ionic additive, ACS Appl. Energy Mater. 2 (2019) 3336–3342.

(22) S. Venkatesan, M. Hasan, J. Kim, N.R. Rady, S. Sohal, E. Neier, Y. Yao, A. Zakhidov, Tailoring nucleation and grain growth by changing the precursor phase ratio for efficient organic lead halide perovskite optoelectronic devices, J. Mater. Chem. C Mater. Opt. Electron. Devices 5 (2017) 10114–10121.

(23) X. Yang, X. Zhang, J. Deng, Z. Chu, Q. Jiang, J. Meng, P. Wang, L. Zhang, Z. Yin, J. You, Efficient green light-emitting diodes based on quasi-two-dimensional composition and phase engineered perovskite with surface passivation, Nat. Commun. 9 (2018) 1–8.

(24) J. Kumar, R. Kumar, K. Frohna, D. Moghe, S.D. Stranks, M. Bag, Unraveling the antisolvent dripping delay effect on the Stranski–Krastanov growth of CH3NH3PbBr3thin films: a facile route for preparing a textured morphology with improved optoelectronic properties, Phys. Chem. Chem. Phys. 22 (2020) 26592–26604.

(25) H. Cho, S.-H. Jeong, M.-H. Park, Y.-H. Kim, C. Wolf, C.-L. Lee, J.H. Heo, A. Sadhanala, N. Myoung, S. Yoo, S.H. Im, R.H. Friend, T.-W. Lee, Overcoming the electroluminescence efficiency limitations of perovskite light-emitting diodes, Science 350 (2015) 1222–1225.

(26) K. Bruening, C.J. Tassone, Antisolvent processing of lead halide perovskite thin films studied by in situ X-ray diffraction, J. Mater. Chem. A Mater. Energy Sustain. 6 (2018) 18865–18870.

(27) Y. Ahn, S. Lee, D.-H. Kwak, M. Kim, D.Y. Kim, J. Kim, Y. Park, M.C. Suh, Improving the efficiency of perovskite light emitting diode using polyvinylpyrrolidone as an interlayer, Appl. Surf. Sci. 507 (2020) 145071.

(28) S.Y. Kim, H. Kang, K. Chang, H.J. Yoon, Case studies on structure–property relations in perovskite light-emitting diodes via interfacial engineering with self-assembled monolayers, ACS Appl. Mater. Interfaces 13 (2021) 31236–31247.

(29) R. Garai, R.K. Gupta, M. Hossain, P.K. Iyer, Surface recrystallized stable 2D–3D graded perovskite solar cells for efficiency beyond 21%, J. Mater. Chem. A Mater. Energy Sustain. 9 (2021) 26069–26076.

(30) D. Das, P. Gopikrishna, R. Narasimhan, A. Singh, A. Dey, P.K. Iyer, White polymer light emitting diodes based on PVK: the effect of the electron injection barrier on transport properties, electroluminescence and controlling the electroplex formation, Phys. Chem. Chem. Phys. 18 (2016) 33077–33084.

(31) S.D. Stranks, R.L.Z. Hoye, D. Di, R.H. Friend, F. Deschler, The physics of light emission in Halide perovskite devices, Adv. Mater. 31 (2019).

(32) B. Zhang, J. Liu, J. Wang, Y. Ruan, X. Ji, K. Xu, C. Chen, H. Wan, L. Miao, J. Jiang, Interface engineering: The Ni(OH) 2 /MoS 2 heterostructure for highly efficient alkaline hydrogen evolution, Nano Energy 37 (2017) 74–80.

(33) Z. Wang, Z. Li, D. Zhou, J. Yu, Low turn-on voltage perovskite light-emitting diodes with methanol treated PEDOT:PSS as hole transport layer, Appl. Phys. Lett. 111 (2017).

(34) Y.-H. Kim, S.-H. Lee, J. Noh, S.-H. Han, Performance and stability of electroluminescent device with self-assembled layers of poly(3,4-ethylenedioxythiophene)–poly(styrenesulfonate) and polyelectrolytes, Thin Solid Films 510 (2006) 305–310.

(35) Y. Zhou, S. Mei, D. Sun, N. Liu, W. Shi, J. Feng, F. Mei, J. Xu, Y. Jiang, X. Cao, Improved efficiency of perovskite light-emitting diodes using a three-step spin-coated CH3NH3PbBr3 emitter and a PEDOT:PSS/MoO3-ammonia composite hole transport layer, Micromachines (Basel) 10 (2019) 459.

(36) W. Wang, Z. Wu, T. Ye, S. Ding, K. Wang, Z. Peng, X.W. Sun, High-performance perovskite light-emitting diodes based on double hole transport layers, J. Mater. Chem. C Mater. Opt. Electron. Devices 9 (2021) 2115–2122.

(37) X. Huang, R. Bäuerle, F. Scherz, J.-N. Tisserant, W. Kowalsky, R. Lovrinčić, G. Hernandez-Sosa, Improved performance of perovskite light-emitting diodes with a NaCl doped PEDOT:PSS hole transport layer, J. Mater. Chem. C Mater. Opt. Electron. Devices 9 (2021) 4344–4350.

(38) Y. Zhou, S. Mei, J. Feng, D. Sun, F. Mei, J. Xu, X. Cao, Effects of PEDOT:PSS:GO composite hole transport layer on the luminescence of perovskite light-emitting diodes, RSC Adv. 10 (2020) 26381–26387.

(39) Heeger, A. J. Semiconducting polymers: the Third Generation. Chem. Soc. Rev. 2010, 39, 2354-2371.

(40) Quade, D. T. M.; Pullen, A. E.; Swager, T. M. Conjugated Polymer-Based Chemical Sensors. Chem. Rev. 2000, 100, 2537-2574.

(41) Facchetti, A. π-Conjugated Polymers for Organic Electronics and Photovoltaic Cell Applications. Chem. Mater. 2011, 23, 733-758.

(42) Gunes, S.; Neugebauer, H.; Sariciftci, N. S. Conjugated Polymer-Based Organic Solar Cells. Chem. Rev. 2007, 107, 1324-1338.

(43) Kraft, A.; Grimsdale, A. C.; Holmes, A. B. Electroluminescent Conjugated Polymers—Seeing Polymers in a New Light. Angew. Chem., Int. Ed. 1998, 37, 402-428.

(44) Torsi, L.; Dodabalapur, A.; Rothberg, L. J.; Fung, A. W. P.; Katz, H. E. Intrinsic Transport Properties and Performance Limits of Organic Field-Effect Transistors. Science1996, 272, 1462-1464.

(45) Sirringhaus, H. Device Physics of Solution-Processed Organic Field-Effect Transistors. Adv. Mater. 2005, 17, 2411-2425.

(46) Thomas, S. W.; Joly, G. D.; Swager, T. M. Chemical Sensors Based on Amplifying Fluorescent Conjugated Polymers. Chem. Rev. 2007, 107, 1339-1386.

(47) Duarte, A.; Pu, K. Y.; Liu, B.; Bazan, G. C. Recent Advances in Conjugated Polyelectrolytes for Emerging Optoelectronic Applications. Chem. Mater. 2011, 23, 501-515.

(48) Cui, Q.; Bazan, G. C. Narrow Band Gap Conjugated Polyelectrolytes. Acc. Chem. Res. 2018, 51, 202-211.

(49) Padvi, M. N.; Moholkar, A. V.; Prasad, S. R.; Prasad N. R. A Critical Review on

Design and Development of Gas Sensing Materials. Eng. Sci., 2021, 15, 20-37.

(50) Lin. P.; Yan, F. Organic Thin-Film Transistors for Chemical and Biological Sensing.

Adv. Mater. 2012, 24, 34-51.

(51) Fan, L. J.; Zhang, Y.; Murphy, C. B.; Angell, S. E.; Parker, M. F.; Flynn, B. R.; Jones Jr, W. E. Fluorescent Conjugated Polymer Molecular Wire Chemosensors for

Transition Metal Ion Recognition and Signaling. Coordination Chemistry Reviews 2009, 253,410-422.

(52) Zhu, C.; Liu, L.; Yang, Q.; Lv, F.; Wang, S. Water-Soluble Conjugated Polymers for Imaging, Diagnosis, and Therapy. Chem. Rev. 2012, 112, 4687-4735

(53) Gopalan, A-I.; Komathi, S.; Muthuchamy, N.; Lee, K-P.; Whitcombe, M.J.; Dhana, L.; Anand, G. S. Functionalized Conjugated Polymers for Sensing and Molecular Imprinting Applications. Prog. Polym. Sci. 2019, 88, 1-29.

(54) Liu, Y.; Ogawa, K.; Schanze, K. S. Conjugated Polyelectrolytes as Fluorescent Sensors. Photochem. Photobiol. C: Photochem. Rev. 2009, 10, 173-190.
(55) Zhang, C.; Chen, P.; Hu, W. Organic Field-Effect Transistor-Based Gas Sensors.Chem. Soc. Rev. 2015, 44, 2087-2107.

(56) Li, H.; Shi, W.; Song, J.; Jang, H-J.; Dailey, J.; Yu, J.; Katz, H. E. Chemical and Biomolecule Sensing with Organic Field-Effect Transistors. Chem. Rev. 2019, 119, 3-35.

(57) Koo, W-T. K.; Kim, Y.; Savagatrup, S.; Yoon, B.; Jeon, I.; Choi, S-J.; Kim, I-D.;Swager, T. M. Porous Ion Exchange Polymer Matrix for Ultrasmall Au NanoparticleDecorated Carbon Nanotube Chemiresistors. Chem. Mater. 2019, 31, 5413-5420.

(58) Roberts, M. E.; Sokolov, A. N.; Bao, Z. Material And Device Considerations for Organic Thin-Film Transistor Sensors. J. Mater. Chem. 2009, 19, 3351–3363.

(59) Malik, A. H.; Hussain, S.; Kalita, A.; Iyer, P. K. Conjugated Polymer Nanoparticles for the Amplified Detection of Nitro-explosive Picric Acid on Multiple Platforms. ACS Appl. Mater. Inter. 2015, 7, 26968-26976.

(60) Kalita, A.; Hussain, S.; Malik, A. H.; Subbarao, N. V. V.; Iyer, P. K. Vapor Phase Sensing of Ammonia at the sub-ppm Level using a Perylene Diimide Thin Film Device. J. Mater. Chem. C 2015, 3, 10767-10774.

(61) Torsi, L.; Magliulo, M.; Manoli, K.; Palazzo, G. Organic Field-Effect Transistor Sensors: A Tutorial Review. Chem. Soc. Rev. 2013, 42, 8612-8628.

(62) Kalita, A.; Hussain, S.; Malik, A. H.; Barman, U.; Goswami, N.; Iyer, P. K. AnionExchange Induced Strong π–π Interactions in Single Crystalline Naphthalene Diimide for Nitroexplosive Sensing: An Electronic Prototype for Visual on- Site Detection. ACS Appl. Mater. Interfaces 2016, 8, 25326-25336.

[This page is intentionally kept blank]

Chapter 2

Modulating carrier injection through rational control of hole transport layer for perovskite light emitting diodes

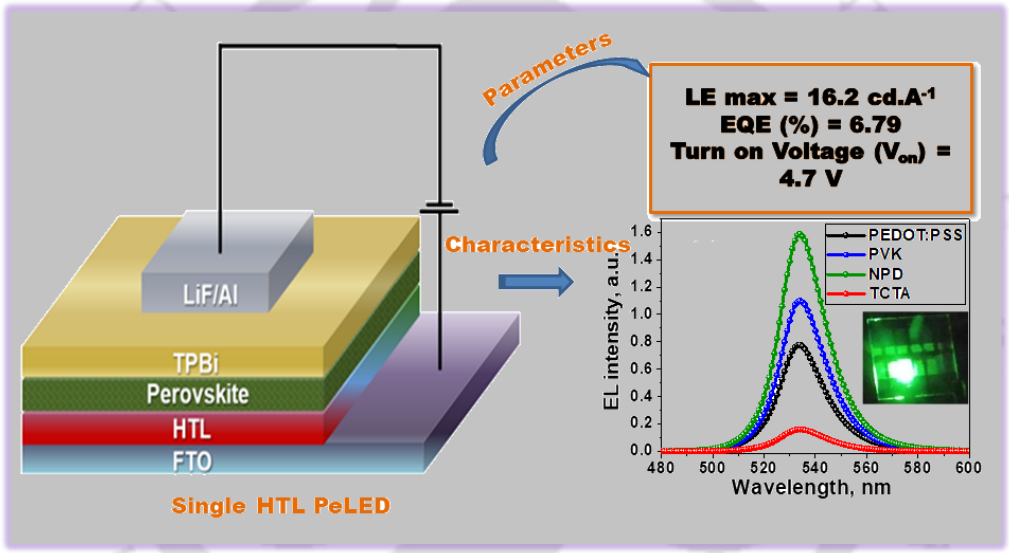

Manuscript: Ramesh Babu Yathirajula, Ritesh Kant Gupta, Mohammad Adil Afroz, Anwesha Choudhury, Parameswar Krishnan Iyer, "Modulating carrier injection through rational control of hole transport layer for perovskite light-emitting diodes." *Journal of Materials Science: Materials in Electronics, Springer, 03, 2023*, DOI: https://doi.org/10.1007/s10854-023-10066-w.

[This page was intentionally left blank]

Abstract

Charge balance in the emissive layer through well-match energy levels and reduced barrier of the transport layers can help to attain maximum radiative recombination. In this work, four hole transporting layers (HTLs) have been used to regulate the hole injection in the emissive layer. The HTLs have varying HOMO levels aligning with the work function of FTO and HOMO of the emissive layer. Among the four HTLs, NPD-based perovskite LED device demonstrated the best performance with highest brightness of 24343 cd m^{-2}, current efficiency of 16.2 cd A^{-1}, and turn-on voltage of 4.7 V. The main reason for such improved results was the well-match HOMO of NPD with both the anode and emissive layer supporting enhanced hole injection. Both the photoluminescence and electroluminescence studies confirm pure green emission with CIE coordinates (0.22, 0.75). Best quality film morphology for NPD-based perovskite film supported efficient transport of the charges. The crystallinity of the NPD-based perovskite film was also found to be optimum. Finally, stability of the working PLEDs is tested and superior stability with 79% of the retention of initial brightness is observed for NPD-based device.

2.1 Overview

At the peak of demand for energy conservation, the light emitting diodes (LEDs) have become a power savior compared to the incandescent and fluorescence technologies.[1, 2] Both inorganic and organic LEDs have been well explored for various applications including displays, lighting, communications and laser sources.[3, 4] However, the inorganic LEDS require high temperature and the organic ones offer very low quantum efficiency.[5] Recently, perovskites after gaining much importance in the field of photovoltaics are being now explored for LED applications as well.[6-8] The material offers series of advantages such as high crystallinity, direct band gap, easily color tunable, long carrier lifetimes, high quantum yield, and higher carrier mobilities.[9-12] It offers good film forming property making it suitable for fabrication of perovskite LED (PLED) through solution-processing technique even on flexible and large area substrates.[13] The researches on PLEDs have now garnered some pace and quantum efficiency of over 23% has been achieved.[14]

Two types of perovskite materials are being used in the fabrication of PLEDs: (i) all inorganic such as cesium lead bromide (CsPbBr3) and (ii) hybrid organic inorganic perovskite (HOIP) such as methyl ammonium lead bromide (MAPbBr3).[15, 16]Among, these two, the all inorganic PLED has impacted more compared to the HOIP. However, at the same time the processing temperature of the same is much higher.[17] Hence, significant developments are being carried out using HOIP PLEDs, especially with MAPbBr3. Further, MAPbBr3 facilitates easy crystallization compared to other perovskite having similar opto-electronic properties. The defects present in the perovskite layer are passivated using various organic and inorganic additives similar to ones done for solar cell application.[18-21] This has resulted in better perovskite film with improved coverage through uniform nucleation.[22] The passivation of defect traps on the perovskite surface is also performed by coating these materials on top of the emissive layer to improve the charge injection.[23] Further, anti-solvent dripping of low boiling point solvents has been also performed to control the crystallization kinetics of the perovskite layer to obtain smooth films.[24, 25] The anti-solvents are expected to remove the excess processing solvents in the perovskite films that prevent the device degradation.[26] Another unique method of nano-crystal pinning has been developed where organic additives are added along with the anti-solvent to not only remove the excess solvents but also passivate the defects of the surface of the perovskite

films.[27] It is well-known that any surface defects or non-smooth film coverage of the perovskite leads to serious leakage problem leading to mitigated device performance and stability.[28, 29] Once proper crystalline perovskite films are obtained the challenge is to inject holes and electrons in the emissive layer for them to recombine radiatively.[30, 31] Significant interfacial engineering is taking place to maintain the maximum charge balance in the emissive layer.[32] 2,2',2"-(1,3,5-Benzinetriyl)-tris(1-phenyl-1-H-benzimidazole) (TPBi) is one of the standard materials for use as electron transport layer (ETL) and poly(3,4-ethylenedioxythiophene) polystyrene sulfonate (PEDOT:PSS) is frequently used as hole transport layer (HTL) in PLEDs.[9, 33] However, the acidic nature of PEDOT:PSS causes the perovskite layer on top to degrade.[34, 35] Also, the barrier for hole injection in the emissive layer is large, thereby sufficient charge balance is not created for radiative recombination.[36] Thus, the HTL has been modified strategically to obtain well-matched highest occupied molecular orbital (HOMO) level with the emissive layer for appropriate hole injection.[37-39] Instead of PEDOT:PSS various other HTLs have also been tried in the fabrication of PLEDs.[40] In this work, Herein, PLEDs with MAPbBr3 as emissive layer has been chosen through strategically selecting the HTLs among PEDOT:PSS, poly(9-vinylcarbazole) (PVK), N,N′-Bis(naphthalen-1-yl)-N,N′-bis(phenyl)-2,2′-dimethylbenzidine (NPD) and Tris(4-carbazoyl-9-ylphenyl)amine (TCTA). The barrier for hole injection can be tuned by the work function or the HOMO of the selected HTLs, as a result the brightness of the PLED varied and highest luminance of 24343 cd m^{-2} is observed for NPD based device which has HOMO well matched with the HOMO of perovskite and work function of FTO. This ensured better hole injection and charge balance in the emissive layer. The output light is of pure green color with CIE coordinates of (0.22, 0.75). Electroluminescence (EL) and photoluminescence (PL) study of all the HTL based perovskite devices and films, respectively were also recorded and the EL and PL peaks were found at 534 and 540 nm, respectively. Time-resolved photoluminescence (TRPL) spectroscopy studies also showed longest carrier lifetime for NPD-based perovskite film. Morphological studies through field emission scanning electron microscopy (FESEM) of perovskite on top of each HTL layer were also taken. All perovskite films showed small domains for on top of each HTL, however, the perovskite layer on top of NPD showed unique and smooth domains which resulted in best performance. Further, the crystallinity of the perovskite on each HTL layer is confirmed using X-ray diffraction (XRD) studies. All films showed polycrystalline peaks, but the least full width half maxima (FWHM) is

obtained for NPD-based perovskite film. Lastly, the stability of the devices was verified and 79% retention of initial brightness is observed for NPD-based device compared to the other counterpart.

2.2 Experimental Section

2.2.1 Materials

Fluorine doped tin oxide (FTO) coated glass (7Ω/sq.), Lead bromide (PbBr2,99.8%),Methyl ammonium bromide (MABr, 99%), DMF (anhydrous, 99.8%), DMSO (anhydrous, 99.8%), Chloroform (anhydrous, 99.8%), PVK(poly(9-vinylcarbazole)), N,N′-Bis(naphthalen-1-yl)-N,N′-bis(phenyl)-2,2′-dimethylbenzidine (NPD) and Tris(4-carbazoyl-9-ylphenyl)amine (TCTA), Lithium fluoride (LIF) and Aluminum (Al) were purchased from Sigma-Aldrich. Poly (3,4-ethylenedioxythiophene) polystyrene sulfonate (PEDOT:PSS, PVP AI 4083) was purchased from Clevios. 2,2',2"-(1,3,5-Benzinetriyl)-tris(1-phenyl-1-H-benzimidazole).(TPBi) was purchased from was purchased from LUMTEC. All other chemicals were used as received

2.2.2 Device Fabrication

The perovskite light emitting diodes (PLEDs) were fabricated on FTO coated glass which was prepatterned and cleaned consecutively in soap solution, de-ionized water, acetone and isopropanol. The substrate was then dried under N2 gas and UV-ozone treated before further processing. Thereafter, the as purchased PEDOT:PSS was coated at 4000 rpm for 45 s for the PEDOT:PSS-based PLED. For the remaining three types of PLED, PVK, NPD and TCTA were taken at 15 mg/mL each with chlorobenzene as processing solvent and coated at 4000 rpm for 45 s. All the coated HTLs were annealed at 120 ºC for 30 min. All the coated HTLs were approximately 40 nm. The perovskite precursor solution was prepared by dissolving MABr and PbBr2 with a 1.1:1 in anhydrous DMF and DMSO (7:3) to give a concentration of 30 wt%. Then the solution is stirred at 70oC for 2 hours to make sure all the solutes are soluble. Then, the substrates were transferred to spin coater chuck for two step spin coating method to obtain the perovskite films. In step 1 the chuck is rotated at 500 rpm for 5 s for uniform spreading of the precursor solution on the substrate. In step 2, the speed of the chuck is increased to 3000 rpm for 50 s and after 10 s of step 2, chloroform (100 μL) is dripped slowly for anti-solvent treatment.

Thereafter, the perovskite films are annealed at 70 °C for 15 min to obtain ~90 nm thick films. Finally, TPBi (40 nm), LiF (1 nm) and Al (100 nm) were vapor deposited at a base pressure of 10^{-6} mbar at a rate of 0.5, 0.1 and 1.0Å/s, respectively. The active area of the PLEDs was 25 mm^2. The overall device architecture was FTO/HTL/Perovskite/TPBi/LiF/Al.

2.2.3 Characterization

The morphology of perovskite samples were examined on scanning electron microscopy (SEM, JEOL JSM-7610F). Perovskite films were characterized by X-ray diffraction (XRD, Rigaku Micromax-007HF diffract meter equipped with Cu Kα1 irradiation [λ =1.54184Å]), UV–vis absorption spectroscopy (PerkinElmer Lambda-35). Photoluminescence studies were recorded using a fluorescence spectrophotometer (HORIBA JobinYvon, fluoromax-4 with a 405 nm laser excitation).Time-resolved fluorescence studies were performed using an Edinburgh Life Spec II instrument. The current density versus voltage (J-V) characteristics of the perovskite LEDs were measured using a Keithley 2400 source meter, whereas the luminance versus voltage (L-V) characteristics and the EL spectra were recorded using Konica Minolta CS 2000 Spectroradiometer.

2.3 Results and Discussions

Figure 2.1a, shows chemical structures of all four HTLs i.e., PEDOT:PSS, PVK, NPD and TCTA used for this work. **Figure 2.1b**, shows energy band diagram of PLEDs with different HTLs. The electron transport layer (ETL) and HTLs for an LED has to be selected such that the electron injection to the lowest unoccupied molecular orbital (LUMO) of the emissive layer and hole injection to the HOMO of the emissive layer can be done conveniently. Thus, the selection of ETL and HTL becomes very important so that majority of the injected electron and hole pairs can recombine radiatively. TPBi is used as standard ETL because it is not only proven to be very good electron injecting material, but also effectively blocks the transport of holes from the emissive layer.[9] Similarly, in the HTL side the HOMO should be well-matched to not only the perovskite layer, but also the work function of the transparent conducting oxides (FTO in this case). Hence, the four HTLs are taken in such a way so that the HOMOs lie in between the work function of FTO and HOMO of emissive layer. This allowed efficient hole injection from FTO to HOMO of the perovskite layer even with an offset of 1.0 eV. Additionally, all HTLs, except

PEDOT:PSS, can also effectively work as electron blocking layer. Ultraviolet Photoelectron Spectroscopy (UPS) was performed to estimate the energy levels of the HTLs and perovskite as presented in **Figure A2.1**.The work function of PEDOT:PSS is 5.1 eV, while the HOMOs of PVK, NPD and TCTA are 5.4, 5.6, 5.8 eV, respectively and the results matched well with the reported values.[41-44] The work function of PEDOT:PSS and HOMO of PVK still shows some energy barrier/offset with the HOMO of perovskite layer. Also, the HOMO of TCTA has energy offset with the FTO. But, HOMO of NPD is intermediate in energy offset with both perovskite and FTO, thus it is expected to have smoother hole injection from FTO to perovskite and better charge balance at the emissive layer. This will allow the recombination zone to be created away from the transport layers and radiative recombination can be increased significantly.[45]

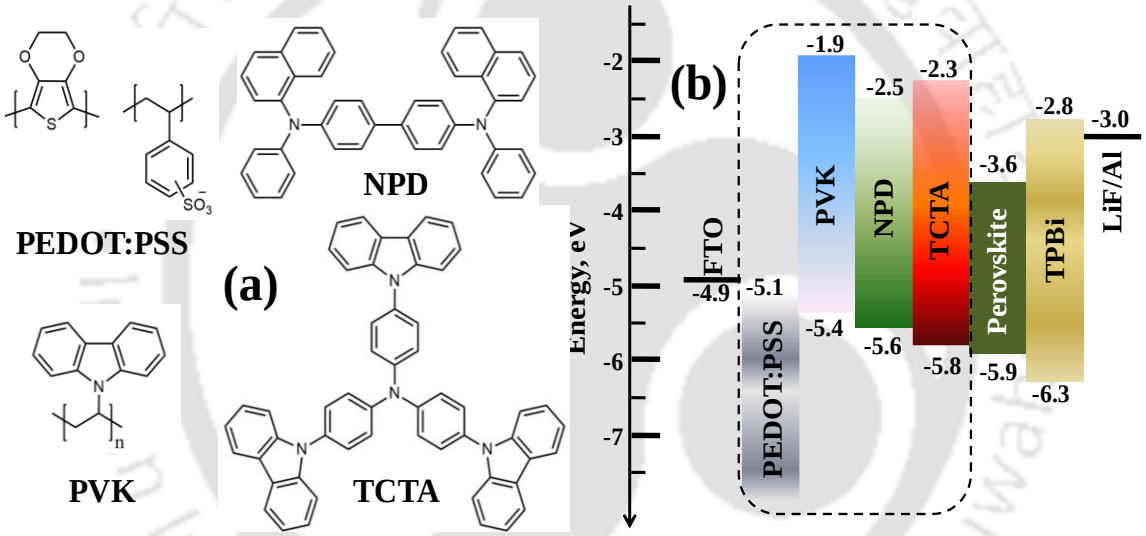

Figure 2.1: (a) Chemical structures of all four hole transporting layers and (b) energy band diagram of perovskite LED device fabricated using MAPbBr3 as an emissive layer.

PLED devices with different HTL layers were fabricated with the architecture FTO/HTL/Perovskite/TPBi/LiF/Al (**Figure A2.2**). The current density-voltage (J-V) curves of all the four PLEDs (**Figure 2.2a**) are exponential in nature and displayed good diode characteristics suggesting that the current is injection limited at lower voltages and space charge limited at higher voltages.[46, 47] From the J-V curve it is found that the current density value for the NPD-based PLED is higher than the other devices. The intermediate HOMO of NPD played a crucial role to minimize the energy barrier of NPD from work function of FTO and HOMO of perovskite emissive layer. This confirms that more number of charges are easily injected in the

perovskite emissive layer contributing to higher recombination current. This resulted in minimum turn-on voltage (V_{on}) of 4.7V for NPD-based PLED. Von of 5.0, 4.8, 4.9 V is obtained for PEDOT:PSS, PVK, TCTA-based PLEDs, respectively.

The luminance for each PLED devices were also recorded at various voltages and presented in **Figure 2.2b**, The highest luminance of 24343 cd m^{-2} is recorded for NPD-based device at 6 V which is one of the best in all $MAPbBr_3$ based PLEDs. For the remaining HTLs the luminance values are 11818, 16814 and 2498 cd m^{-2} for PEDOT:PSS, PVK and TCTA-based PLEDs, respectively at 6 V. The probable reason for higher luminance value for NPD-based device is better hole injection from the anode to the emissive layer through NPD due to better band matching than the other HTLs because of balanced energy offset from FTO to NPD and from NPD to emissive layer. This allows better hole injection in the emissive layer. This creates a charge balance in the emissive layer; hence maximum radiative recombination is obtained for NPD-based PLED. Though, the HOMO of TCTA is closer to the HOMO of emissive layer, yet since the energy offset between TCTA and FTO is higher, hole injection to the emissive layer is reduced. This has resulted in the recombination zone closer to the HTL, but in the case of NPD the recombination would occur within the emissive layer, hence the highest luminance.

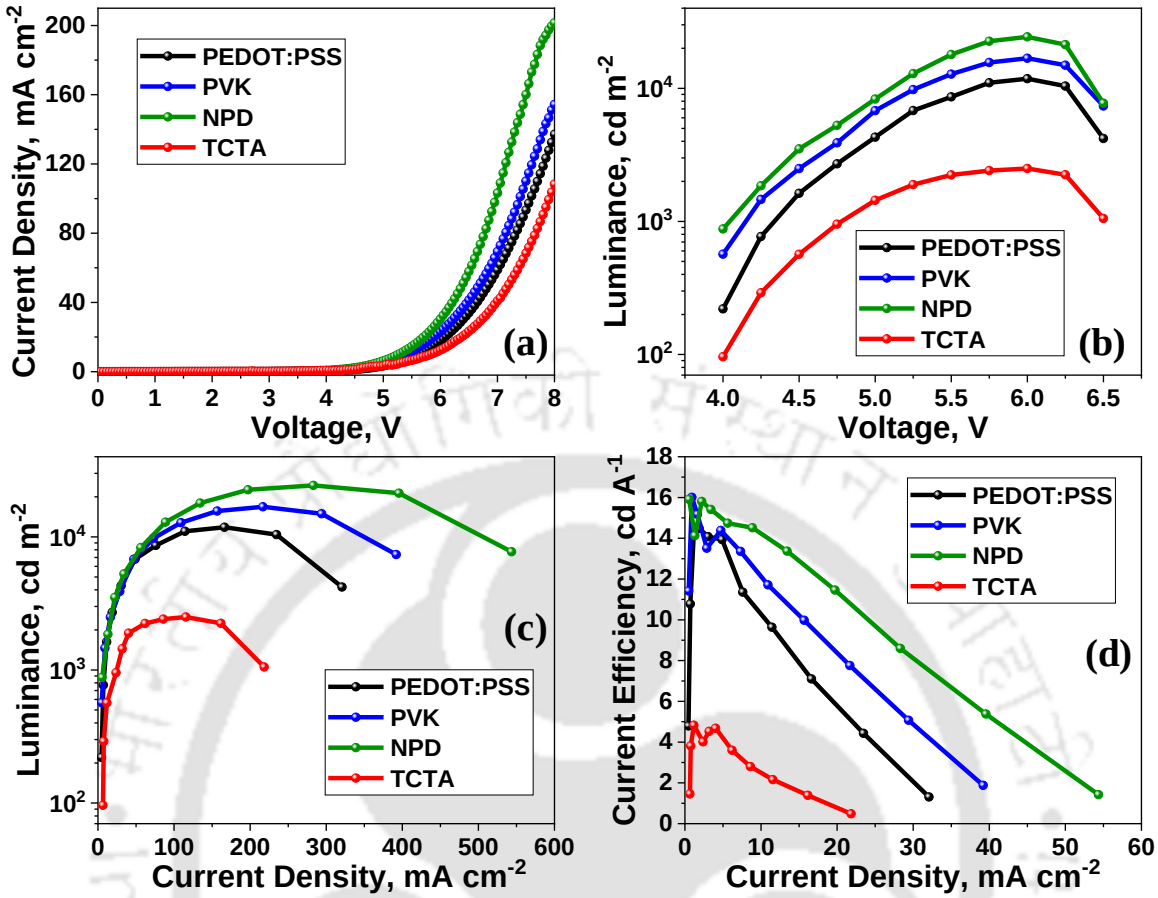

Figure 2.2: (a) current density versus voltage, (b) luminance versus voltage, (c) luminance versus current density and (d) current efficiency versus current density curves of PLEDs with different HTLs.

The variation in luminance and current efficiency with respect to current density is presented in **Figure 2.2c and 2.2d**, respectively. The luminance increases with the increase in current density and after attaining the highest value for each HTL the luminance decreases at higher current density. However, it can be well observed that the drop in luminance for NPD-based PLED occurs at much higher current density compared to the other HTLs. The well-matched band alignment of NPD has most likely ensured the holes to get injected easily in the emissive layer which allowed the highest luminance at higher current density. Similarly, current efficiency is also optimum at a particular current density value and decreases at higher current density. The best current efficiency of 16.2 cd A^{-1} is obtained for NPD-based PLED. PEDOT:PSS, PVK and TCTA-based PLEDs display current efficiencies of 12.1, 12.8, and 4.2 cd A^{-1}, respectively.

Figure A2.3 displays the EL spectra for all four HTLs with bias voltage varied from 4.0 to 6.5 V with a step size of 0.25 V. For all the four HTLs, the EL spectra's λ-peak is constant at ~534 nm for different voltages which indicates the stability of EL peak for different voltages for all the HTLs. **Figure 2.3a** shows the EL spectra of all the four PLEDs at 6 V. Inset of **Figure 2.3a** shows the photograph of working LED. The EL intensity is higher for NPD based-PLED compared to the other three HTL-based PLEDs. For the NPD-based device, the radiative recombination is higher due to efficient hole injection in the emissive layer resulting in better charge balance compared to the other three PLED devices. The full width half maximum (FWHM) is found to be ~24 nm and the λPeak is ~534 nm for all the PLED devices. **Figure 2.3b** presents the Commission Internationale de I'Eclairage (CIE) chromaticity coordinates of the fabricated PLEDs. As can be seen in the figure the CIE coordinates for PLEDs obtained is around (0.22, 0.75) which indicates pure green emission. All the device parameters are enlisted and presented in **Table A2.1**.

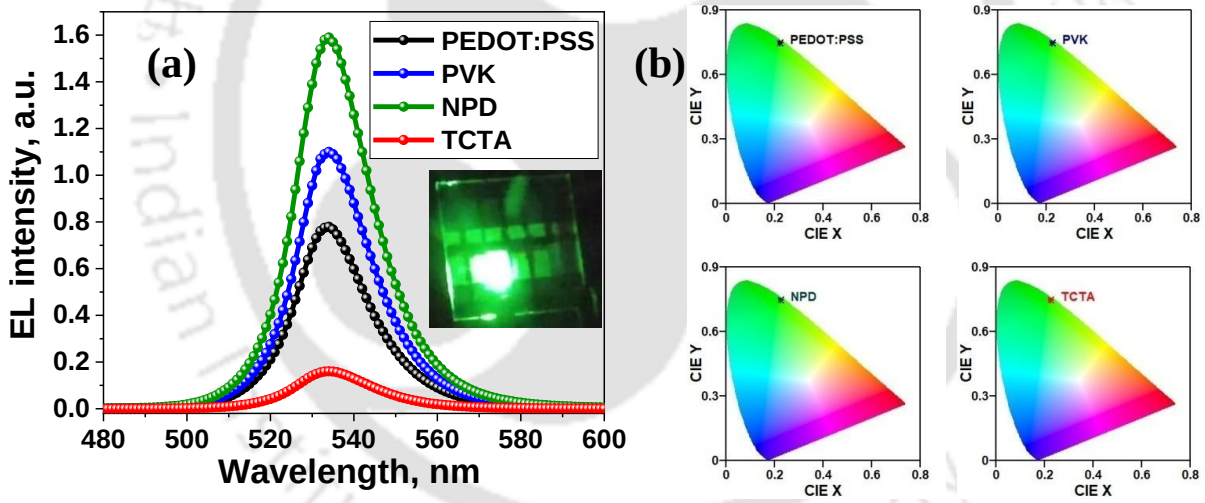

Figure 2.3: (a) EL spectra for PEDOT:PSS, PVK, NPD and TCTA-based PLEDs at 6 V and inset showing green emission of NPD-based working PLED, and (b) CIE diagrams for PEDOT:PSS, PVK, NPD and TCTA-based PLEDs.

Figure 2.4a-d shows the morphology of the perovskite films coated on each HTL using the field emission scanning electron microscopy (FESEM). It can be seen that small crystalline domains were formed for perovskite coated on top of PEDOT:PSS as HTL. These domains become distinct when PVK was used as HTL, but clear and smooth features could be seen for the

perovskite film coated on top of NPD as HTL. However, when TCTA was used as HTL, the perovskite domains overlapped with each other reducing the smoothness. This can be one of the possible reasons for smooth charge transport through NPD to the perovskite layer. Further, smooth perovskite films do not allow charges to dissociate, instead it is given a path to radiatively recombine easily in the emissive layer which is happening on the case of NPD based device.[28] Further, and it can be observed that the density of grain boundary is the minimum for NPD-based perovskite films. The reduction in grain boundary ensures that the non-radiative charge recombination is minimized.

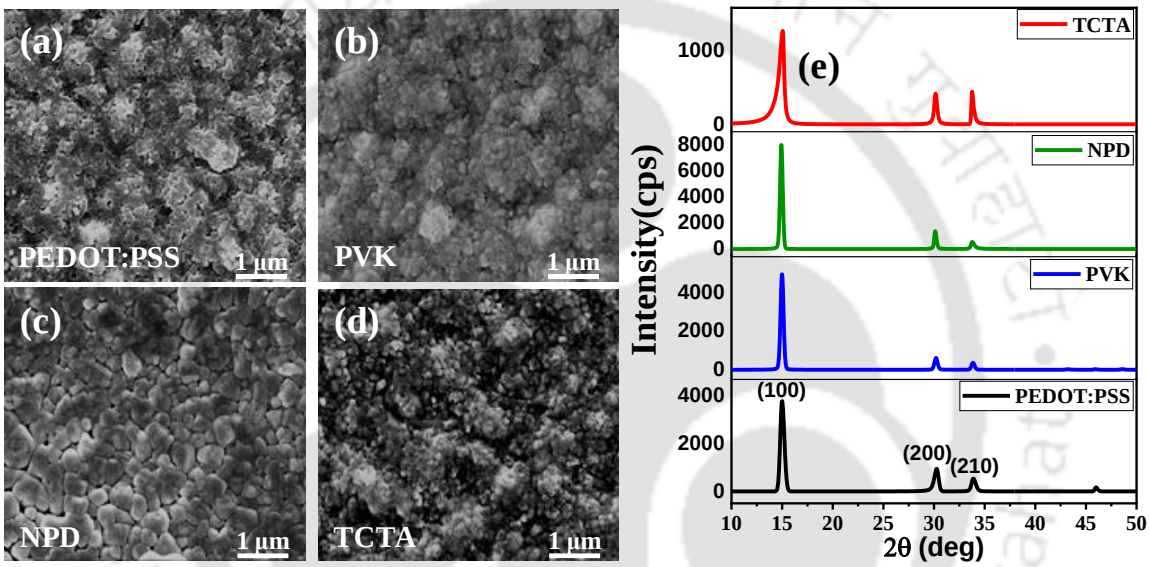

Figure 2.4: (a-d) Field emission scanning electron microscopy images for perovskite films based on PEDOT:PSS, PVK, NPD and TCTA as HTLs, and (e) XRD patterns for perovskite films with different HTLs.

To further confirm the crystallinity of the perovskite emissive layer coated on top of various HTLs, X-ray diffraction (XRD) study is performed (**Figure 2.4e**). The XRD spectra exhibited two distinct and strong diffraction peaks at 14.95º, 30.15º and 33.90º for all perovskite films which correspond to (100), (200) and (210) planes, respectively of cubic MAPbBr3.[48] Outstanding crystallinity and preferred orientation of diffraction peaks are obtained for NPD-based perovskite films compared to the other three films. Furthermore, the FWHM is also obtained for the (100) plane for all HTL coated perovskite films and was found to be 0.60º, 0.37º, 0.34ºand 0.78º for PEDOT:PSS, PVK, NPD and TCTA-based perovskite films,

respectively. Lowest FWHM value for NPD-based perovskite film also confirms enhanced crystallinity.[49]

Figure A2.4 shows the PL of the perovskite emissive layer on various HTLs. The PL λ_{Peak} is found at 540 nm for all the samples justifying the reason for good green emitters. NPD-based perovskite film displays the highest PL intensity which indicates that maximum radiative recombination of the generated charges. This can be a possible reason for NPD-based PLED to showcase highest brightness value compared to the other three PLED devices. **Figure A2.5** shows the time-resolved photoluminescence (TRPL) spectroscopy which is a tool to investigate excited charge carrier recombination in semiconductors and molecular systems. The lifetimes are obtained through bi-exponential fitting of the TRPL spectra. Two lifetimes are: (i) fast due to trap assisted recombination (τ1), and (ii) slow for radiative recombination in the bulk of emissive layer (τ2).[48, 50] τ1is estimated to be 2.63, 2.81, 3.90 and 1.98 ns for PEDOT:PSS, PVK, NPD and TCTA, respectively. τ2 is estimated to be 44.56, 45.98, 48.60, and 40.72 ns for PEDOT:PSS, PVK, NPD and TCTA, respectively. From the estimated τ1and τ2 values the average charge carrier lifetime (τavg) is calculated and it is found to be 35.92, 39.17, 43.85 and 32.76 ns for PEDOT:PSS, PVK, NPD and TCTA, respectively. Even though the τ1 is higher for NPD-based PLED, the higher τ2 leads to highest τavg. Hence, the best PLED brightness is obtained for NPD-based device. All the carrier lifetimes are enlisted in **Table A2.2**.

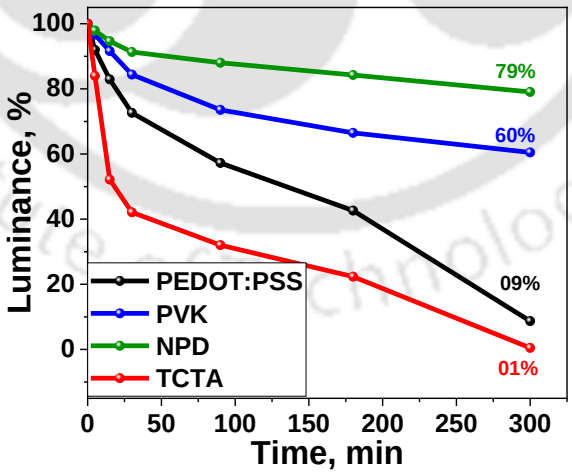

Figure 2.5: Stability study tested with respect to luminance for 300 minutes at 6V.

Stability of an LED device is one important factor for its acceptance in various applications. Thus, the stability of the PLED devices (**Figure 2.5**) is tested with respect to luminance for 300 minutes. The luminance is recorded at 6V, i.e. at voltage where highest brightness is recorded for all four PLED devices. It is observed that after 300 minutes the NPD-based device displayed best stability compared to other three PLEDs. For PEDOT:PSS, PVK, NPD and TCTA-based PLED 9%, 60%, 79% and 1% initial brightness is retained, respectively. The most likely reason for improved device stability of the NPD-based PLED is the charge balance in the emissive layer which is allowing the recombination zone to be created in the bulk instead of at the interfaces. Since, the charge balance for the other three PLED devices is not as adequate as in NPD-based device the recombination zone is created away from the centre for emissive layer due to which some charge pairs recombine non-radiatively creating heat and damaging the transport layers and electrodes. TCTA showed the minimum stability as perovskite displayed lower crystallinity when coated above it resulting in faster degradation due to the recombination of charges near the transport layers. Also, for PEDOT:PSS being acidic, the PLED device based on it deteriorate faster, thus displaying retention of only 9% of initial luminance after 300 minutes. Hence, the lifetime of the NPD-based device showed enhanced stability compared to the three PLEDs.

2.4 Conclusions

In this work, stable $MAPbBr_3$-based PLEDs with high brightness is fabricated by strategically selecting the HTL for efficient hole injection and charge balance in the emissive layer. The crucial effects of hole injection barrier and the hole transport properties of different HTLs on the charge transport, luminescence and current efficiency are studied. NPD-based PLED showed the best result with Von of 4.7 V and highest luminance of 24343 cd m^{-2} at 6 V for $MAPbBr_3$-based PLED. The main reason for such improved brightness is that the HOMO of NPD was lying intermediate to work function of FTO and HOMO of emissive layer which facilitated holes to be injected easily for radiative recombination. The results are well supported with electrical, morphological and photo-physical characterizations. The NPD-based perovskite film displayed uniform grain distribution with maximum crystallinity which resulted in pure green color with the λPeak at 534 nm in EL study. Finally, the working stability of the fabricated PLEDs were tested and found that the NPD-based device displayed enhanced stability by retaining 79% of its initial brightness. NPD as HTL allowed the charge balance to occur in the

emissive layer which resulted in recombination zone to be created at the centre, away from the transport layers.

References

(1) N.K. Kumawat, A. Dey, K.L. Narasimhan, D. Kabra, Near infrared to visible electroluminescent diodes based on organometallic Halide perovskites: Structural and optical investigation, ACS Photonics 2 (2015) 349–354.

(2) D. Das, P. Gopikrishna, D. Barman, R.B. Yathirajula, P.K. Iyer, White light emitting diode based on purely organic fluorescent to modern thermally activated delayed fluorescence (TADF) and perovskite materials, Nano Converg. 6 (2019) 31.

(3) N.K. Kumawat, D. Gupta, D. Kabra, Recent advances in metal Halide-based perovskite light-emitting diodes, Energy Technol. 5 (2017) 1734–1749.

(4) W. Faschinger, J. Nürnberger, Green II–VI light emitting diodes with long lifetime on InP substrate, Appl. Phys. Lett. 77 (2000) 187–189.

(5) A. Ren, H. Wang, W. Zhang, J. Wu, Z. Wang, R.V. Penty, I.H. White, Emerging light-emitting diodes for next-generation data communications, Nat. Electron. 4 (2021) 559–572.

(6) R. Garai, R.K. Gupta, A.S. Tanwar, M. Hossain, P.K. Iyer, Conjugated polyelectrolyte-passivated stable perovskite solar cells for efficiency beyond 20%, Chem. Mater. 33 (2021) 5709–5717.

(7) M.A. Afroz, R.K. Gupta, R. Garai, M. Hossain, S.P. Tripathi, P.K. Iyer, Crystallization and grain growth regulation through Lewis acid-base adduct formation in hot cast perovskite-based solar cells, Org. Electron. 74 (2019) 172–178.

(8) G. Pacchioni, Highly efficient perovskite LEDs, Nat. Rev. Mater. 6 (2021) 108–108.

(9) Z. Xiao, R.A. Kerner, L. Zhao, N.L. Tran, K.M. Lee, T.-W. Koh, G.D. Scholes, B.P. Rand, Efficient perovskite light-emitting diodes featuring nanometre-sized crystallites, Nat. Photonics 11 (2017) 108–115.

(10) R. Garai, M.A. Afroz, R.K. Gupta, P.K. Iyer, Efficient trap passivation of $MAPbI_3$ via multifunctional anchoring for high-performance and stable perovskite solar cells, Adv. Sustain. Syst. 4 (2020).

(11) M. Hossain, R. Garai, R.K. Gupta, R.N. Arunagirinathan, P.K. Iyer, Fluoroarene derivative based passivation of perovskite solar cells exhibiting excellent ambient and thermo-stability achieving efficiency >20%, J. Mater. Chem. C Mater. Opt. Electron. Devices 9 (2021) 10406–10413.

(12) A. Choudhury, R.K. Gupta, R. Garai, P.K. Iyer, Tailoring trap density of states through impedance analysis for flexible organic field-effect transistors, Adv. Mater. Interfaces 8 (2021).

(13) S. Chu, W. Chen, Z. Fang, X. Xiao, Y. Liu, J. Chen, J. Huang, Z. Xiao, Large-area and efficient perovskite light-emitting diodes via low-temperature blade-coating, Nat. Commun. 12 (2021) 147.

(14) Y.-H. Kim, S. Kim, A. Kakekhani, J. Park, J. Park, Y.-H. Lee, H. Xu, S. Nagane, R.B. Wexler, D.-H. Kim, S.H. Jo, L. Martínez-Sarti, P. Tan, A. Sadhanala, G.-S. Park, Y.-W. Kim, B. Hu, H.J. Bolink, S. Yoo, R.H. Friend, A.M. Rappe, T.-W. Lee, Comprehensive defect suppression in perovskite nanocrystals for high-efficiency light-emitting diodes, Nat. Photonics 15 (2021) 148–155.

(15) Q. Van Le, H.W. Jang, S.Y. Kim, Recent advances toward high-efficiency Halide perovskite light-emitting diodes: Review and perspective, Small Methods 2 (2018).

(16) X. Zhang, H. Liu, W. Wang, J. Zhang, B. Xu, K.L. Karen, Y. Zheng, S. Liu, S. Chen, K. Wang, X.W. Sun, Hybrid perovskite light-emitting diodes based on perovskite nanocrystals with organic–inorganic mixed cations, Adv. Mater. 29 (2017).

(17) Z. Wei, A. Perumal, R. Su, S. Sushant, J. Xing, Q. Zhang, S.T. Tan, H.V. Demir, Q. Xiong, Solution-processed highly bright and durable cesium lead halide perovskite light-emitting diodes, Nanoscale 8 (2016) 18021–18026.

(18) R.K. Gupta, R. Garai, P.K. Iyer, Dual-passivation strategy for improved ambient stability of perovskite solar cells, ACS Appl. Energy Mater. 4 (2021) 10025–10032.

(19) L.A. Frolova, A.I. Davlethanov, N.N. Dremova, I. Zhidkov, A.F. Akbulatov, E.Z. Kurmaev, S.M. Aldoshin, K.J. Stevenson, P.A. Troshin, Efficient and stable $MAPbI_3$-based perovskite solar cells using polyvinylcarbazole passivation, J. Phys. Chem. Lett. 11 (2020) 6772–6778.

(20) H. Zhang, F. Ye, W. Li, J. Yao, R.S. Gurney, D. Liu, C. Xiong, T. Wang, Bright perovskite light-emitting diodes with improved film morphology and reduced trap density via surface passivation using quaternary ammonium salts, Org. Electron. 67 (2019) 187–193.

(21) H. Zhang, F. Ye, W. Li, R.S. Gurney, D. Liu, C. Xiong, T. Wang, Improved performance of perovskite light-emitting diodes by dual passivation with an ionic additive, ACS Appl. Energy Mater. 2 (2019) 3336–3342.

(22) S. Venkatesan, M. Hasan, J. Kim, N.R. Rady, S. Sohal, E. Neier, Y. Yao, A. Zakhidov, Tailoring nucleation and grain growth by changing the precursor phase ratio for efficient organic lead halide perovskite optoelectronic devices, J. Mater. Chem. C Mater. Opt. Electron. Devices 5 (2017) 10114–10121.

(23) X. Yang, X. Zhang, J. Deng, Z. Chu, Q. Jiang, J. Meng, P. Wang, L. Zhang, Z. Yin, J. You, Efficient green light-emitting diodes based on quasi-two-dimensional composition and phase engineered perovskite with surface passivation, Nat. Commun. 9 (2018) 1–8.

(24) J. Kumar, R. Kumar, K. Frohna, D. Moghe, S.D. Stranks, M. Bag, Unraveling the antisolvent dripping delay effect on the Stranski–Krastanov growth of $CH_3NH_3PbBr_3$thin films: a facile route for preparing a textured morphology with improved optoelectronic properties, Phys. Chem. Chem. Phys. 22 (2020) 26592–26604.

(25) H. Cho, S.-H. Jeong, M.-H. Park, Y.-H. Kim, C. Wolf, C.-L. Lee, J.H. Heo, A. Sadhanala, N. Myoung, S. Yoo, S.H. Im, R.H. Friend, T.-W. Lee, Overcoming the electroluminescence efficiency limitations of perovskite light-emitting diodes, Science 350 (2015) 1222–1225.

(26) K. Bruening, C.J. Tassone, Antisolvent processing of lead halide perovskite thin films studied by *in situ* X-ray diffraction, J. Mater. Chem. A Mater. Energy Sustain. 6 (2018) 18865–18870.

(27) Y. Ahn, S. Lee, D.-H. Kwak, M. Kim, D.Y. Kim, J. Kim, Y. Park, M.C. Suh, Improving the efficiency of perovskite light emitting diode using polyvinylpyrrolidone as an interlayer, Appl. Surf. Sci. 507 (2020) 145071.

(28) S.Y. Kim, H. Kang, K. Chang, H.J. Yoon, Case studies on structure–property relations in perovskite light-emitting diodes via interfacial engineering with self-assembled monolayers, ACS Appl. Mater. Interfaces 13 (2021) 31236–31247.

(29) R. Garai, R.K. Gupta, M. Hossain, P.K. Iyer, Surface recrystallized stable 2D–3D graded perovskite solar cells for efficiency beyond 21%, J. Mater. Chem. A Mater. Energy Sustain. 9 (2021) 26069–26076.

(30) D. Das, P. Gopikrishna, R. Narasimhan, A. Singh, A. Dey, P.K. Iyer, White polymer light emitting diodes based on PVK: the effect of the electron injection barrier on transport properties, electroluminescence and controlling the electroplex formation, Phys. Chem. Chem. Phys. 18 (2016) 33077–33084.

(31) S.D. Stranks, R.L.Z. Hoye, D. Di, R.H. Friend, F. Deschler, The physics of light emission in Halide perovskite devices, Adv. Mater. 31 (2019). https://doi.org/10.1002/adma.201803336.

(32) B. Zhang, J. Liu, J. Wang, Y. Ruan, X. Ji, K. Xu, C. Chen, H. Wan, L. Miao, J. Jiang, Interface engineering: The Ni(OH) 2 /MoS 2 heterostructure for highly efficient alkaline hydrogen evolution, Nano Energy 37 (2017) 74–80.

(33) Z. Wang, Z. Li, D. Zhou, J. Yu, Low turn-on voltage perovskite light-emitting diodes with methanol treated PEDOT:PSS as hole transport layer, Appl. Phys. Lett. 111 (2017).

(34) Y.-H. Kim, S.-H. Lee, J. Noh, S.-H. Han, Performance and stability of electroluminescent device with self-assembled layers of poly(3,4-ethylenedioxythiophene)–poly(styrenesulfonate) and polyelectrolytes, Thin Solid Films 510 (2006) 305–310.

(35) Y. Zhou, S. Mei, D. Sun, N. Liu, W. Shi, J. Feng, F. Mei, J. Xu, Y. Jiang, X. Cao, Improved efficiency of perovskite light-emitting diodes using a three-step spin-coated

CH3NH3PbBr3 emitter and a PEDOT:PSS/MoO3-ammonia composite hole transport layer, Micromachines (Basel) 10 (2019) 459.

(36) W. Wang, Z. Wu, T. Ye, S. Ding, K. Wang, Z. Peng, X.W. Sun, High-performance perovskite light-emitting diodes based on double hole transport layers, J. Mater. Chem. C Mater. Opt. Electron. Devices 9 (2021) 2115–2122.

(37) X. Huang, R. Bäuerle, F. Scherz, J.-N. Tisserant, W. Kowalsky, R. Lovrinčić, G. Hernandez-Sosa, Improved performance of perovskite light-emitting diodes with a NaCl doped PEDOT:PSS hole transport layer, J. Mater. Chem. C Mater. Opt. Electron. Devices 9 (2021) 4344–4350.

(38) Y. Zhou, S. Mei, J. Feng, D. Sun, F. Mei, J. Xu, X. Cao, Effects of PEDOT:PSS:GO composite hole transport layer on the luminescence of perovskite light-emitting diodes, RSC Adv. 10 (2020) 26381–26387.

(39) X.-F. Peng, X.-Y. Wu, X.-X. Ji, J. Ren, Q. Wang, G.-Q. Li, X.-H. Yang, Modified conducting polymer hole injection layer for high-efficiency perovskite light-emitting devices: Enhanced hole injection and reduced luminescence quenching, J. Phys. Chem. Lett. 8 (2017) 4691–4697.

(40) Y. Wu, P. Wang, S. Wang, Z. Wang, B. Cai, X. Zheng, Y. Chen, N. Yuan, J. Ding, W.-H. Zhang, Heterojunction engineering for high efficiency cesium formamidinium double-cation lead Halide perovskite solar cells, ChemSusChem 11 (2018) 837–842.

(41) X. Gong, S.-H. Lim, J.C. Ostrowski, D. Moses, C.J. Bardeen, G.C. Bazan, Phosphorescence from iridium complexes doped into polymer blends, J. Appl. Phys. 95 (2004) 948–953.

(42) T. Chassé, C.-I. Wu, I.G. Hill, A. Kahn, Band alignment at organic-inorganic semiconductor interfaces: α-NPD and CuPc on InP(110), J. Appl. Phys. 85 (1999) 6589–6592.

(43) Q. Arnoux, A. Boucly, V. Barth, R. Benbalagh, A. Cossaro, L. Floreano, M. Silly, F. Sirotti, E. Derat, S. Carniato, F. Bournel, J.-J. Gallet, D. Fichou, L. Tortech, F. Rochet, Energy-level alignment of a hole-transport organic layer and ITO: Toward applications for organic electronic devices, ACS Appl. Mater. Interfaces 9 (2017) 30992–31004.

(44) P. Vashishtha, S. Bishnoi, C.-H.A. Li, M. Jagadeeswararao, T.J.N. Hooper, N. Lohia, S.B. Shivarudraiah, M.S. Ansari, S.N. Sharma, J.E. Halpert, Recent advancements in near-infrared perovskite light-emitting diodes, ACS Appl. Electron. Mater. 2 (2020) 3470–3490.

(45) Z. Li, Z. Chen, Y. Yang, Q. Xue, H.-L. Yip, Y. Cao, Modulation of recombination zone position for quasi-two-dimensional blue perovskite light-emitting diodes with efficiency exceeding 5%, Nat. Commun. 10 (2019) 1–10. https://doi.org/10.1038/s41467-019-09011-5.

(46) F. Torricelli, D. Zappa, L. Colalongo, Space-charge-limited current in organic light emitting diodes, Appl. Phys. Lett. 96 (2010).

(47) V.I. Arkhipov, H. von Seggern, E.V. Emelianova, Charge injection versus space-charge-limited current in organic light-emitting diodes, Appl. Phys. Lett. 83 (2003) 5074–5076.

(48) Z. Wang, T. Cheng, F. Wang, S. Dai, Z. Tan, Morphology engineering for high-performance and multicolored perovskite light-emitting diodes with simple device structures, Small 12 (2016) 4412–4420.

(49) A. Choudhury, R.K. Gupta, R. Garai, P.K. Iyer, Tuning polymer semiconductor morphology through additive engineering for a stable phototransistor, ACS Appl. Electron. Mater. 3 (2021) 5393–5401.

(50) X. Wu, M.T. Trinh, D. Niesner, H. Zhu, Z. Norman, J.S. Owen, O. Yaffe, B.J. Kudisch, X.-Y. Zhu, Trap states in lead iodide perovskites, J. Am. Chem. Soc. 137 (2015) 2089–2096.

Appendix:

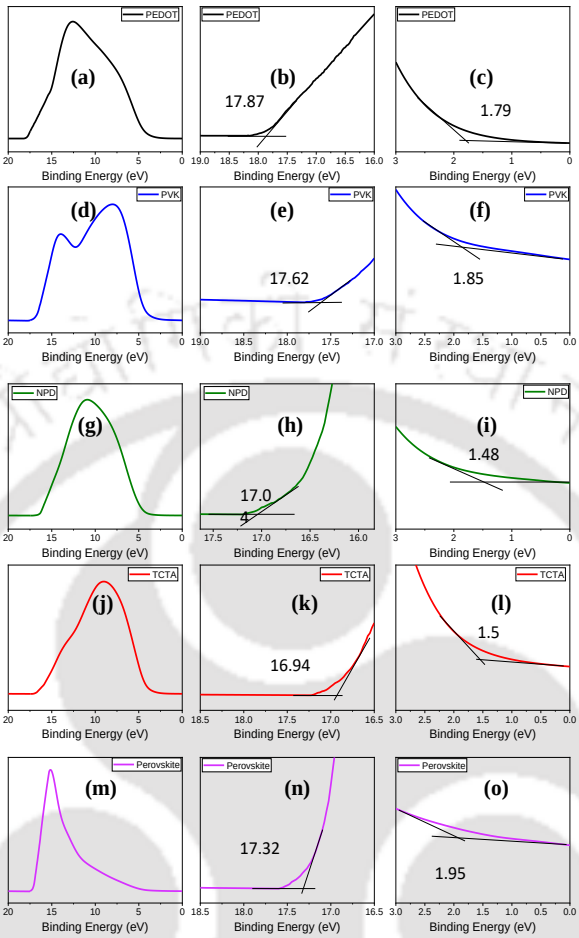

Figure A2.1: UPS analysis of (a, b, c) PEDOT:PSS, (d, e, f) PVK, (g, h, i) NPD, (j, k, l) TCTA, and (m, n, o) perovskite.

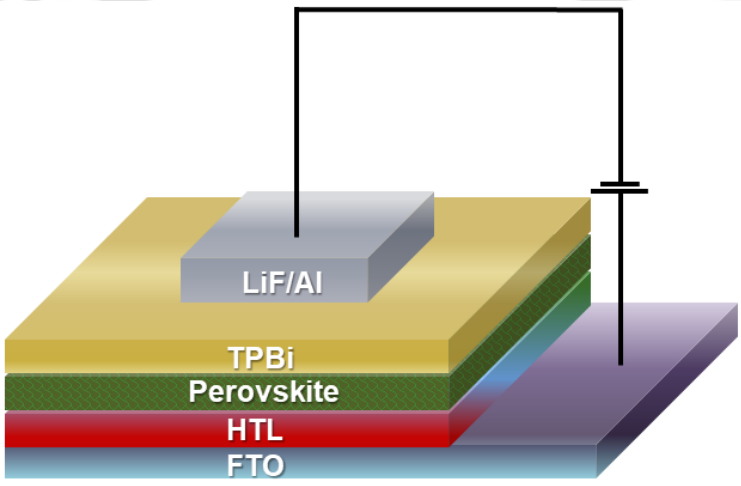

Figure A2.2: Device architecture of Perovskite LED with single HTL.

Table A2.1: Summary of PLED device parameters fabricated with different HTLs.

S.No	Device Parameter	PEDOT:PSS	PVK	NPD	TCTA
1	Turn-on voltage (V_{on})	5.0	4.8	4.7	4.9
2	Luminance ($cd.m^{-2}$)	11,818	16,814	24,343	2,498
3	Current Efficiency(cd/A)	12.1	12.8	16.2	4.2

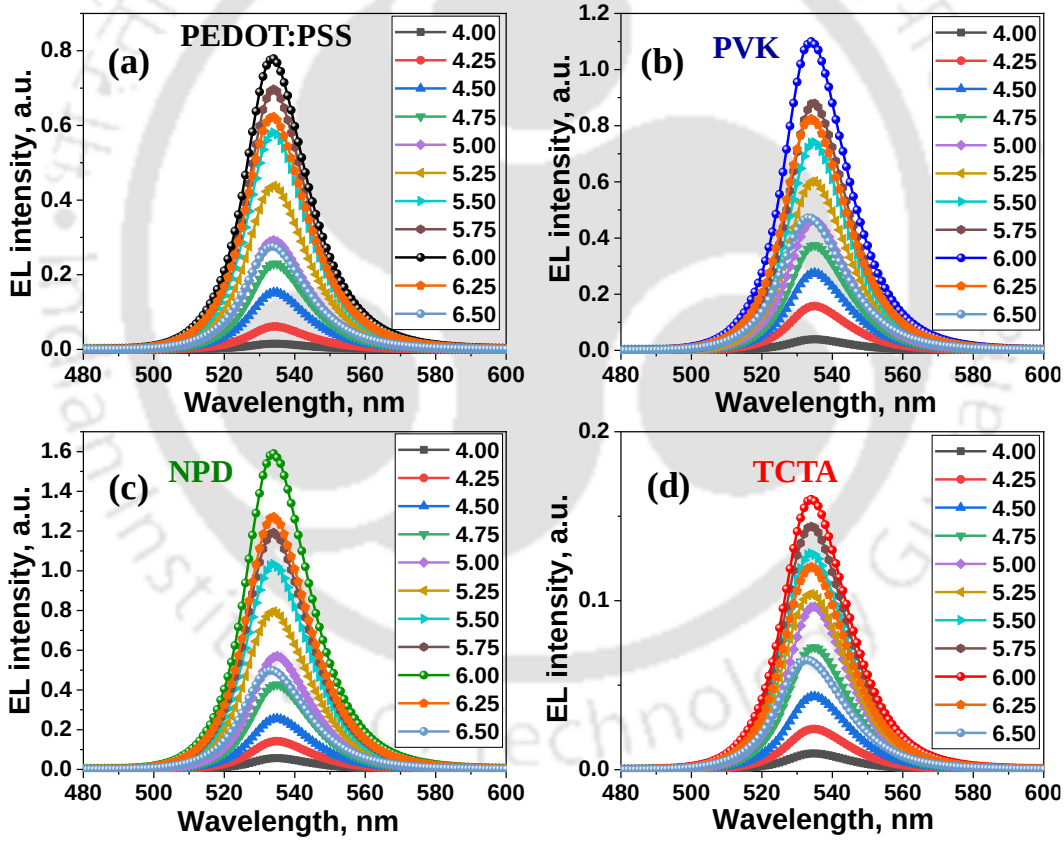

Figure A2.3: EL spectra of PLED devices based on (a) PEDOT:PSS, (b) PVK(c)NPD, and (d)TCTA as HTL at different voltages.

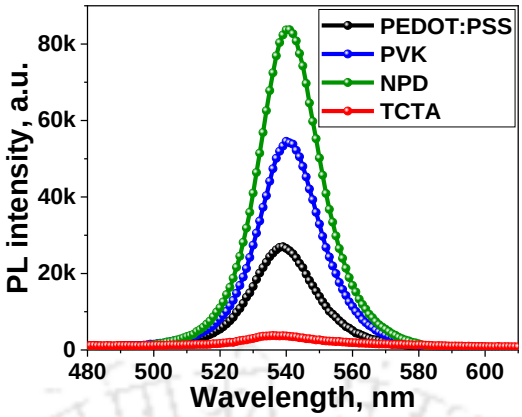

Figure A2.4: Photoluminescence (PL) spectra of perovskite films coated on different HTLs.

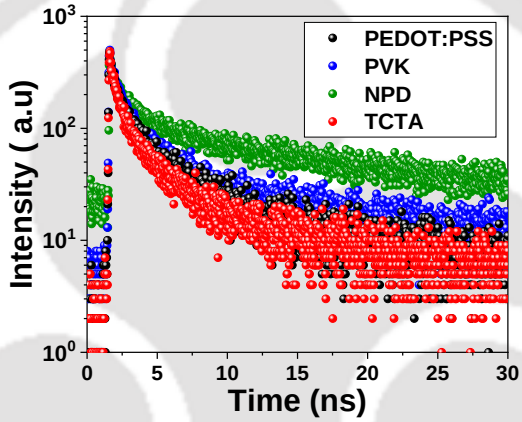

Figure A2.5: Time-resolved photoluminescence (TRPL) study of perovskite films coated on different HTLs.

Table A2.2: Summary of TRPL parameters of perovskite films with different HTLs.

S.No	Type of the sample	τ_1(ns)	τ_2(ns)	τ_{avg}(ns)
1	PEDOT:PSS/$MAPbBr_3$	2.63	44.56	35.92
2	PVK/$MAPbBr_3$	2.81	45.98	39.17
3	NPD/$MAPbBr_3$	3.90	48.60	43.85
4	TCTA/$MAPbBr_3$	1.98	40.72	32.76

[This page was intentionally left blank]

Chapter 3

Dual hole transport layer facilitated efficient perovskite light emitting diode

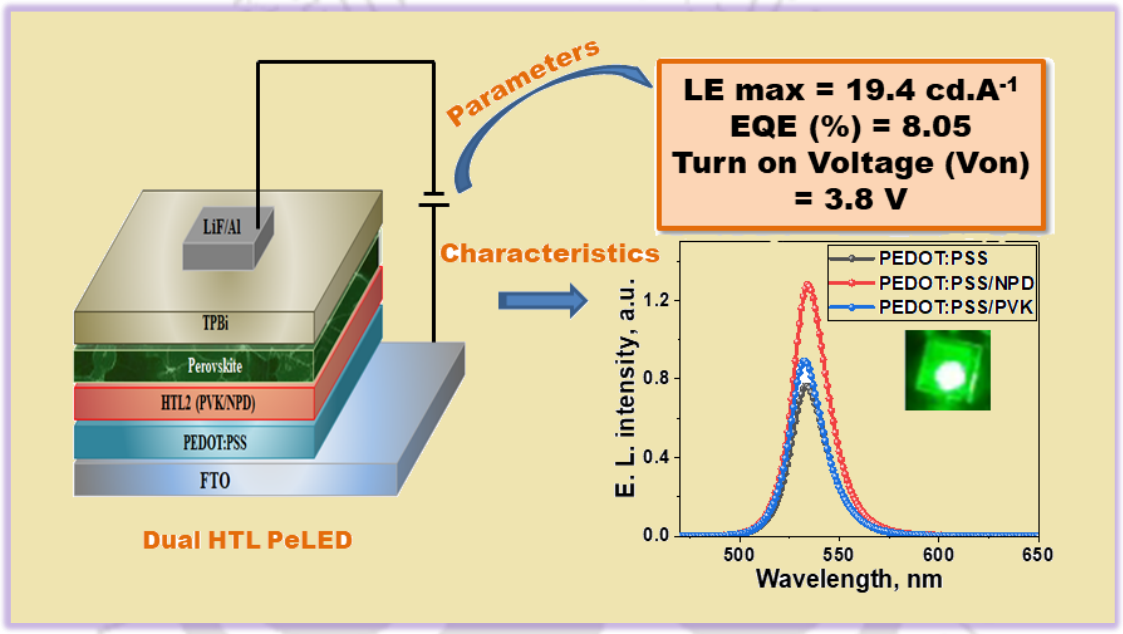

Manuscript: Ramesh Babu Yathirajula, Ritesh Kant Gupta, Mohammad Adil Afroz, Anwesha Choudhury, Himangshu Baishya, and Parameswar Krishnan Iyer. "Dual-Hole-Transport-Layer-Facilitated Efficient Perovskite Light-Emitting Diode." *Physica Status Solidi Applied Research* 220, no. 24 (**2023**): 2300247. DOI: https://doi.org/10.1002/pssa.202300247.

[This page was intentionally left blank]

Abstract

The luminescence and colour purity of solution processable perovskite materials have significantly improved, which makes them a promising candidate for high performance lighting technologies. In this paper, we present a straightforward method for fabricating dual hole transport layers (HTLs) in green-emitting perovskite light emitting diodes (PeLEDs), which significantly helps and charge balance in the emissive layer (EML). By achieving charge balance in the emissive layer, with well-matched energy levels, and lowered charge injection barrier of the transport layers, maximum radiative recombination can be obtained (HTLs). The varying HOMO levels of the HTLs used in the device are in alignment with the work function of the FTO and HOMO of the emissive layer. The PEDOT: PSS/NPD-based PeLED device showed outstanding performance with a maximum brightness of 19625 cd m^{-2}, the highest current efficiency of 19.2 cd A^{-1}, and turn-on voltage of 3.8 V among the all three HTL combination. The reason for these higher results was the well-match HOMO of PEDOT: PSS and NPD with both the anode and emissive layer facilitating better hole injection and charge balance. CIE coordinates (0.22, 0.74) for pure green emission are supported by studies utilizing photoluminescence and electroluminescence. The best film morphology and crystallinity with less pinholes were found in perovskite films made on top of PEDOT:PSS/NPD, which allowed for efficient charge transport.

3.1 Overview

The light-emitting diode (LED) technology has been growing since its invention in the year 1960, increasing its importance in order to transform it into a better energy efficient, longer life, durable lighting and display technologies.[1,2,3] 3D Organic-Inorganic Halide (OIHP) based perovskite represented by the general formula ABX3, where A is organic and or inorganic cation (MA^+, FA^+, Cs^+, Rb^+), B is the divalent metal cation (Pb^{2+}, Ge^{2+}, Sn^{2+}) and X is the halide anions (I^-, Br^-, Cl^-) has got enormous research interest in the field of solid-state light-emitting diode after photovoltaic technology.[4] The advantages of perovskite material over the conventional semiconducting materials are its low temperature and solution processibility, high charge carrier mobility, superior spectral purity, high brightness, and most importantly easy colour tunability by changing halide compositions makes it a potential material for next generation lighting and displaying technology.[5-11] Methyl ammonium lead bromide ($MAPbBr_3$) is the widely studied perovskite material for green light emission perovskite LEDs (PeLEDs) due to its easy film formation process.[12,13] However, the low photoluminescence (PL) emission restricts its uses in the efficient light-emitting application. The reason behind the low light emission is directly related to the crystal growth process and hence the grain size of the perovskite film during its nucleation process.[14, 15] The morphology of the perovskite film is playing a crucial role in the solution processed perovskite material.[16,17] The fine morphology engineering has been done without using any additive molecule in order to obtain a pinhole free low surface roughness perovskite film with the help of different anti-solvents in one step spin coating methods.[18,19]

In addition to the morphology and crystallinity of the emissive layer, the charge injection layers must also meet certain requirements in order to increase the device's stability and efficiency. These requirements include good chemical and physical stability, favorable energy level alignment with the emissive layer, effective transport of only one type of charge carriers while blocking opposite carriers, and favorable surface properties for the growth of additional layers on top of that layer.[20,21] Because of the low surface roughness produced at the FTO and perovskite interface for effective hole injection to the emissive layer, Poly(3,4-ethylenedioxythiophene)- poly(styrenesulfonate) (PEDOT:PSS) has been utilized extensively as a hole transport layer (HTL) in various p-i-n architecture based PeLED devices.[22] However, large energy gap between the HOMO of $MAPbBr_3$ perovskite and PEDOT:PSS hinder the hole injection to the perovskite layer (EML) resulted non-radiative recombination of holes takes place at the interface of the HTL and EML.[23] The injection barrier between HTL and EML must be reduced for enhancing hole injection and, consequently, the device's electroluminescence. Again, due to the small injection barrier between the 2,2',2''-(1,3,5-Benzinetriyl)-tris(1-phenyl-1-H-benzimidazole) (TPBi), electron injection layer (EIL) and perovskite a significant amount of electron can inject to the EML. Thus, the unbalance charge injection into the EML lead to enhancement in both the non-radiative recombination and turn-on voltage of the device.[24] In order to improve device performance Wang et al. reported a dual HTL (TFB/PVK) to minimize the hole injection barrier and hence to obtained the balance charge injection to the EML.[25]

In this work, we have fabricated a dual HTL p-i-n architecture based PeLED device. In order to improve the hole injection a dual HTL architecture is adopted (Figure S1) comprising of poly(9-vinylcarbazole) (PVK)/ N,N′-Bis(naphthalen-1-yl)-N,N′-bis(phenyl)-2,2′-dimethylbenzidine (NPD) along with the PEDOT:PSS HTL. The PEDOT:PSS/NPD dual layer HTL shows better crystallinity and less pinhole film compared to the only PEDOT:PSS and PEDOT:PSS/PVK dual HTL, as a result the better charge injection is feasible to the EML and hence improves the electroluminescence intensity remarkably and the turn on voltage of the device minimizes to 3.8V.

Through careful selection of the HTLs, PeLEDs with $MAPbBr_3$ as the emissive layer are optimized in this study by choosing among PEDOT:PSS, PVK, and NPD. The work function or HOMO of the chosen HTLs can be used to tune the barrier for hole injection, which causes the brightness of the PeLED to vary. The device based on PEDOT:PSS/NPD, which has a HOMO well matched with the HOMO of perovskite and a work function of FTO, has the highest luminance of 19625 cd m^{-2}. As a result, the emissive layer's charge balancing and hole injection were improved. The output light has CIE coordinates of (0.22, 0.74) and is entirely green. The electroluminescence (EL) and photoluminescence (PL) peaks were identified at 534 and 528 nm, respectively. Studies using time-resolved photoluminescence (TRPL) spectroscopy also revealed that PEDOT:PSS/ NPD based perovskite film has the longest carrier lifetime which is favourable for the efficient transport of charge to the EML. Moreover, field emission scanning electron microscopy (FESEM) morphological observations of the perovskite on top of each HTL layer were analyzed.

3.2 Experimental Section

3.2.1 Materials

Fluorine doped tin oxide (FTO) coated glass (7Ω/sq.), Lead bromide (PbBr2,99.8%),Methyl ammonium bromide (MABr, 99%), DMF (anhydrous, 99.8%), DMSO (anhydrous, 99.8%), Chloroform (anhydrous, 99.8%), PVK(poly(9-vinylcarbazole)), N,N′-Bis(naphthalen-1-yl)-N,N′-bis(phenyl)-2,2′-dimethylbenzidine (NPD) and Tris(4-carbazoyl-9-ylphenyl)amine (TCTA), Lithium fluoride (LIF) and Aluminum (Al) were purchased from Sigma-Aldrich. Poly (3,4-ethylenedioxythiophene) polystyrene sulfonate (PEDOT:PSS, PVP AI 4083) was purchased from Clevios. 2,2',2''-(1,3,5-Benzinetriyl)-tris(1-phenyl-1-H-benzimidazole).(TPBi) was purchased from was purchased from LUMTEC.

3.2.2 Device Fabrication

The perovskite light emitting diodes (PLEDs) were fabricated on FTO coated glass which was prepatterned and cleaned consecutively in soap solution, de-ionized water, acetone, and isopropanol. The substrate was then dried under N_2 gas and UV-ozone treated before further processing. Thereafter, the as purchased PEDOT:PSS was coated at 4000 rpm for 45 s for the PEDOT:PSS-based PLED. For the remaining two types of PLED, PEDOT:SS/NPD and

PEDOT:PSS/PVK , first PEDOT:PSS was coated at 6000 rpm for 45 s and secondly NPD and PVK were taken at 15 mg/mL each with chlorobenzene as processing solvent and coated at 6000 rpm for 45 s. All the coated HTLs were annealed at 120 ºC for 30 min. All the coated HTLs were approximately 40 nm. The perovskite precursor solution was prepared by dissolving MABr and $PbBr_2$ with a 1.1:1 in anhydrous DMF and DMSO (7:3) to give a concentration of 30 wt.%. Then the solution is stirred at 70^{o}C for 2 hours to make sure all the solutes are soluble. Then, the substrates were transferred to spin coater chuck for two step spin coating method to obtain the perovskite films. In step 1 the chuck is rotated at 500 rpm for 5 s for uniform spreading of the precursor solution on the substrate. In step 2, the speed of the chuck is increased to 3000 rpm for 50 s and after 10 s of step 2, chloroform (100 μL) is dripped slowly for anti-solvent treatment. Thereafter, the perovskite films are annealed at 70 °C for 15 min to obtain ~90 nm thick films. Finally, TPBi (40 nm), LiF (1 nm) and Al (100 nm) were vapor deposited at a base pressure of 10^{-6} mbar at a rate of 0.5, 0.1 and 1.0Å/s, respectively. The active area of the PLEDs was 25 mm^2. The overall device architecture was FTO/HTL/Perovskite/TPBi/LiF/Al.

3.2.3 Characterization

The morphology of perovskite samples was examined on scanning electron microscopy (SEM, JEOL JSM-7610F). Perovskite films were characterized by X-ray diffraction (XRD, Rigaku Micromax-007HF diffractometer equipped with Cu Kα1 irradiation [λ =1.54184Å]), UV–vis absorption spectroscopy (PerkinElmer Lambda-35). Photoluminescence studies were recorded using a fluorescence spectrophotometer (HORIBA JobinYvon, fluoromax-4 with a 405 nm laser excitation).Time-resolved fluorescence studies were performed using an Edinburgh Life Spec II instrument. The current density versus voltage (J-V) characteristics of the perovskite LEDs were measured using a Keithley 2400 source meter, whereas the luminance versus voltage (L-V) characteristics and the EL spectra were recorded using Konica Minolta CS 2000 Spectroradiometer.

3.3 Results and Discussions

Figure 3.1a illustrates the chemical structure of each of the three HTLs employed in this work PEDOT:PSS, PVK and NPD. The energy band diagram of PeLEDs with various HTLs is shown in **Figure 3.1b**. For an LED, the electron transport layer (ETL) and HTLs

must be chosen in a way that makes it simple to inject electrons into the lowest unoccupied molecular orbital (LUMO) of the emissive layer and holes into the emissive layer's HOMO. To ensure that the bulk of the injected electron and hole pairs can recombine radiatively, it is crucial to carefully choose the ETL and HTL.

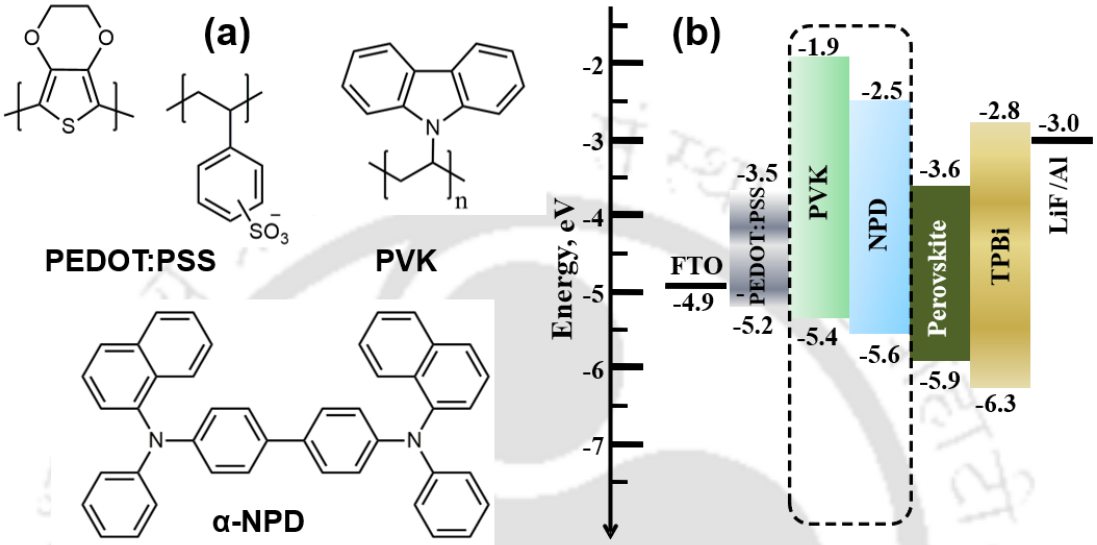

Figure 3.1: (a) Chemical structures of the three hole transport layers and (b) energy band diagram for a perovskite LED made with $MAPbBr_3$ as the emissive layer.

Since TPBi has been shown to be a very good electron injecting material and also works well to prevent the transit of holes from the emissive layer, it is utilised as the industry standard for ETLs. The HOMO should also be well-matched to the work function of the transparent conducting oxides (FTO) as well as the perovskite layer on the HTL side. Based upon this, three HTLs are chosen so that the HOMOs are positioned between the work function of the FTO and the HOMO of the emissive layer. The HOMOs of PVK and NPD are 5.4 and 5.6 eV, whereas the work function of PEDOT:PSS is 5.1 eV. The HOMO of the perovskite layer still exhibits some energy barrier/offset in the work function of PEDOT:PSS and PVK. However, because the energy offset between the HOMO of NPD and both perovskite and FTO is intermediate, it is anticipated to have smoother hole injection from FTO to perovskite and improved charge balance at the emissive layer. This will make it possible to build the recombination zone away from the transport layers and considerably increase radiative recombination. The architecture FTO/PEDOT:PSS/HTL2/ Perovskite/TPBi/LiF/Al was used

to fabricate PeLED devices with various HTL layers (**Figure A3.1**). All three PeLEDs' current density-voltage (J-V) curves (**Figure 3.2a**) exhibit good diode characteristics and are exponential in form, indicating that the current is injection restricted at low voltages and space charge limited at high voltages. The J-V curve reveals that the PEDOT:PSS/NPD based PeLED has a greater current density value than the other devices. The HOMO level of NPD has significant intermediate energy value that facilitate easy injection of hole from PEDOT:PSS to perovskite layer. This demonstrates that additional charges can be introduced into the perovskite emissive layer, increasing the recombination current. This led to a PEDOT:PSS/NPD based PeLED having a minimum turn-on voltage (Von) of 3.8 V while PEDOT:PSS and PEDOT:PSS/PVK based PeLEDs, have Von of 4.47 and 4.2 V respectively (**Figure A3.2**).

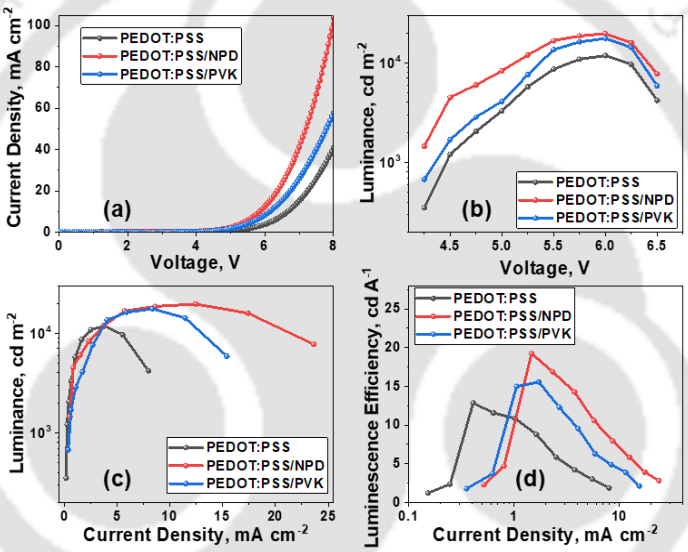

Figure 3.2: (a) current density Vs voltage, (b) luminance Vs voltage, (c) luminance Vs current density and (d) current efficiency Vs current density curves of PeLEDs with different HTLs.

Figure 3.2b shows the luminance curve for each PeLED device with respect to voltages. The PEDOT:PSS/NPD based device has the highest brightness of 19625 cd m^{-2} at 6 V, making it one of the best $MAPbBr_3$ based PeLEDs. The brightness values for the remaining HTLs are, respectively, 11818 and 17594 cd m^{-2} for PEDOT:PSS and PEDOT:PSS/PVK based PeLEDs operating at 6 V. The energy offset between FTO and NPD is larger compared to that of FTO and PVK. However, it is equally important to highlight that the energy offset between NPD and the HOMO of the perovskite presents itself as slightly smaller than the energy offset

between PVK and the perovskite's HOMO. This has most likely allowed better hole injection to the perovskite layer through the second HTL layer of NPD than that of PVK, thus creating an efficient charge injection into the perovskite emissive layer that leading to the highest brightness.

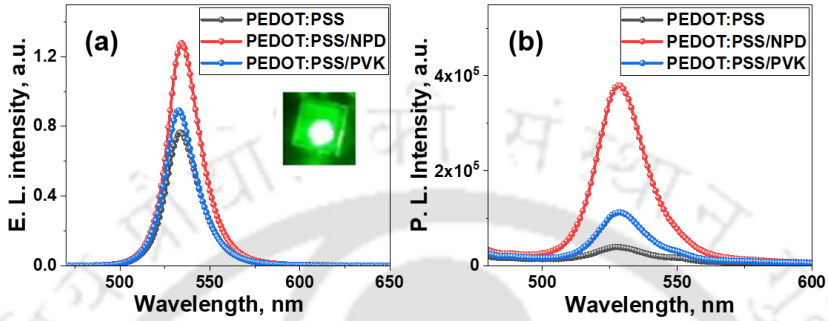

Figure 3.3: (a) EL spectra for PEDOT:PSS, PEDOT:PSS/NPD and PEDOPT:PSS/PVK based PeLEDs att 6 V and inset showing green emission of NPD based working PeLED, and (b) PL spectra for PEDOT:PSS, PEDOT:PSS/NPD and PEDOPT:PSS/PVK based PeLEDs.

Figures 3.2c and 3.2d, respectively, show the variation in brightness and current efficiency with regard to current density. After reaching the highest value of brightness for each combination HTLs, it drops with increasing current densities. In contrast to the other HTLs, it is clear that the brightness roll-off for PEDOT:PSS/NPD based PeLEDs happens at a significantly greater current density. The PEDOT:PSS is well-aligned with the NPD's bands which most likely made it easier for holes to be injected into the emissive layer, allowing for the maximum luminance at greater current densities. Nonetheless, it is clear that the brightness roll-off for PEDOT:PSS/NPD based PeLEDs happens at a much greater current density than for the other HTLs. The high brightness at higher current densities was made possible by the well-matched band alignment of PEDOT: PSS/NPD, which probably made it easier for the holes to be injected in the emissive layer. Similar to voltage efficiency, current efficiency is similarly at its peak at a specific current density value and declines with greater current densities. The PEDOT:PSS/NPD based PeLED has the highest current efficiency, 19.2 cd A^{-1}. PeLEDs based on PEDOT:PSS and PEDOT:PSS/PVK exhibit current efficiencies of 12.8, and 14.9. In **Table A3.1**, all the device parameters are listed. The EL

spectra for all four HTLs are shown in **Figure A3.3** with a bias voltage range of 4.0–6.5 V and a step size of 0.25 V. The EL spectra's peak remains consistent at ~533 nm for all three HTLs, indicating that the EL peak is stable for various voltages for all three HTLs. All four PeLEDs' EL spectra at 6 V are depicted in **Figure 3.3a**. The image of an operational LED is displayed in the inset of **Figure 3.3a**. Compared to the other two HTL based PeLEDs, the EL intensity of the PEDOT:PSS/NPD based PeLED is higher. In contrast to the other three PeLED devices, the PEDOT:PSS/NPD based device has a greater radiative recombination rate because the emissive layer's efficient hole injection produces superior charge balance. All PeLED devices have been found to have a full width half maximum (FWHM) of ~22 nm and a peak of ~533nm. The PL of the perovskite emissive layer on various HTLs is shown in **Figure 3.3b**. All samples' PL Peaks are discovered at 528 nm, supporting the case for good green emitters. The perovskite film made of PEDOT:PSS/NPD has the highest PL intensity, indicating the greatest amount of radiative recombination of the produced charges. The PEDOT:PSS/NPD based PeLED may exhibit the maximum brightness value when compared to the other two PeLED devices for this reason.

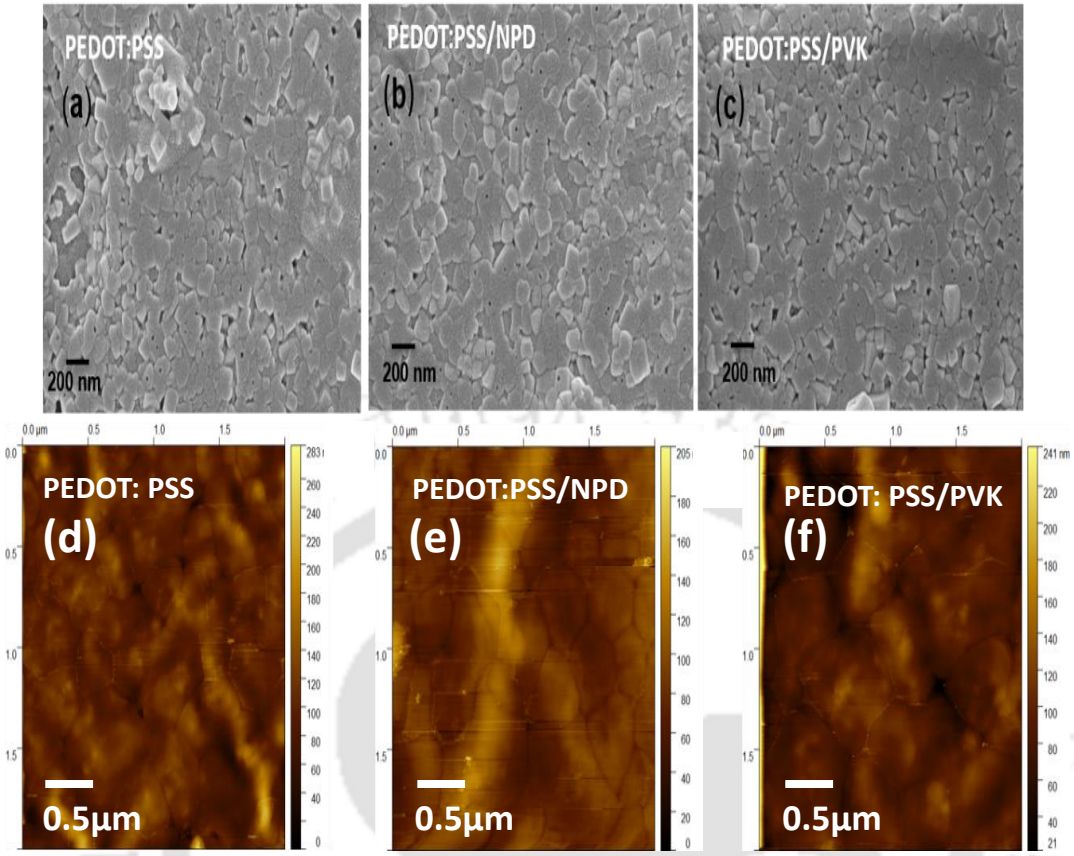

Figure 3.4: (a-c) Field emission scanning electron microscopy images for perovskite films based on PEDOT:PSS, PEDOT:PSS/NPD and PEDOT:PSS/PVK as HTLs, and (d-f) AFM images of the perovskite film coated on the top of PEDOT:PSS, PEDOT:PSS/NPD and PEDOT:PSS/PVK HTL combinations.

Figure 3.4a-c, depicts the morphology of the perovskite films coated on each HTLs combination (FESEM). In all cases, the perovskite films exhibited small crystalline domains when coated on top of the HTL layers. Notably, when PEDOT:PSS/PVK was employed as the HTL, these domains became more prominent, indicating a less uniform and compact morphology. However, when the perovskite film was coated on top of PEDOT:PSS/NPD as the HTL, a smooth and compact morphology was observed. Furthermore, AFM imaging (**Figure 3.4d-f**) of the perovskite film shows the RMS roughness value of 31.6 nm, 22.35 nm and 26.8 nm, for the PEDOT:PSS, PEDOT:PSS/NPD and PEDOT:PSS/PVK HTL combinations respectively. This distinct morphology of the perovskite film in the PEDOT:PSS/NPD combination is advantageous for the charge transport process within the

device. Additionally, the incorporation of PEDOT:PSS/NPD as the hole transport layer (HTL) led to a notable reduction in grain boundaries within the perovskite film. This beneficial effect is also reflected in the trap-filled limited voltage (V_{TFL}) measurements conducted on the hole-only devices (**Figure A3.4**). The V_{TFL} of the PEDOT:PSS/NPD based device exhibited a decrease from 3.1V to 2.9V, in contrast to the device using PEDOT:PSS/PVK. Moreover, an evaluation of trap density (η_t), as determined using **equation A3.1**, demonstrated a decrease in trap density for the PEDOT:PSS/NPD hole-only device, shifting from $3.16x10^{15}$ cm^{-3} to $2.94x10^{15}$ cm^{-3} when compared to the PEDOT:PSS/PVK based hole only device. This reduction is crucial as it helps to minimize non-radiative recombination of injected charge carriers, a process that can lead to energy roll off within the device [26] which was confirmed by the improved charge carrier mobility value from $0.54x10^{-7}$ $cm^2V^{-1}s^{-1}$ to $0.83x10^{-7}$ $cm^2V^{-1}s^{-1}$ in PEDOT:PSS/NPD based device compared to PEDOT:PSS/PVK based device calculated using **equation A3.2**. The chromaticity coordinates of the fabricated PeLEDs are shown in (**Figure A3.5**) by the Commission Internationale de I'Eclairage (CIE). The CIE coordinates for PeLEDs, as seen in this figure, are about (0.22, 0.74), which denotes pure green emission. The comparison parameters in all the device configurations are presented (**Table A3.1**). An X-ray diffraction (XRD) study is carried out to further establish the crystallinity of the perovskite emissive layer deposited on top of various single and dual HTLs (**Figure A3.6**). For all perovskite films, the XRD spectra showed two distinct and strong diffraction peaks at 14.95°, 30.15°, and 33.90°, which are, respectively, the (100), (200), and (210) planes of cubic $MAPbBr_3$. In comparison to the other three films, PEDOT:PSS/NPD based perovskite films exhibit exceptional crystallinity and preferred diffraction peak orientation. To determine the lifetime of the photo-generated charge carriers, we performed bi-exponential fitting of the time-resolved photoluminescence (TRPL) spectra (**Figure A3.7**). The TRPL spectra exhibited two distinct decay times, reflecting the behavior of excited charge carriers: (i) a fast decay time ($\tau1$) attributed to trap-assisted recombination and (ii) a slower decay time ($\tau2$) associated with radiative recombination occurring in most of the emissive layer (**Table A3.2**). For the devices utilizing PEDOT:PSS, PEDOT:PSS/NPD, and PEDOT:PSS/PVK as the HTLs, the estimated values for $\tau1$ were found to be 2.57 ns, 4.27 ns, and 2.64 ns, respectively. On the other hand, the estimated values for $\tau2$ were 43.20 ns, 49.55 ns, and 47.11 ns for the respective HTL

combinations. The average charge carrier lifetime (τ_{avg}) was then determined based on the estimated values for $\tau 1$ and $\tau 2$. For the PEDOT:PSS, PEDOT:PSS/NPD, and PEDOT:PSS/PVK devices, the calculated average charge carrier lifetimes were found to be 32.18 ns, 45.78 ns, and 35.69 ns, respectively. The longer average charge carrier lifetime in the PEDOT:PSS/NPD device suggests more efficient charge transport and reduced non-radiative recombination, contributing to its superior PL intensity. [27,28]

3.4 Conclusions

In summary, we presented a simple method by using PEDOT:PSS and NPD as dual HTLs, and we were able to demonstrate that a PeLED based on PEDOT:PSS/NPD will perform the best and offer a high efficiency PeLED. Through careful dual HTL selection, high brightness PeLEDs based on $MAPbBr_3$ were fabricated, enabling efficient hole injection and charge balance in the emissive layer. The impact of the hole injection barrier and the hole transport characteristics of different HTLs are explored in terms of morphology, crystallinity, charge transport and luminescence which shows highest brightness of 19625 cd m^{-2} at 6 V and current efficiency of 19.2 cd A^{-1} in the PEDOT:PSS/NPD based dual HTL PeLED device. The results are strongly supported by electrical, morphological, and photo-physical characterizations. The PEDOT:PSS/NPD based PeLED showed an EL peak at 533 nm which was a clear green in colour. The emissive layer was able to establish charge balance attributed to PEDOT:PSS and NPD acting as dual HTL, which resulted in the enhancement of the radiative recombination in the EML.

References

(1) M.-H. Chang, D. Das, P.V. Varde, M. Pecht, Light emitting diodes reliability review, Microelectron. Reliab. 52 (2012) 762–782.

(2) D. Das, P. Gopikrishna, D. Barman, R.B. Yathirajula, P.K. Iyer, White light emitting diode based on purely organic fluorescent to modern thermally activated delayed fluorescence (TADF) and perovskite materials, Nano Converg. 6 (2019) 31.

(3) D. Das, P. Gopikrishna, D. Barman, R.B. Yathirajula, P.K. Iyer, Substantial efficiency enhancement in solution processed phosphorescent light emitting diode with polymer host: Efficient optimization of charge balance and processing conditions, J. Phys. Chem. Solids. 163 (2022) 110577.

(4) K. Ji, M. Anaya, A. Abfalterer, S.D. Stranks, Halide perovskite light-emitting diode technologies, Adv. Opt. Mater. 9 (2021) 2002128.

(5) C. Wehrenfennig, G.E. Eperon, M.B. Johnston, H.J. Snaith, L.M. Herz, High charge carrier mobilities and lifetimes in organolead trihalide perovskites, Adv. Mater. 26 (2014) 1584–1589.

(6) A. Kojima, K. Teshima, Y. Shirai, T. Miyasaka, Organometal halide perovskites as visible-light sensitizers for photovoltaic cells, J. Am. Chem. Soc. 131 (2009) 6050–6051.

(7) X.-K. Liu, W. Xu, S. Bai, Y. Jin, J. Wang, R.H. Friend, F. Gao, Metal halide perovskites for light-emitting diodes, Nat. Mater. 20 (2021) 10–21.

(8) L. Zhang, X. Yang, Q. Jiang, P. Wang, Z. Yin, X. Zhang, H. Tan, Y.M. Yang, M. Wei, B.R. Sutherland, E.H. Sargent, J. You, Ultra-bright and highly efficient inorganic based perovskite light-emitting diodes, Nat. Commun. 8 (2017) 15640.

(9) Y.-H. Kim, H. Cho, J.H. Heo, T.-S. Kim, N. Myoung, C.-L. Lee, S.H. Im, T.-W. Lee, Multicolored organic/inorganic hybrid perovskite light-emitting diodes, Adv. Mater. 27 (2015) 1248–1254.

(10) J.S. Kim, J.-M. Heo, G.-S. Park, S.-J. Woo, C. Cho, H.J. Yun, D.-H. Kim, J. Park, S.-C. Lee, S.-H. Park, E. Yoon, N.C. Greenham, T.-W. Lee, Ultra-bright, efficient and stable perovskite light-emitting diodes, Nature. 611 (2022) 688–694.

(11) Y. Jiang, C. Sun, J. Xu, S. Li, M. Cui, X. Fu, Y. Liu, Y. Liu, H. Wan, K. Wei, T. Zhou, W. Zhang, Y. Yang, J. Yang, C. Qin, S. Gao, J. Pan, Y. Liu, S. Hoogland, E.H. Sargent, J. Chen, M. Yuan, Synthesis-on-substrate of quantum dot solids, Nature. 612 (2022) 679–684.

(12) Z. Wang, T. Cheng, F. Wang, S. Dai, Z. Tan, Morphology engineering for high-performance and multicolored perovskite light-emitting diodes with simple device structures, Small. 12 (2016) 4412–4420.

(13) P. Chen, Z. Xiong, X. Wu, M. Shao, X. Ma, Z.-H. Xiong, C. Gao, Highly efficient perovskite light-emitting diodes incorporating full film coverage and bipolar charge injection, J. Phys. Chem. Lett. 8 (2017) 1810–1818.

(14) H. Cho, S.-H. Jeong, M.-H. Park, Y.-H. Kim, C. Wolf, C.-L. Lee, J.H. Heo, A. Sadhanala, N. Myoung, S. Yoo, S.H. Im, R.H. Friend, T.-W. Lee, Overcoming the electroluminescence efficiency limitations of perovskite light-emitting diodes, Science. 350 (2015) 1222–1225.

(15) M. Hossain, R. Garai, R.K. Gupta, R.N. Arunagirinathan, P.K. Iyer, Fluoroarene derivative based passivation of perovskite solar cells exhibiting excellent ambient and thermo-stability achieving efficiency >20%, J. Mater. Chem. C 9 (2021) 10406–10413.

(16) R. Garai, R.K. Gupta, A.S. Tanwar, M. Hossain, P.K. Iyer, Conjugated polyelectrolyte-passivated stable perovskite solar cells for efficiency beyond 20%, Chem. Mater. 33 (2021) 5709–5717.

(17) R.K. Gupta, R. Garai, P.K. Iyer, Ambient stable perovskite solar cells through trifluoro acetic acid-mediated multifunctional anchoring, ACS Appl. Energy Mater. 5 (2022) 1571–1579.

(18) W.S. Subhani, K. Wang, M. Du, X. Wang, N. Yuan, J. Ding, S. (frank) Liu, Anti-solvent engineering for efficient semitransparent CH3NH3PbBr3 perovskite solar cells for greenhouse applications, J. Energy Chem. 34 (2019) 12–19.

(19) J. Li, R. Yang, L. Que, Y. Wang, F. Wang, J. Wu, S. Li, Optimization of anti-solvent engineering toward high performance perovskite solar cells, J. Mater. Res. 34 (2019) 2416–2424.

(20) V.M. Le Corre, M. Stolterfoht, L. Perdigón Toro, M. Feuerstein, C. Wolff, L. Gil-Escrig, H.J. Bolink, D. Neher, L.J.A. Koster, Charge transport layers limiting the efficiency of perovskite solar cells: How to optimize conductivity, doping, and thickness, ACS Appl. Energy Mater. 2 (2019) 6280–6287.

(21) L.E. Polander, P. Pahner, M. Schwarze, M. Saalfrank, C. Koerner, K. Leo, Hole-transport material variation in fully vacuum deposited perovskite solar cells, APL Mater. 2 (2014) 081503.

(22) M.A. Afroz, R.K. Gupta, R. Garai, M. Hossain, S.P. Tripathi, P.K. Iyer, Crystallization and grain growth regulation through Lewis acid-base adduct formation in hot cast perovskite-based solar cells, Org. Electron. 74 (2019) 172–178.

(23) S. Li, Y.-L. Cao, W.-H. Li, Z.-S. Bo, A brief review of hole transporting materials commonly used in perovskite solar cells, Rare Metals. 40 (2021) 2712–2729.

(24) Q.-W. Liu, S. Yuan, S.-Q. Sun, W. Luo, Y.-J. Zhang, L.-S. Liao, M.-K. Fung, Interfacial engineering for highly efficient quasi-two dimensional organic–inorganic hybrid perovskite light-emitting diodes, J. Mater. Chem. C Mater. Opt. Electron. Devices. 7 (2019) 4344–4349.

(25) W. Wang, Z. Wu, T. Ye, S. Ding, K. Wang, Z. Peng, X.W. Sun, High-performance perovskite light-emitting diodes based on double hole transport layers, J. Mater. Chem. C 9 (2021) 2115–2122.

(26) Z. Ni, S. Xu, H. Jiao, H. Gu, C. Fei, J. Huang, High grain boundary recombination velocity in polycrystalline metal halide perovskites, Sci. Adv. 8 (2022).

(27) Z. Wang, T. Cheng, F. Wang, S. Dai, Z. Tan, Morphology engineering for high-performance and multicolored perovskite light-emitting diodes with simple device structures, Small. 12 (2016) 4412–4420.

(28) X. Hu, Y. Xie, C. Geng, S. Xu, W. Bi, Study on the color compensation effect of composite orange-red quantum dots in WLED application, Nanoscale Res. Lett. 15 (2020) 118.

Appendix:

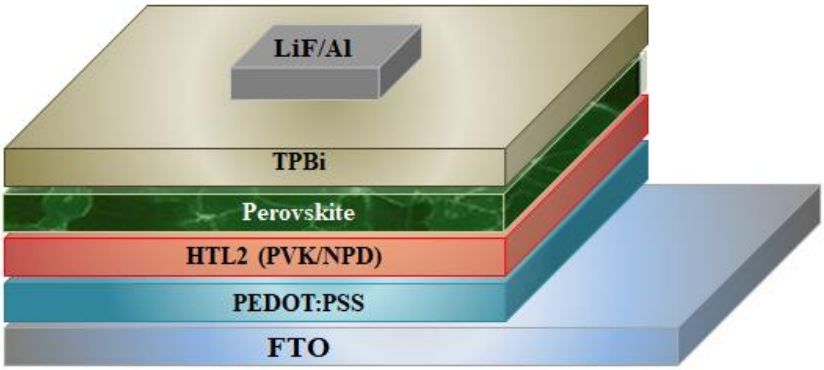

Figure A3.1: Device architecture of dual HTL based Perovskite LED.

Table A3.1: Summary of PLED device parameters fabricated with different HTLs.

S.No	Device Parameter	PEDOT:PSS	PEDOT:PSS/NPD	PEDOT:PSS/PVK
1	Luminance (cd/m^2)	11,818	19,625	17,594
2	Current Efficiency(cd/A)	12.8	19.2	14.9
3	External Quantum Efficiency (EQE,%)	5.37	8.05	6.72
4	CIE-Co-ordinates (x,y)	(0.21,0.75)	(0.22,0.74)	(0.21,0.74)
5	Peak-wavelength (λpeak) (nm)	533	533	534
6	Turn-on-Voltage (V)	4.4	3.8	4.2

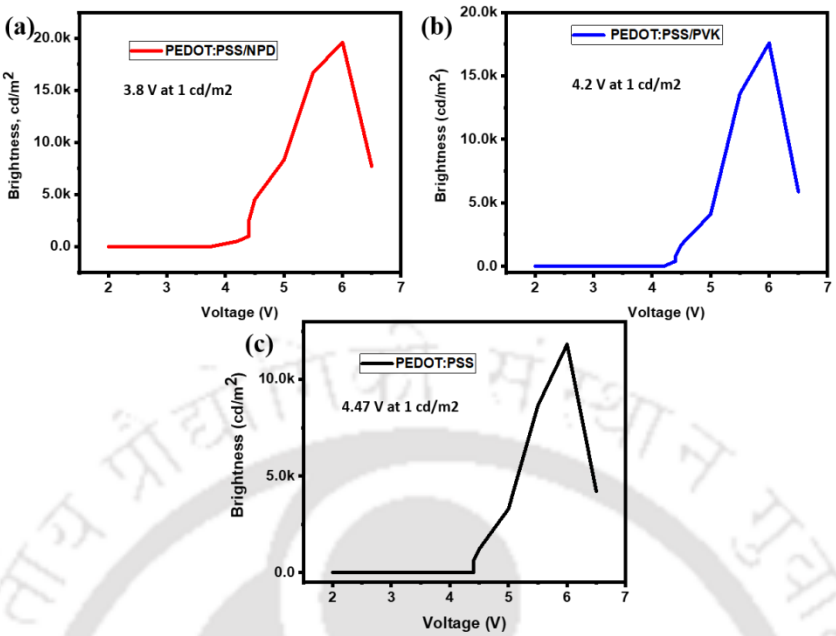

Figure A3.2: Brightness vs Voltage plot of (a) PEDOT:PSS/NPD, (b) PEDOT:PSS/PVK and (c)PEDOT:PSS as HTL based PeLEDs. (**Voltage measured at 1 cd.m^{-2}**).

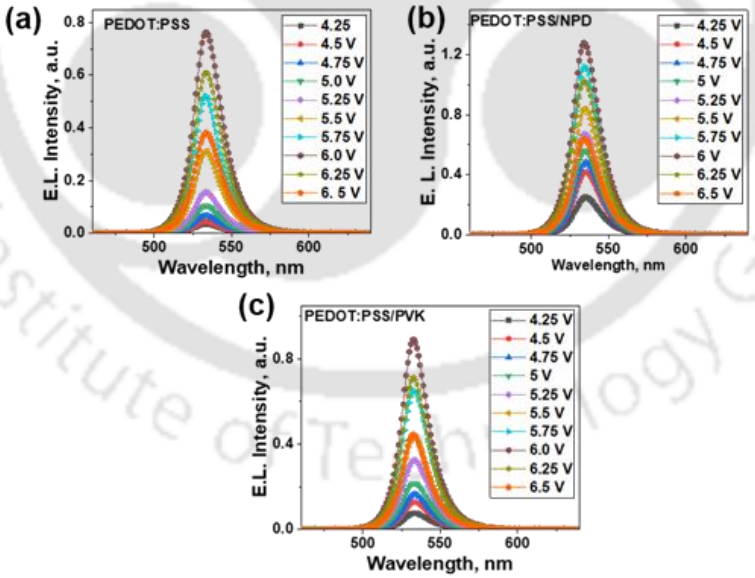

Figure A3.3: EL spectra of PLED devices based on (a) PEDOT:PSS, (b) PEDOT:PSS/NPD and (c)PEDOT:PSS/PVK as HTL at different voltages.

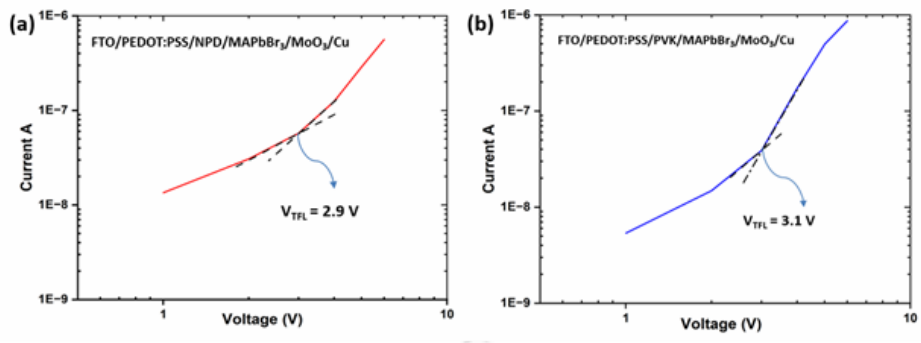

Figure A3.4: Hole only device for (a) PEDOT:PSS/NPD, (b) PEDOT:PSS/PVK HTL combination for trap filled limited voltage (V_{TFL}) and trap density (η_t)calculation.

Equation-A3.1: Trap density (η_t)= $2\varepsilon\varepsilon_o V_{TFL} / (eL^2)$

Where, ε= relative permittivity (~25.5)

ε_o = vacuum permittivity

e = elementary charge

L = thickness of perovskite layer

Equation-A3.2: Hole Mobility (μ_h) = $(8L^3J_D)/(9\varepsilon\varepsilon_o V^2)$

Where,

L= thickness of the perovskite layer (90nm)

J_D= current density at child region

V= voltage at child region

ε= relative permittivity (~25.5)

ε_o = vacuum permittivity, Device area (A) = 0.5x0.5 mm^2

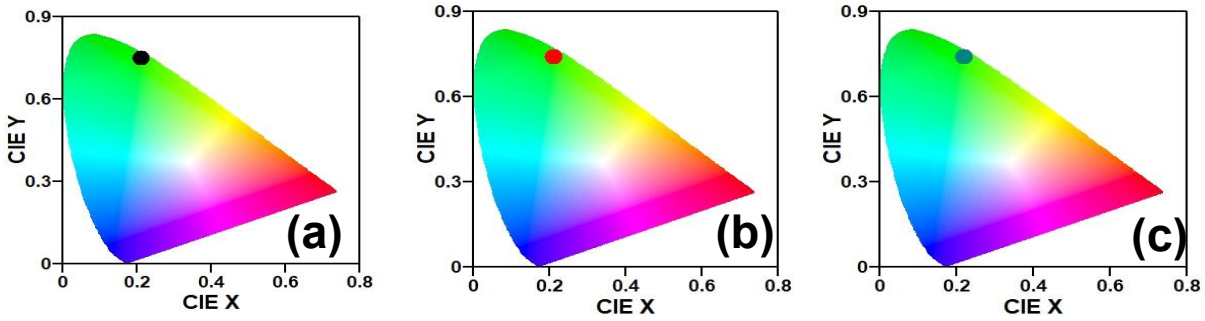

Figure A3.5: CIE coordinates for PeLEDs coated on the top of (a) PEDOT:PSS, (b) PEDOT:PSS/NPD and (c) PEDOT:PSS/PVK HTL combinations.

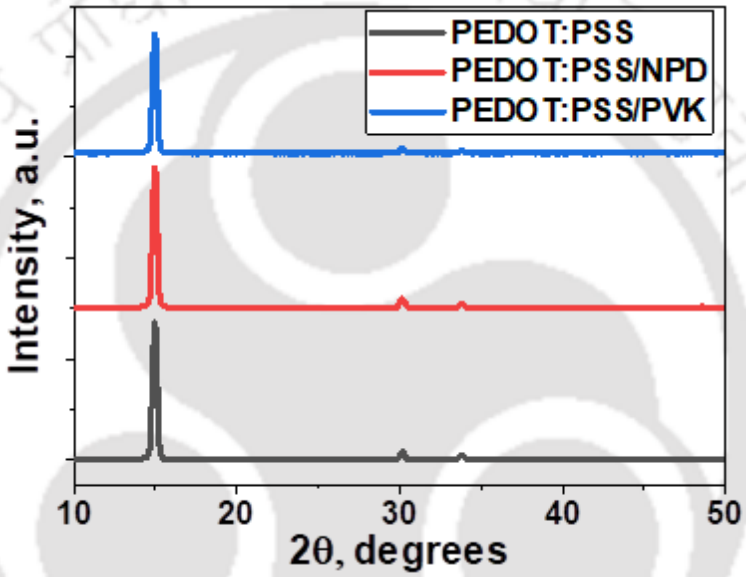

Figure A3.6: XRD patterns for perovskite films coated on different HTL combinations.

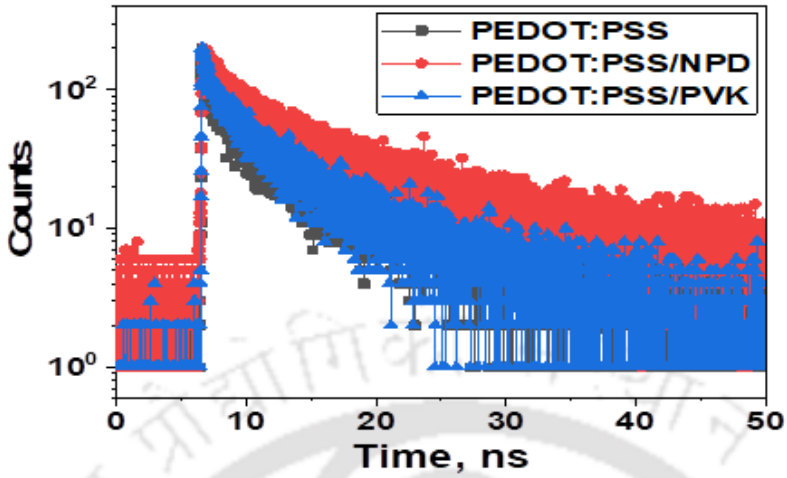

Figure A3.7: Time-resolved photoluminescence (TRPL) spectra of perovskite films coated on different HTL combinations.

Table A3.2: Summary of TRPL parameters of perovskite films with different single and double HTLs.

S.No	Type of the sample	τ_1(ns)	τ_2(ns)	τ_{avg}(ns)
1	PEDOT:PSS/$MAPbBr_3$	2.57	43.20	32.18
2	PEDOT:PSS /NPD/$MAPbBr_3$	4.27	49.55	45.78
3	PEDOT:PSS /PVK/$MAPbBr_3$	2.64	47.11	35.69

[This page was intentionally left blank]

Chapter 4

Conjugated polymer-based electrical Ammonia sensor with Schottky barrier diode modelling

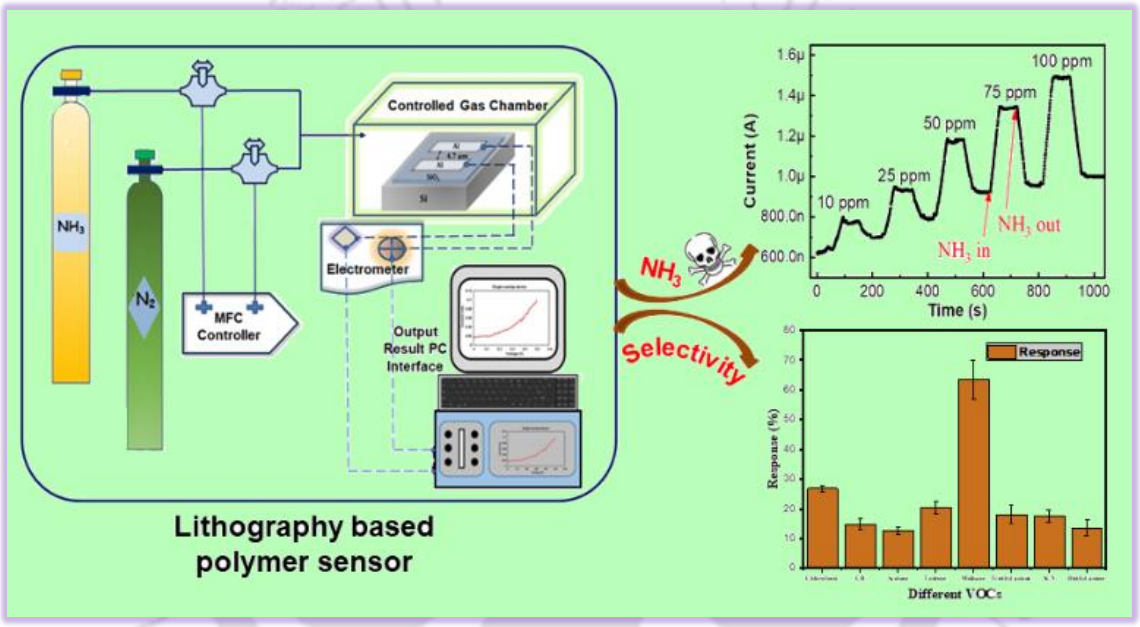

Manuscript: Ramesh Babu Yathirajula, Arvin Sain Tanwar, Himangshu Baishya, Vimal Kumar Singh Yadav and Parameswar Krishnan Iyer, "Conjugated polymer-based highly sensitive Ammonia electrical sensor fabricated using lithography and its Schottky barrier diode modeling" (Manuscript under Communication)

[This page was intentionally left blank]

Abstract

Organic semiconductors can significantly increase the performance of photolithography-based electrical sensing devices. In this work, we develop a novel poly(3,3'-((2-(benzo[c][1,2,5]thiadiazol-4-yl)-9H-fluorene-9,9-diyl)bis(hexane-6,1-diyl))bis(1-methyl-1H-imidazol-3-ium)) (PFIM) polymer-based two-terminal electrical device for Ammonia detection. The gas sensing device is fabricated on a silicon wafer using the photo-lithography technique, with a 4.7 μm long micro-channel separating the two Aluminum electrodes. The active material PFIM is drop-cast onto the micro-channel connecting the two electrodes; The PFIM-based sensor is highly selective and effectively distinguishes Ammonia from a pool of VOCs. With a response of 64.5% and a LOD of 87.3 ppb, the PFIM shows the best response with Ammonia. The stability of the sensor is analyzed under varying humidity conditions. The calculation of the Zeta Potential is conducted with and without Ammonia. A thermionic-emission-based transport model has been utilized to extract the important parameters of the photo-lithographically fabricated Schottky barrier diode. The diode shows a barrier height of 0.52 eV, an ideality factor of 1.92, and a series resistance of 75.6 kΩ at ambient temperature.

4.1 Overview

Ammonia (NH_3) stands as a colorless and odorous compound with vital roles across diverse fields such as agriculture, automotive, chemicals, food processing, hydrogen utilization, and biomedical applications.[1, 2] Its ability to transition seamlessly between solid, liquid, and gaseous phases, owing to strong intermolecular hydrogen bonding, has contributed to its prominence. Notably, its low boiling point of -33.3 °C and melting point of -77.7 °C, coupled with a low density of 0.86 kg/m³, refractive index of 1.33, and dipole moment of 1.42 D, underscore its distinctive properties.[3] In recent times, escalating environmental pollution stemming from toxic gases like NH_3, Nitrogen dioxide (NO_2), Carbon monoxide (CO), and Sulphur dioxide (SO_2) has disrupted ecological equilibrium.[4-7] NH_3, for instance, stands as the second-highest produced chemical commodity, with a production of 235 million tons in 2019. Projections estimate a surge to approximately 290 million tons by 2030.[8] Its primary source is the agricultural sector, attributed to widespread fertilizer use, livestock farming, and suboptimal nitrogen utilization efficiency. Airborne NH_3 is closely linked to spatial and temporal variations in particulate matter (PM 2.5) concentrations, posing threats to public health upon inhalation, particularly during the COVID-19 pandemic.[9, 10] Notably, it has been identified in exhaled human breath and serves as a critical biomarker for diagnosing conditions like gastric ulcers, renal disorders stemming from Helicobacter pylori infections, and even COVID-19. In cases of renal failure, ammonium ions stemming from accumulated urea in the blood traverse the lung membrane, further emphasizing the compound's significance.[11] Given these multifaceted roles and concerns, real-time monitoring of trace NH_3 emissions has gained paramount importance for safeguarding lives, promoting environmental equilibrium, and advancing biomedical diagnostics.

A diverse array of techniques is employed for detecting NH_3, encompassing calorimetric, gravimetric, electrochemical, optical, chromatographic, catalytic, and resistive-based methods.[12-16] Among these, chemo-resistors have emerged as pivotal NH_3 sensing technologies, owing to their compact design, affordability, ease of use, portability, and energy efficiency. These attributes make them well-suited for NH_3 detection in contexts

ranging from human breath analysis and workplace leak monitoring to agricultural applications.

An electrical gas sensor comprises a sensing material arranged as a layer deposited onto a substrate that contains electrodes, which is then accompanied by detecting circuitry. The setup determines changes in the conductance of the sensing material upon its interaction with the targeted gas. A variety of active sensing materials have been harnessed in NH_3 gas sensing techniques.[17-21] These include polymers like polypyrrole (PPy), polyvinyl alcohol (PVA), polyaniline (PAN), poly(aniline co-pyrrole) (PAP), polystyrene (PS), poly 3,4-ethylene dioxythiophene (PEDOT), and cationic polyacrylamide (CPAM).[22-24] These polymers, chosen for their desired functionalities and conductivity, persistently advance the performance of NH_3 sensing. Polymer-based NH_3 sensors are particularly esteemed for their compact configurations, user-friendliness, ecological compatibility, tunable chemistries, cost-effectiveness, flexibility, and energy efficiency. This unification of qualities has cemented its status in various applications, encompassing scaled-down sensing arrangements, environmentally conscious detection methodologies, and versatile sensing platforms.

In this work, a two-terminal conducting polymer-based electrical sensor is fabricated for targeted detection of NH_3 gas with other Volatile Organic Compounds (VOCs). This gas sensing device is constructed on a silicon wafer platform, with two Aluminum (Al) electrodes separated by a micro-channel measuring 4.7 µm in length. In the process of evaluating the selectivity of the PFIM-based device, our results indicate that it effectively differentiates ammonia from a range of VOCs. The device shows an impressive sensor response of 64.5%, with a Limit of Detection (LOD) as low as 87.3 parts per billion (ppb), making it particularly sensitive to ammonia. To further assess its operational characteristics, we also conducted experiments involving humidity variations. Employing mathematical modeling, we investigated the photolithography Schottky barrier diode, revealing remarkable electrical parameters. Specifically, the barrier height is calculated to be 0.52 eV, the ideality factor stood at 1.92, and the series resistance measured 75.6 kΩ at ambient temperature. These findings signify a substantial enhancement in the electrical performance of the two-terminal sensor. Zeta Potential studies are performed with and without ammonia exposure.

These investigations provided insights into the impact of ammonia on the device's structure and surface properties. Our study showcases the potential of organic semiconductors to elevate the capabilities of photolithography-based electronic sensing devices. The PFIM polymer-based two-terminal electrical device exhibited outstanding selectivity for ammonia detection, displaying a remarkable response rate and an impressively low LOD. Additionally, coupled with mathematical modeling, this chapter details the advancements achieved in enhancing the sensor's overall performance.

4.2 Experimental Section

4.2.1 Materials

All chemicals, as well as reagents, and Aluminum, were purchased from Sigma Aldrich, Merck (India), and Alfa-Aesar. Elix-grade water from a Milli-Q purification system was used for the experiments.

4.2.2 Synthesis of PFIM

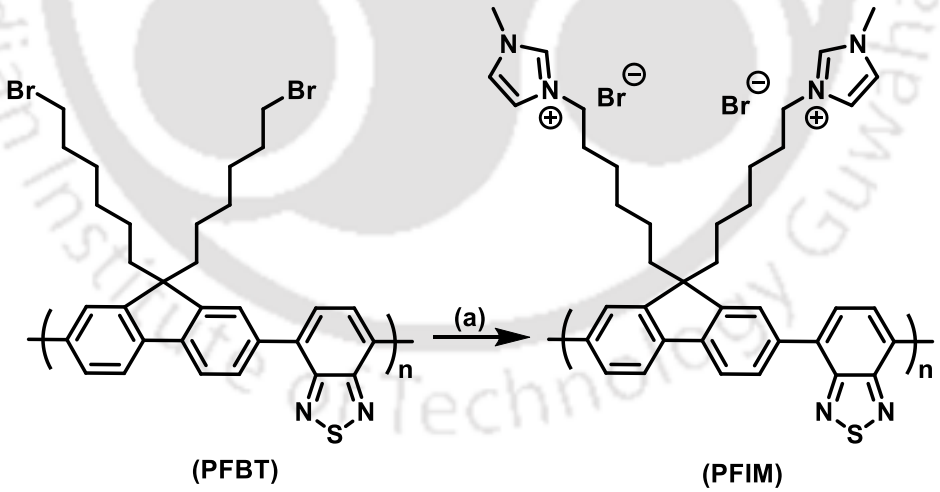

Figure 4.1: Synthesis of PFIM: (a) 1-Methylimidazole, DMF, 70 °C, 24 h. (Scheme)

Synthesis of PFIM: In a 10 mL round bottom flask, the precursor polymer PFBT (21 mg), was solubilized in dimethylformamide (2 mL) and then added 1-Methylimidazole (0.5 mL).[25]

The reaction mixture was stirred for 24 h at 70 °C in an inert nitrogen gas atmosphere. Later it was cooled to room temperature and poured into diethyl ether to get precipitates. The precipitates were collected and washed multiple times with dichloromethane (DCM) followed by drying at room temperature to get an orange-colored polymer (PFIM) **(Figure 4.1)** (Yield = 82%). ^{1}H NMR (600 MHz, δ, DMSO-d6): 9.09 (b), 8.23 (b), 8.15 (b), 7.68 (b), 7.66 (b), 4.05 (b), 3.80 (b), 2.18 (b), 1.63 (b), 1.14 (b), 1.07 (b), 0.80 (b). (**Figure A4.1**)

4.2.3 Device Fabrication with Photolithography

The Si/SiO_2 substrate underwent initial cleaning with Piranha solution, followed by sequential rinsing with Deionized (DI) water, Acetone, and 2-propanol. The substrate was then dried well in the presence of Nitrogen gas (N_2). A primer Hexamethyldisilazane (HMDS) was used for spin-coating the cleaned substrate and was annealed at 125 °C for 10 minutes. Soon afterward, S1813 (a positive photoresist) was spin-coated and soft-baked at 125 °C for 3 minutes (**Figure A4.2**).

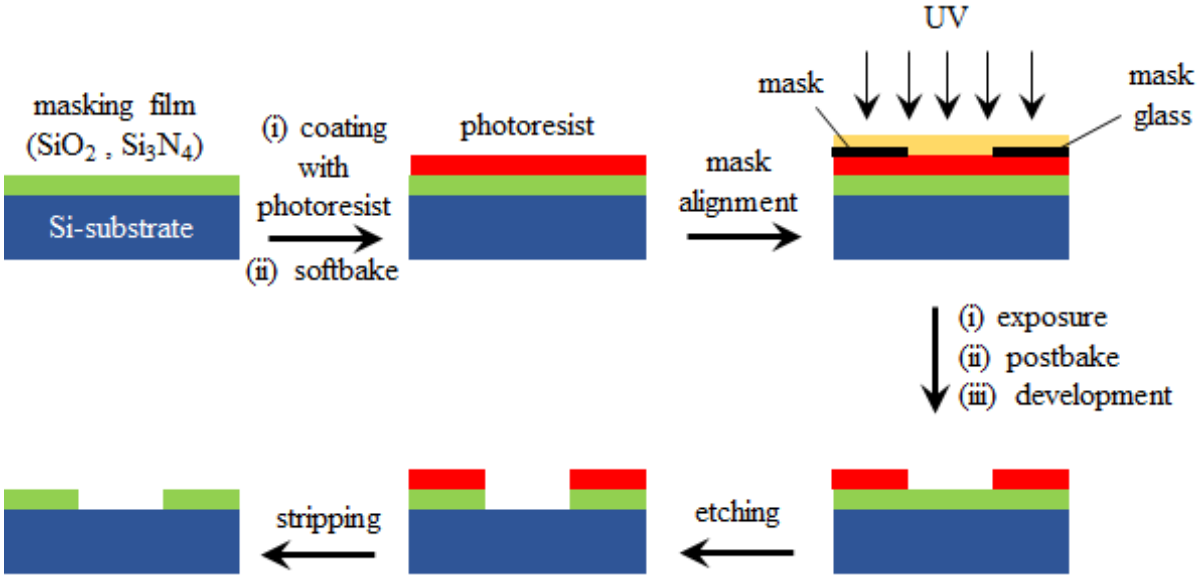

Figure 4.2: Photolithography Process Steps (PR: S1813, 1µm thick, 3000 rpm, Acetone cleaning).

Next, a two-terminal electrode with a length of 5 µm and a width of 10 µm was drawn using CleWin software; the substrate was patterned using direct laser beam lithography [Make: KLOE, Model-Dilase-250] by maintaining the appropriate velocity and modulation.

After that, the substrate was dipped into a developer solution for 1 minute and hard-baked at 125 °C. Finally, 100 nm thick Aluminum was deposited over the patterned substrate using a thermal evaporation system [Make: HHV Auto 500]. **(Figure 4.2)** For the lift-off process, the deposited Aluminum substrate was immersed in acetone, followed by washing with DI water.

PFIM polymer-based gas-sensing device was fabricated by using a simple drop-casting method and optical images were recorded. (**Figure A4.3**) At first, 2 µL of the sensing material was dropped cast over electrodes and annealed at 100 °C for 10 min; this process was repeated twice to reinforce the material uniformly between the electrodes. The drop-cast material had a diameter of approximately 2–3 mm over the electrodes and an average thickness of 150 nm.

4.2.4 Characterization

In the electrical characterization, the fabricated sensor was placed inside a controlled environment chamber (CEC, Gen Renew India), and the contact pads were connected to a source meter by using low-noise triaxial cables (Keithley 4200A-SCS, USA.) via crocodile clips. The CEC system consists of three mass flow controllers (MFCs) [Make: Alicat Scientific] with different flow rates to control the carrier and analyte gas. Alicat's Flow Vision MX gas-blending software in the computer regulated the gas mixing as per the required percentage and pressure. (**Figure A4.4**) The MFC output was connected to the sensing chamber through an in-line mixing unit. ^{1}H NMR (600 MHz) and ^{13}C NMR (100 MHz) spectra were obtained on Bruker Ascend 600 and Varian spectrometers, respectively. Malvern Zetasizer Nano ZS90 Model No. ZEN3690 was used to calculate the zeta potential of the polymer.

4.3 Results and Discussions

Sensing and Selectivity Studies:

Sensing experiments were conducted using two-terminal sensor devices featuring PFIM polymer with a simple architecture, as illustrated in **Figure 4.3(a)**. The devices were placed within a controlled environmental chamber (CEC) and connected to a Keithley 4200A SCS semiconductor parameter analyzer for comprehensive electrical characterization. For I–

V (Current-Voltage) measurements, initial tests were performed in a vacuum, followed by subsequent measurements under ambient conditions. The voltage was swept from -10 V to +10 V to assess the devices' stability in real-world environments.

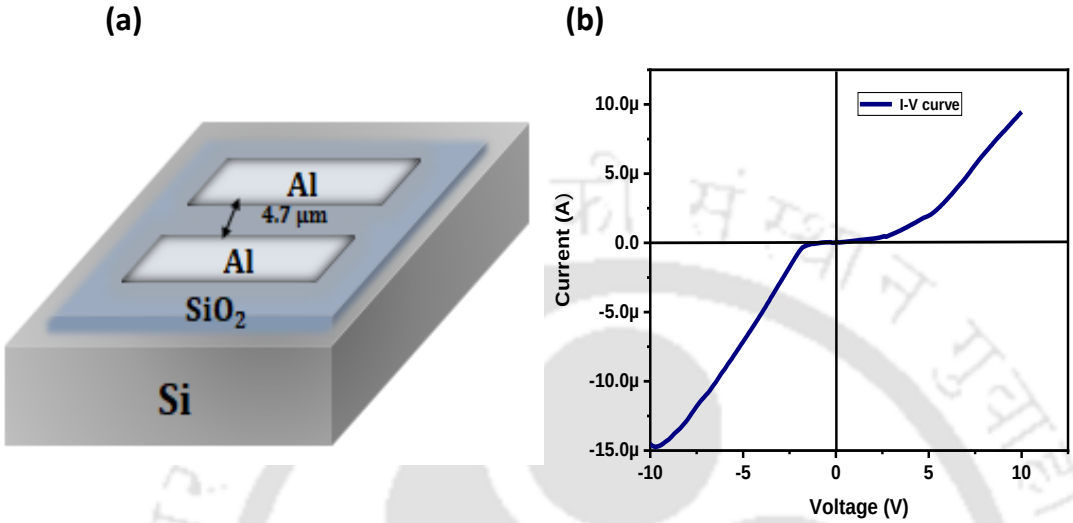

Figure 4.3: (a) Schematic diagram of the device structure and (b) I–V characteristics of the PFIM thin film device.

The I–V curve acquired for a thin film fabricated with PFIM showcased favorable conducting behavior, as shown in **Figure 4.3 (b)**. To investigate the sensing response of a PFIM film-based device towards NH_3, the concentrations of NH_3 were systematically varied from 10 ppm to 100 ppm and changes in the current intensity were observed.

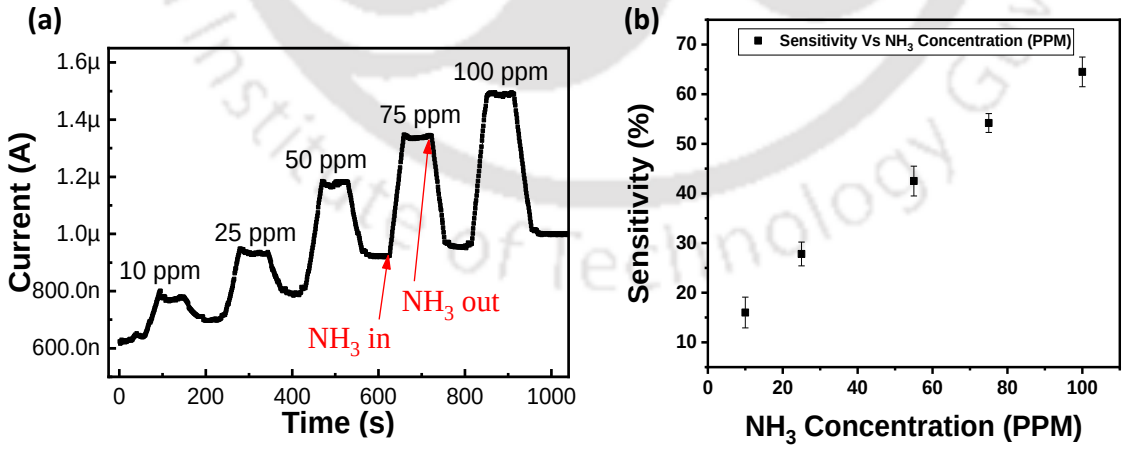

Figure 4.4: (a) Response of the PFIM sensor device towards various concentrations of NH_3 vapors ranging from 10 ppm to 100 ppm and (b) sensitivity of a device as a function of NH_3 concentration.

As shown in **Figure 4.4 (a),** a significant increase in current was observed upon the introduction of 100 ppm NH_3 vapors into the CEC, demonstrating a continuous enhancement with a remarkably short response time. When the NH_3 source was turned off, the current intensity quickly returned to its initial level. This observation leads to the conclusion that the device exhibits commendable response and recovery times for NH_3 detection. For the quantification process, the chamber underwent exposure to NH_3 vapors at concentrations of 10, 25, 50, 75, and 100 ppm. This exposure resulted in similar responses characterized by higher current intensities that corresponded to the varying concentrations of NH_3. The corresponding sensitivity (S) was calculated using the formula $S = \Delta I/I_0$, where ΔI is the change in current intensity upon NH_3 vapor exposure and I_0 is the initial current in the absence of NH_3 vapors. The sensitivity of the device was then plotted as a function of different NH_3 concentrations. The curve showed a linear response with an increase in the concentration of ammonia as shown in **Figure: 4.4 (b)**.

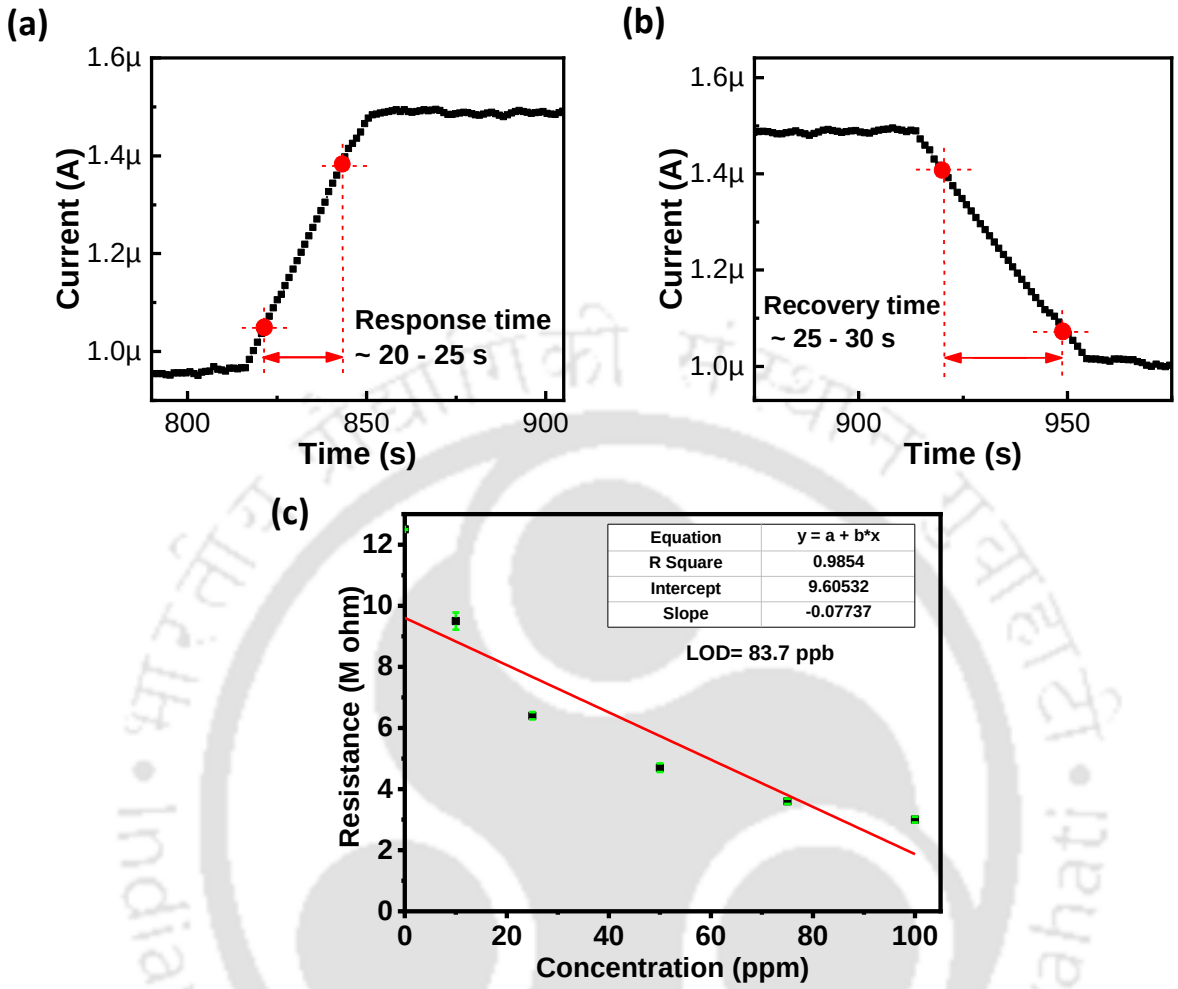

Figure 4.5: (a-b) Response and recovery time of the NH_3 sensor and (c) calibration curve for calculating the detection limit.

The valuation of response and recovery times stands as crucial parameters for any gas-sensing devices. The response time is defined as the duration required for a sensing device to achieve 90% of the total current change following the introduction of analyte vapors. Whereas, the recovery time is the duration for the device to return 90% of the current change to its original position after deactivating the analyte vapor source. In the case of the device's response to 100 ppm of NH_3, the calculated response time was remarkably low at 25 s, while the recovery time was found to be 30 s. These quick response and recovery times underscore the efficiency of the device in rapidly detecting and recovering from the presence of NH_3 vapors (**Figure: 4.5 (a-b)**). To the best of our knowledge, such low-cost stability devices

have not been reported yet with such a remarkable response/recovery time for NH_3 detection and high sensitivity making the current protocol highly reliable and useful for the rapid detection of NH_3 vapors. The LOD is another vital parameter to be determined for a sensor device. To calculate the LOD, a calibration curve was constructed by plotting the maximum current intensity against the concentration of NH_3 (**Figure: 4.5 (c**)).

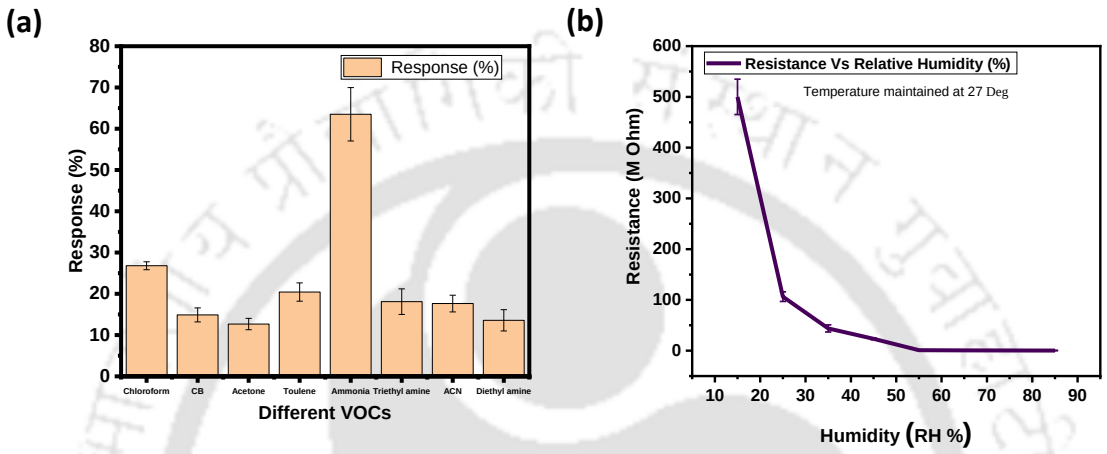

Figure 4.6: (a) Selectivity studies and (b) Humidity studies

The curve demonstrates a good linear relationship with the correlation coefficient (R^2) value of 0.9854. To assess the sensor's sensitivity, the LOD was calculated using the formula LOD = 3 × |σ| / slope, where 'σ' represents the average of the standard deviation of the baseline readings, and 'slope' corresponds to the slope of the average electrical resistance with varying concentrations of ammonia. This LOD calculation method allows for a quantitative evaluation of the sensor's ability to detect low concentrations of ammonia. Applying this approach, the sensor demonstrated a calculated LOD of 87.3 ppb for ammonia detection. This LOD value underscores the sensor's capability to reliably identify trace amounts of ammonia in the tested environment. To validate the selectivity of the device, similar sensing experiments were also performed with five common volatile organic solvents (chloroform, chlorobenzene, acetone, toluene, and ACN). The device responses to common organic analytes were very low in comparison to 100 ppm of NH_3. To date, such outstanding selectivity and reusability of NH_3 sensors with remarkably low detection limits have marked this sensor device as a rare example available in the literature. To further explore the selectivity of this system, the device was also exposed to various other common organic

amines such as triethyl amine and diethyl amine, etc., since all these vapors have biological or environmental consequences. From (**Figure: 4.6** (**a**)), it can be concluded safely that the response of a sensor device towards various other amines also was insignificant compared to NH_3 even at much higher concentrations.

Humidity Studies:

All sensing experiments were conducted in the laboratory atmosphere, ensuring a relative humidity (RH) of ≥ 60% that provides an environment closer to the ultimate condition of the sensor devices. To investigate deeper into the impact of humidity on the NH_3 response, additional sensing experiments were performed. These experiments involved exposing 50 ppm NH_3 to three different devices under varied humidity levels: RH 0%, 60%, and 85%, respectively. This systematic investigation allows for a comprehensive understanding of how humidity influences the sensor's performance in NH_3 detection. (**Figure: 4.6** (**b**)). In a vacuum environment (RH 0%), the sensor device exhibited the highest response to NH_3, which decreased by ~ 21% upon increasing the relative humidity (RH) to 60%. Remarkably, with a further increase in humidity levels from 60% to 85%, the device's response to NH_3 experienced a comparatively smaller decrease of ~ 13%. The reduced sensitivity of the device at raised humidity levels supports the concept of weak adsorption/diffusion of ammonia vapors on the film's surface. This observation suggests that under higher humidity conditions, a remarkable competition arises between water and ammonia molecules for adsorption/diffusion at the receptor sites of the PFIM film. Consequently, it can be inferred that the sensor device remains operational across a wide range of humidity levels, demonstrating its potential for effective NH_3 sensing in real environmental conditions.

Sensing mechanism: Generally, the mechanism underlying organic semiconductor-based conductometric gas sensors encompasses the adsorption of analytes (NH_3) onto the surface through dissociation and/or diffusion processes. This is followed by the potential formation of a charge transfer complex, ultimately resulting in a modulation of the majority charge carriers within the current.[26, 27]Depending on the chemical nature of both species, the binding can vary in strength, ranging from weak to strong, facilitated by chemical interactions such as hydrogen bonding (hydrogen bond donor-hydrogen bond acceptor) and dipole-dipole

interactions, among others. The molecular self-assembly, due to π-π interactions in these semiconductors, additionally furnishes efficient pathways for charge migration or transport. Another significant factor influencing the mobility of charge carriers is the alteration in redox potential.[28-33]This can be explained by donor-acceptor-like complexation[34] between n-type organic semiconductor materials i.e. PFIM (electron acceptor) and NH_3 (electron donor) molecules. Since, each PFIM molecule consists of two –COOH units at the imide positions that tend to bind with analyte NH_3 through an acid-base interaction, numerous ion pairs are expected to form in the film that can drastically increase the ionic conductivity and consequently the current. In addition, the presence of imidazole groups will further boost the sensitivity of the device due to the favorable hydrogen bond interactions with NH_3. The aggregation of PFIM molecules due to π-π interactions is another possible factor responsible for such a high sensitivity since it can provide efficient charge transport into the material.

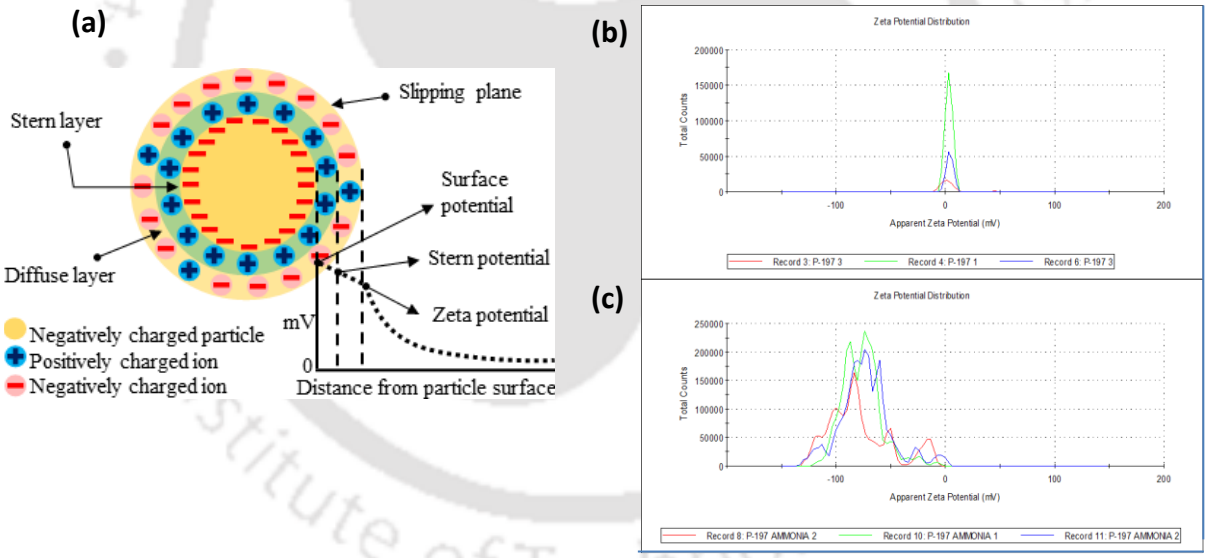

Figure 4.7: (a) Zeta Potential illustration of PFIM polymer before and after the addition of ammonia and (b-c) Zeta-Potential experiment results for only polymer and with ammonia as an analytic VOC.

Furthermore, from the zeta potential experiment, **Figure: 4.7 (a)** shows, an illustration diagram of PFIM polymer before and after the addition of ammonia with all layers involved in the zeta potential principle. Zeta potential is the electric potential at the shear plane around

a charged particle in a dispersion medium. The shear plane is a hypothetical boundary that separates the liquid phase from the stern layer, which is the region of immobilized counter ions. The zeta potential is influenced by the nature and concentration of ions in the dispersing medium and the surface charge of the particles. This significant modification strongly substantiates our hypothesis regarding the electrical characteristics of the system. **Figure: 4.7 (b-c)** shows, the zeta potential of the polymer alone measures approximately +1.91 mV, attributed to the cationic nature of PFIM. However, upon the introduction of ammonia, a significant shift occurs, and the zeta potential records at -76.5 mV. The introduction of ammonia is accompanied by a significant increase in current, further confirming the growing nature of the system's characteristics.

Mathematical modeling:

The I-V Characteristics of the fabricated devices exhibit a back-to-back Schottky diode-like behavior.

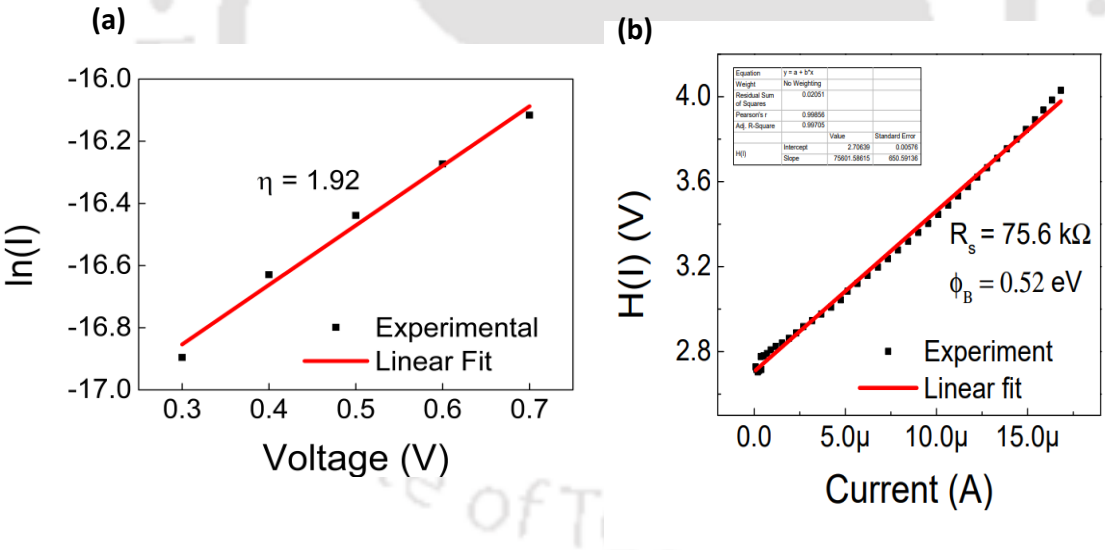

Figure 4.8: (a) Plot for ideality factor extraction and (b) Plot for SBH and R_S extraction.

The thermionic emission–based diode current model has been used to verify the experimental results as expressed below:

$$I_{SD} = SA^* T^2 e^{\frac{-q\Phi_B}{kT}} \left[e^{\frac{-qV}{\eta kT}} - 1 \right]$$-------equation (1)

The ideality factor, η of the diode is obtained as 1.92 from the ln (I)-V plot as shown in **Figure: 4.8 (a-b)**. The series resistance and SBH have been extracted with the help of ideality factor using function H(I) re-derived from equation (1) depending on the current of the diode, which is expressed as:

$$H(I) = V - \frac{\eta kT}{q} \ln \frac{I_{SD}}{SA^{*}T^{2}} = \eta \Phi_B + I_{SD} R_S \text{ -----equation (2)}$$

The value of series resistance is calculated from the slope of the straight line obtained from the H(I)-I plot, while the intercept is equal to $\eta\varphi_{SB}$. The obtained value of series resistance is 75.6 kΩ and a low SBH value of 0.52 eV.

A low SBH value hints of a strong Schottky effect, however, the ideality factor shows a larger shift from 1. The reasons are under investigation which will also help to determine the dominant transport mechanism in the fabricated sensors and to develop a better understanding of the gas and VOCs sensing mechanism.

4.4 Conclusion

In summary, we have developed a highly sensitive sensor capable of detecting minute concentrations of ammonia down to 87.3 ppb at room temperature. This accomplishment was made possible through the utilization of the PFIM polymer as sensing material. The sensor's selectivity is thoroughly assessed, demonstrating its robust performance. Our device shows a remarkable response (%) when detecting ammonia, highlighting its efficacy in this specific application. Beyond ammonia detection, we conducted comprehensive tests involving various VOCs, expanding the sensor's versatility and potential range of applications. Furthermore, this research investigated the characterization of the Schottky barrier diode parameters, revealing insightful values for the ideality factor (η=1.92), Schottky barrier height (φ_{SB}=0.52 eV), and series resistance (Rs=75.6 kΩ). These findings were obtained through mathematical modeling techniques, enhancing our understanding of the polymer diode's performance towards sensing. The derivation of key Schottky diode parameters underscores the scientific rigor of our approach. Ultimately, we present a cost-effective and exceptionally sensitive solution for ammonia sensing, showcasing the immense potential of the PFIM polymer-based sensor technology.

References

(1) A. Valera-Medina, F. Amer-Hatem, A.K. Azad, I.C. Dedoussi, M. de Joannon, R.X. Fernandes, P. Glarborg, H. Hashemi, X. He, S. Mashruk, J. McGowan, C. Mounaim-Rouselle, A. Ortiz-Prado, A. Ortiz-Valera, I. Rossetti, B. Shu, M. Yehia, H. Xiao, M. Costa, Review on ammonia as a potential fuel: From synthesis to economics, Energy Fuels 35 (2021) 6964–7029.

(2) V. Chaudhary, A. Kaur, Enhanced and selective ammonia sensing behaviour of poly(aniline co-pyrrole) nanospheres chemically oxidative polymerized at low temperature, J. Ind. Eng. Chem. 26 (2015) 143–148.

(3) Chaudhary, V.; Gautam, A.; Mishra, Y. K.; Kaushik, A. Emerging MXene-Polymer Hybrid Nanocomposites for High-Performance Ammonia Sensing and Monitoring. *Nanomaterials (Basel)* **2021**, *11* (10), 2496.

(4) S.B. Kulkarni, Y.H. Navale, S.T. Navale, F.J. Stadler, N.S. Ramgir, V.B. Patil, Hybrid polyaniline-WO3 flexible sensor: A room temperature competence towards NH3 gas, Sens. Actuators B Chem. 288 (2019) 279–288.

(5) Y. Hu, T. Li, J. Zhang, J. Guo, W. Wang, D. Zhang, High-sensitive NO2 sensor based on p-NiCo2O4/n-WO3 heterojunctions, Sens. Actuators B Chem. 352 (2022) 130912.

(6) M.A. Farea, G.B. Bhanuse, H.Y. Mohammed, M.O. Farea, M. Sallam, S.M. Shirsat, M.-L. Tsai, M.D. Shirsat, Ultrahigh sensitive and selective room-temperature carbon monoxide gas sensor based on polypyrrole/titanium dioxide nanocomposite, J. Alloys Compd. 917 (2022) 165397.

(7) Z. Zhao, C. Ma, L. Xu, Z. Yu, D. Wang, L. Jiang, X. Jiang, G. Gao, Conductive polyaniline-based microwire arrays for SO_2 gas detection, ACS Appl. Mater. Interfaces (2023).

(8) D. Gupta, A. Kafle, T.C. Nagaiah, Sustainable ammonia synthesis through electrochemical dinitrogen activation using an $Ag_2VO_2PO_4$ catalyst, Faraday Discuss. 243 (2023) 339–353.

(9) S. Comunian, D. Dongo, C. Milani, P. Palestini, Air pollution and Covid-19: The role of particulate matter in the spread and increase of Covid-19's morbidity and mortality, Int. J. Environ. Res. Public Health 17 (2020) 4487.

(10) Y. Wu, B. Gu, J.W. Erisman, S. Reis, Y. Fang, X. Lu, X. Zhang, PM2.5 pollution is substantially affected by ammonia emissions in China, Environ. Pollut. 218 (2016) 86–94.

(11) N.D. Vaziri, M. Khazaeli, A.C.F. Nunes, K.T. Harley, H. Said, O. Alipour, W.L. Lau, M.V. Pahl, Effects of end-stage renal disease and dialysis modalities on blood ammonia level: Blood ammonia in ESRD patients, Hemodial. Int. 21 (2017) 343–347.

(12) A. Bannov, J. Prášek, O. Jašek, L. Zajíčková, Investigation of pristine graphite oxide as room-temperature chemiresistive ammonia gas sensing material, Sensors (Basel) 17 (2017) 320.

(13) X. Xia, S. Guo, W. Zhao, P. Xu, H. Yu, T. Xu, X. Li, Carboxyl functionalized gold nanoparticles in situ grown on reduced graphene oxide for micro-gravimetric ammonia sensing, Sens. Actuators B Chem. 202 (2014) 846–853.

(14) P.K. Sekhar, J.S. Kysar, An electrochemical ammonia sensor on paper substrate, J. Electrochem. Soc. 164 (2017) B113–B117.

(15) M. Maierhofer, V. Rieger, T. Mayr, Optical ammonia sensors based on fluorescent aza-BODIPY dyes— a flexible toolbox, Anal. Bioanal. Chem. 412 (2020) 7559–7567.

(16) M. Zhang, X. Dong, X. Li, Y. Jiang, Y. Li, Y. Liang, Review of separation methods for the determination of ammonium/ammonia in natural water, Tren. Environ. Anal. Chem. 27 (2020) e00098.

(17) Z. Bielecki, T. Stacewicz, J. Smulko, J. Wojtas, Ammonia gas sensors: Comparison of solid-state and optical methods, Appl. Sci. (Basel) 10 (2020) 5111.

(18) D. Kwak, Y. Lei, R. Maric, Ammonia gas sensors: A comprehensive review, Talanta 204 (2019) 713–730.

(19) A.G. Bannov, M.V. Popov, A.E. Brester, P.B. Kurmashov, Recent advances in ammonia gas sensors based on carbon nanomaterials, Micromachines (Basel) 12 (2021) 186.

(20) Y. Tu, C. Kyle, H. Luo, D.-W. Zhang, A. Das, J. Briscoe, S. Dunn, M.-M. Titirici, S. Krause, Ammonia gas sensor response of a vertical zinc oxide nanorod-gold junction diode at room temperature, ACS Sens. 5 (2020) 3568–3575.

(21) Y. Seekaew, W. Pon-On, C. Wongchoosuk, Ultrahigh selective room-temperature ammonia gas sensor based on tin–titanium dioxide/reduced graphene/carbon nanotube nanocomposites by the solvothermal method, ACS Omega 4 (2019) 16916–16924.

(22) M.A. Farea, H.Y. Mohammed, S.M. Shirsat, P.W. Sayyad, N.N. Ingle, T. Al-Gahouari, M.M. Mahadik, G.A. Bodkhe, M.D. Shirsat, Hazardous gases sensors based on conducting polymer composites: Review, Chem. Phys. Lett. 776 (2021) 138703.

(23) S. Kanaparthi, S.G. Singh, Solvent-free fabrication of a room temperature ammonia gas sensor by frictional deposition of a conducting polymer on paper, Org. Electron. 68 (2019) 108–112.

(24) Zhao, L.; Zheng, Y.; Wang, K.; Lv, C.; Wei, W.; Wang, L.; Han, W. Highly Stable Cross-linked Cationic Polyacrylamide/$Ti_3C_2T_x$ MXene Nanocomposites for Flexible Ammonia-recognition Devices. *Adv. Mater. Technol.* **2020**, *5* (7), 2000248.

(25) A.S. Tanwar, R. Parui, R. Garai, M.A. Chanu, P.K. Iyer, Dual "static and dynamic" fluorescence quenching mechanisms based detection of TNT via a cationic conjugated polymer, ACS Meas. Sci. Au 2 (2022) 23–30.

(26) Y. Huang, W. Zhang, J. Wang, Z. Wei, Probing the sensory property of perylenediimide derivatives in hydrazine gas: Core-substituted aromatic group effect, ACS Appl. Mater. Interfaces 6 (2014) 9307–9313.

(27) M.-Z. Dai, Y.-L. Lin, H.-C. Lin, H.-W. Zan, K.-T. Chang, H.-F. Meng, J.-W. Liao, M.-J. Tsai, H. Cheng, Highly sensitive ammonia sensor with organic vertical nanojunctions for noninvasive detection of hepatic injury, Anal. Chem. 85 (2013) 3110–3117.

(28) Y. Huang, L. Fu, W. Zou, F. Zhang, Z. Wei, Ammonia sensory properties based on single-crystalline micro/nanostructures of perylenediimide derivatives: Core-substituted effect, J. Phys. Chem. C Nanomater. Interfaces 115 (2011) 10399–10404.

(29) W. Huang, K. Besar, R. LeCover, A.M. Rule, P.N. Breysse, H.E. Katz, Highly sensitive NH_3 detection based on organic field-effect transistors with Tris(pentafluorophenyl)borane as receptor, J. Am. Chem. Soc. 134 (2012) 14650–14653.

(30) Y. Huang, L. Fu, W. Zou, F. Zhang, Probing the effect of substituted groups on sensory properties based on single-crystalline micro/nanostructures of perylenediimide dyes, New J Chem 36 (2012) 1080.

(31) C. Li, H. Zhai, X. Liu, W. Zhang, Y. Huang, Effect of stereoisomerism of the alkyl chain on the gas sensing properties based on perylene dyes, J. Mater. Chem. C Mater. Opt. Electron. Devices 3 (2015) 2778–2782.

(32) A. Kalita, N.V.V. Subbarao, P.K. Iyer, Large-scale molecular packing and morphology-dependent high performance organic field-effect transistor by symmetrical naphthalene diimide appended with methyl cyclohexane, J. Phys. Chem. C Nanomater. Interfaces 119 (2015) 12772–12779.

(33) Y. Huang, W. Zhang, H. Zhai, C. Li, Alkylsilane-functionalized perylenediimide derivatives with differential gas sensing properties, J. Mater. Chem. C Mater. Opt. Electron. Devices 3 (2015) 466–472.

(34) P. Dutta, B. Kalita, B. Gogoi, N.S. Sarma, Development of macroporous *co*-polyesters of glyceryl methacrylate with acrylonitrile and styrene for electrical sensing of ammonia vapor, J. Phys. Chem. C Nanomater. Interfaces 119 (2015) 17260–17270.

Appendix

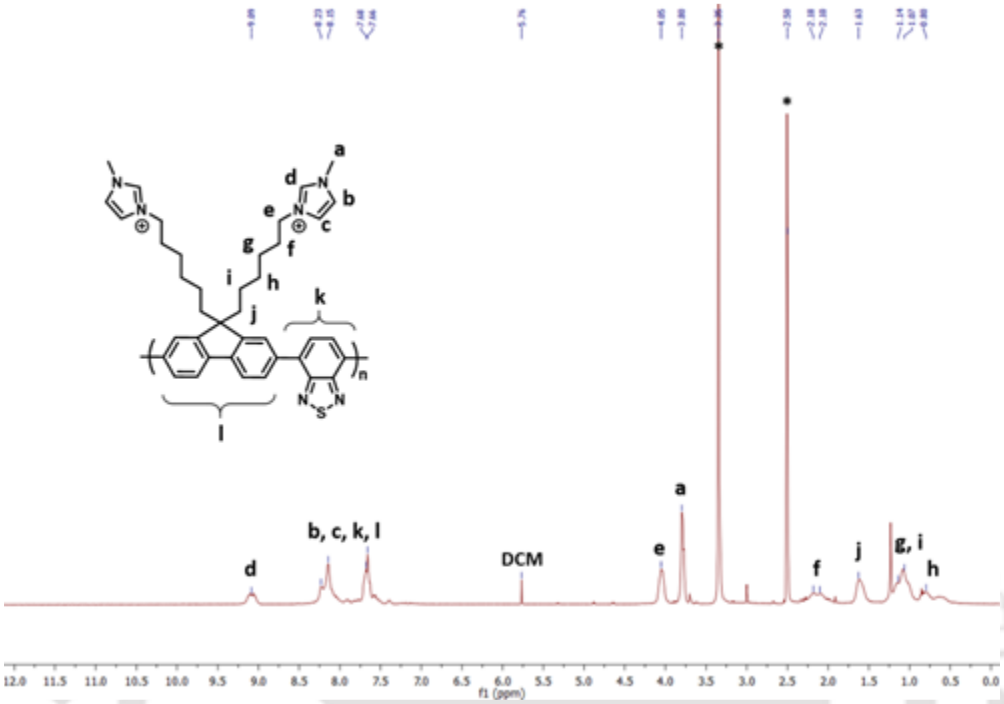

Figure A4.1: ^{1}H NMR spectra of PFIM**.**

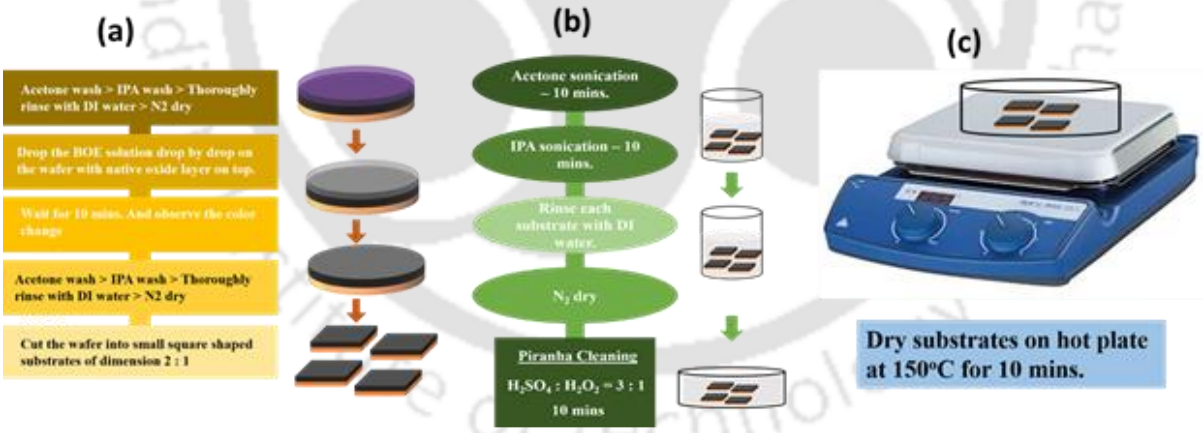

Figure A4.2 (a-c): Schematic illustration of Si/SiO2 Substrate cleaning steps.

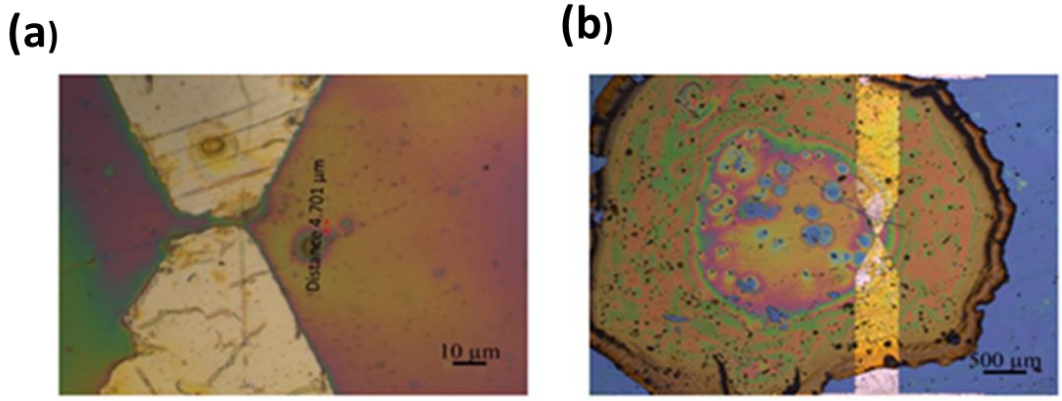

Figure A4.3: (a) Lithography-based Al channel with 4.7 µm and (b) After PFIM drop-casted on top of the microchannel. (Optical images)

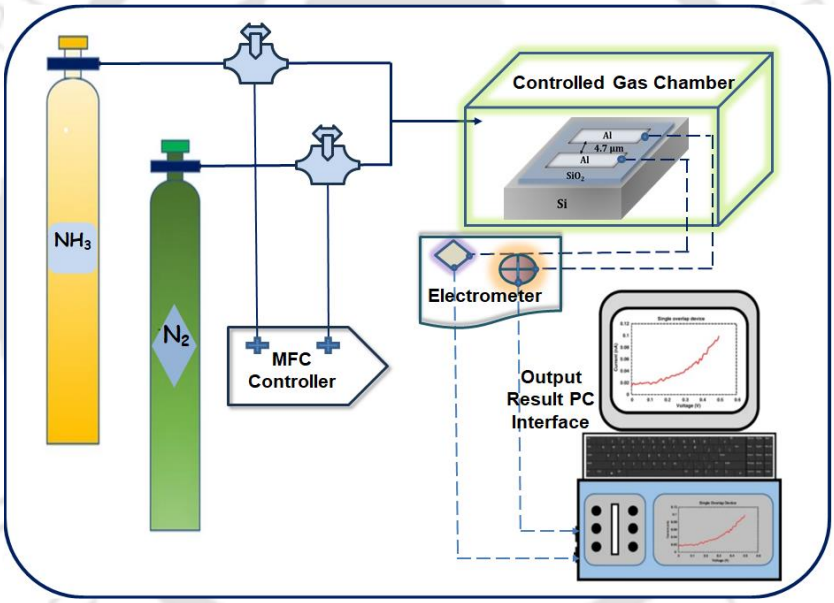

Figure A4.4: Gas /VOC sensing chamber set-up with 4200A SCS (Semiconductor Characterization System).

[This page was intentionally left blank]

Chapter 5

Printed conjugated polymer based CO electrical sensor with schottky barrier diode mathematical modelling

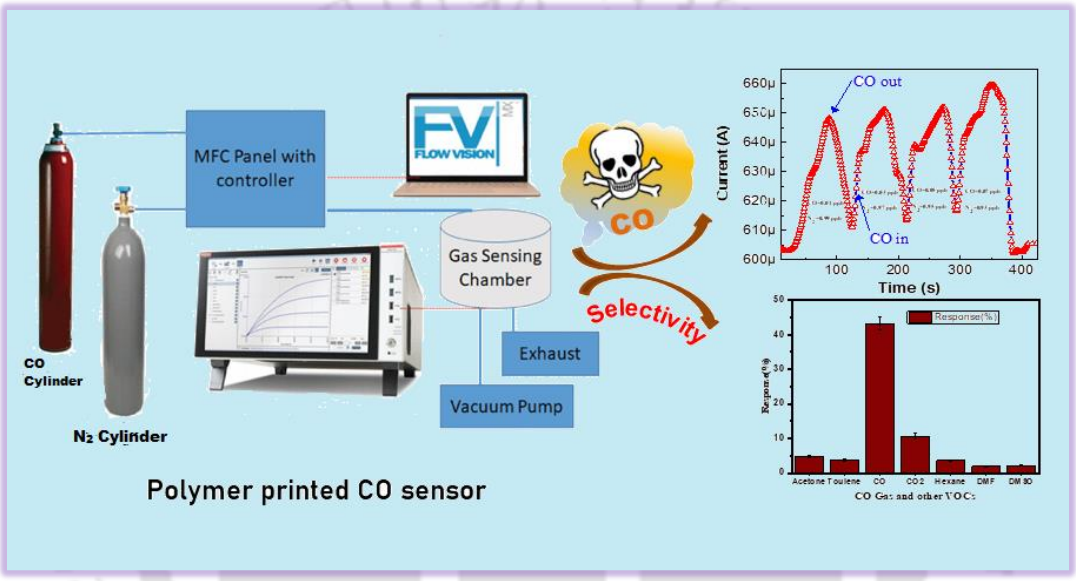

Manuscript: **Ramesh Babu Yathirajula**, Nehal Zehra, Mayur Patel, Himangshu Baishya, Vimal Kumar Singh Yadav and Parameswar Krishnan Iyer, "Printed conjugated polymer-based CO electrical sensor with schottky barrier diode mathematical modelling" (Manuscript under Communication)

[This page was intentionally left blank]

Abstract

The performance of printed electronic devices can be greatly improved by using organic semiconductors. In this study, we describe a novel Poly[(9,9-bis(4'-sulfonatobutyl)fluorene-co-alt-1,4-phenylene) sodium], (PFPT) polymer-based micro cantilever (μC) printed device for the detection of CO. The gas sensing device is fabricated on a silicon wafer support with the micro-channel of ~15 μm length separating the two μC printed AgNP electrodes. The active material PFPT is drop-casted onto the channel connecting the two electrodes. For the selectivity study, the PFPT effectively discriminates CO gas over pool of volatile organic compounds (VOCs) and CO_2 gas. With CO, the PFPT exhibits the best response of 43.25% and 0.447 ppb Limit of Detection (LOD). Furthermore, with mathematical modelling, the printed schottky diode has showed remarkable barrier height of 0.57 eV, an ideality factor of 1.7, and a series resistance of 5978 kΩ at room temperature.

5.1 Overview

The rapid pace of modernization and industrialization has led to a substantial increase in environmental pollution, making continuous environmental monitoring and pollution control imperative.[1,2,3] Among the pollutants of concern, carbon monoxide (CO) stands out as a toxic gas with a steadily rising environmental presence.[4,5] This tasteless, odorless, and colorless gas primarily originates from exhaust emissions in chemical plants, automobile exhaust, industrial processes, as well as natural sources like wildfires and volcanic activities.[6] Excessive emissions of CO pose a severe threat to the natural environment. The dangers of CO extend beyond environmental impact, as it poses a significant hazard to human health.[7] Its potent binding ability with hemoglobin, a key component of human blood, results in the impairment of oxygen transport, leading to severe tissue hypoxia in the body.[8,9] Even at low concentrations, CO can cause symptoms such as headaches, dizziness, and nausea. At higher concentrations, it can induce more severe effects such as angina, visual impairment, palpitations, and even loss of consciousness, potentially leading to fatal outcomes.[10, 11] Therefore, the detection and monitoring of this harmful gas are crucial to safeguard both living organisms and the ecosystem. Gas sensors utilizing various sensing materials have become indispensable for the detection of harmful gases. These sensors play a vital role in environmental monitoring by providing real-time data on CO concentrations. Early detection allows for timely intervention and implementation of pollution control measures, preventing adverse health effects and minimizing environmental damage.

In the past decade, significant advancements in gas sensor technologies have led to the development of various sensing materials for the detection of gaseous analytes. Among the reported classes of sensing materials, prominent ones include metal oxides, polymers, and carbon nanotubes.[12,13,14] Additionally, there is a growing trend of combining multiple classes of materials, such as metal oxide/CNT composites, polymer/graphene composites, and the exploration of less commonly used materials like metal-organic frameworks (MOFs) and ionic liquids.[15,16,17] However, polymers stand out as a particularly advantageous class of sensing materials for gas sensors, offering several key benefits over other materials. The tunable electronic and chemical properties of organic polymers, achieved by modifying the

functional groups within the material, make them highly versatile for engineering sensors with exceptional selectivity and sensitivity. This tunability allows for customization to suit specific sensing requirements, enhancing the sensor's performance in detecting targeted gases. The combination of tunable property, low manufacturing cost, and flexibility positions polymers as a highly adaptable and attractive choice for gas sensor applications.[18, 19]

In two-terminal sensing devices, the formation of a Schottky junction plays a pivotal role in the sensing mechanism, leveraging its unique electrical characteristics and surface properties. The sensitivity of the gas sensor is intricately tied to the alterations in the height and width of the barrier, resulting from the interaction of gases with the junction's surface. This sensitivity enables the detection and identification of different gases, making Schottky barrier junction-based gas sensors highly versatile. Their ability to provide selectivity, sensitivity, quick response times, low power consumption, and durability makes them well-suited for effective and consistent gas detection applications.[20, 21, 22] In summary, the unique properties of Schottky barrier junctions make them indispensable for gas sensors. Their ability to provide selectivity, sensitivity, quick response times, low power consumption, and durability makes them well-suited for effective and consistent gas detection applications.

In this work, the usage of micro-cantilever printed silver nanoparticles (AgNP) contact pads for fabrication of PFPT polymer Schottky diode-based sensors for detecting CO with the other VOCs and CO_2 with printing technology. The gas sensing device is fabricated on a silicon wafer support with the micro-channel of ~15 μm length separating the two μC printed AgNP electrodes. In the process of evaluating the selectivity of the PFPT-based device, our results indicate that it effectively differentiates CO from a range of VOCs. The device's response rate reached an impressive 43.25 %, with a LOD as low as 0.447 ppb, making it particularly sensitive to CO. To further assess its operational characteristics, we also conducted experiments involving Electro-chemical impedance spectroscopic (EIS) studies. Employing mathematical modelling, we investigated the printed schottky barrier diode, revealing remarkable electrical parameters. Specifically, the barrier height is calculated to be 0.57 eV, the ideality factor stood at 1.7, and the series resistance measured

5978 kΩ at ambient temperature. Additionally, coupled with mathematical modelling, this chapter details the advancements achieved in enhancing the sensor's overall performance.

5.2 Experimental Section

5.2.1 Materials

All chemicals, as well as reagents, and AgNP conductive (Product Id: 736481) were purchased from Sigma Aldrich, Merck (India), and Alfa-Aesar. Elix-grade water from a Milli-Q purification system was used for the experiments.

5.2.2 Synthesis of PFPT

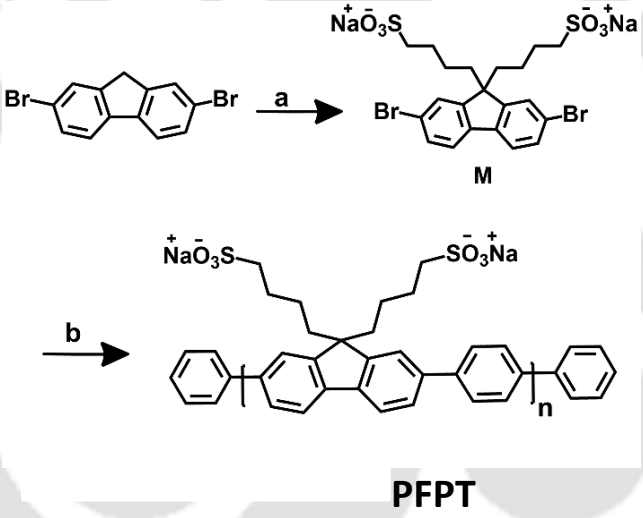

Figure 5.1: Synthesis of 2,7-Dibromo-9,9-bis(4'-sulfonatobutyl)fluorenedisodium, M

In a 50 ml round bottom flask 2,7-dibromo fluorene (0.5 g, 1.5 mmol), tetrabutyl ammonium bromide (0.08g, 0.248 mmol), 50% aqueous sodium hydroxide solution (1mL) were added and degassed twice. To this, 1,4-butane sultone (0.49g, 3.6 mmol) dissolved in 9 mL DMSO was transferred drop wise and the mixture was stirred overnight at room temperature under argon. The resulting mixture was then precipitated in acetone and crystalized in water to obtain the desired compound as a colorless crystal.

^{1}H NMR (600 MHz, D_2O, δ ppm): 7.55(s,2H), 7.55(d,2H), 7.44-7.41(d,2H), 2.45(m,4H), 1.93(m,4H), 1.33(m,4H), 0.48(m,4H). (**Figure A5.1**) ^{13}C NMR (150 MHz, D_2O, δ ppm): 152.12, 139.02, 130.32, 126.48, 121.38, 121.23, 55.25, 50.72, 38.67, 24.14, 22.31. (**Figure A5.2**)

Synthesis of Poly[(9,9-bis(4'-sulfonatobutyl)fluorene-co-alt-1,4-phenylene) sodium], PFPT: A mixture of benzene 1,4-bis boronic acid (0.052 g, 0.318 mmol), monomer M (0.2g, 0.312 mmol), aq. K_2CO_3 (2 M) and catalyst tetrakistriphenylphosphine palladium(0) (0.018g, 0.0156 mmol), were added in a round bottom flask under an inert atmosphere. The water: DMF (1:3) mixture was introduced into the flask and degassed three times via the freeze-thaw cycles. The reaction mixture was refluxed for 36 h under an inert atmosphere, followed by precipitated acetone. The precipitate was then dissolved in water and purified using a dialysis membrane (molecular cutoff 2000 g/mole) for two days. Afterward, freeze-drying was carried out to yield the desired polymer as a greyish solid (0.18g, 81.1 %). **(Figure 5.1)** ^{1}H NMR (500 MHz, DMSO-d6, δ ppm): 7.90-7.37(m, 10H), 2.19(b, 8H), 1.39(b, 4H), 0.63(b, 4H). (**Figure A5.3**)

5.2.3 Device Fabrication with Material Printing System (MPS)

The Si/SiO_2 substrate underwent initial cleaning with piranha solution, followed by sequential rinsing with deionized (DI) water, acetone, and 2-propanol. The substrate was then dried well in the presence of nitrogen gas (N_2). 1 μL of AgNP ink is drop-casted over a cleaned SiO2/Si substrate and annealed from 60°C to 200°C with a rate of 2°C/minute. The annealed AgNP drop is bisected with a sharp edge cutter to achieve a channel gap varying from 10 to 50 μm. Finally, device is fabricated on a silicon wafer support with the micro-channel of ~15 μm length separating the two μC printed AgNP electrodes. PFPT polymer based CO gas-sensing device was fabricated by using a simple drop-casting method and images are showed. (**Figure A5.4 and Figure A5.5**) At first, 2 μL of the sensing material was drop casted over electrodes and annealed at 100 °C for 10 min; this process was repeated twice to reinforce the material uniformly between the electrodes. The drop-cast material had a diameter of approximately 2–3 mm over the electrodes and an average thickness of around 100 nm.

5.2.4 Characterization

In the electrical characterization, the fabricated sensor was placed inside a controlled environment chamber (CEC, Gen Renew India), and the contact pads were connected to a source meter by using low-noise triaxial cables (Keithley 4200A-SCS, USA.) via crocodile

clips. The CEC system consists of three mass flow controllers (MFCs) [Make: Alicat Scientific] with different flow rates to control the carrier and analyte gas. Alicat's Flow Vision MX gas-blending software in the computer regulated the gas mixing as per the required percentage and pressure. (**Figure A5.6**) The MFCs output was connected to the sensing chamber through an in-line mixing unit. ^{1}H NMR (600 MHz) and ^{13}C NMR (100 MHz) spectra were obtained on Bruker Ascend 600 and Varian spectrometers, respectively. Electro-chemical impedance spectroscopic measurement were performed using an electrochemical workstation (CH Instruments 760D).

5.3 Results and Discussions

Sensing and Selectivity Studies:

Sensing experiments were carried out utilizing printed two-terminal sensor devices incorporating PFPT polymer with a straightforward architecture, as depicted in **Figure 5.2 (a)**. These devices were situated within a controlled environmental chamber (CEC) and connected to a Keithley 4200A SCS semiconductor parameter analyzer for thorough electrical characterization. Initially, I–V (Current-Voltage) measurements were conducted in a vacuum, followed by subsequent tests under ambient conditions. Voltage sweeping ranging from -5 V to +5 V was employed to evaluate the devices' stability in real-world environments.

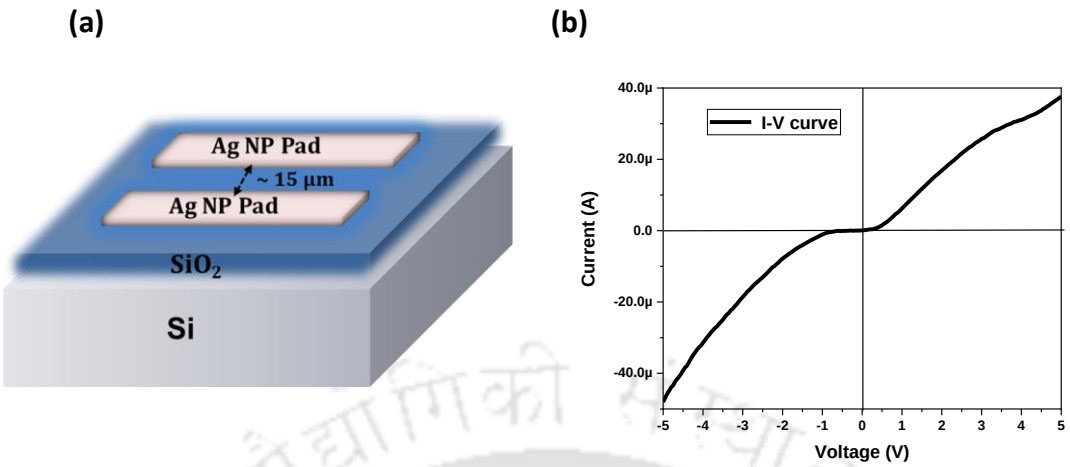

Figure 5.2: (a) Schematic diagram of the printed device structure and (b) I–V characteristics of the PFPT thin film device.

The I–V curve acquired for a thin film fabricated with PFPT showcased favorable conducting behavior, as shown in **Figure 5.2 (b)**. Subsequent optical images were captured of the printed device with a channel length of approximately 15 µm, both with and without PFPT polymer drop-casted into the channel. These images allow observation of the channel length and the formation of the two-terminal device (**Figure 5.3 (a-b)**). To explore the sensing response of a PFPT film-based device to CO gas, concentrations of CO were systematically varied from 0.01 ppb to 0.07 ppb, and alterations in the current intensity were monitored.

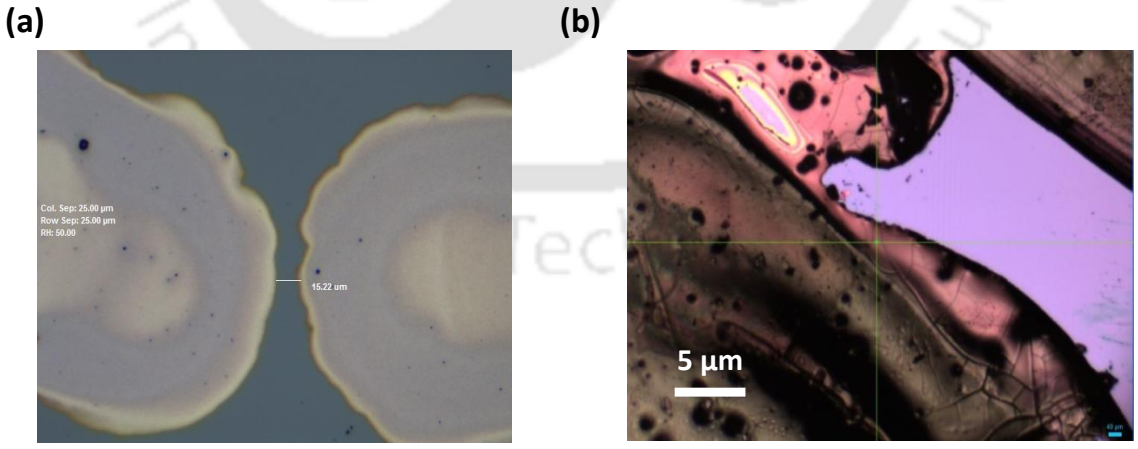

Figure 5.3: (a) Optical image of printed device with channel length ~15 µm and (b) Optical image of printed device after PFPT polymer drop-casted into the channel.

As illustrated in **Figure 5.4 (a),** a notable increase in current was noted upon the introduction of 0.01 ppb CO gas into the CEC, showcasing a continuous enhancement with an impressively short response time. Upon cessation of the CO gas source, the current intensity turned off to its initial level. This observation suggests that the device demonstrates commendable response and recovery times for CO gas detection. For quantification, the chamber underwent exposure to CO gas at concentrations of 0.01, 0.03, 0.05, and 0.07 ppb, resulting in similar responses characterized by higher current intensities corresponding to the varying concentrations of CO gas. The corresponding sensitivity (*S*) was calculated using the formula $S = \Delta I/I_0$, where ΔI is the change in current intensity upon CO gas exposure and I_0 is the initial current in the absence of CO gas.

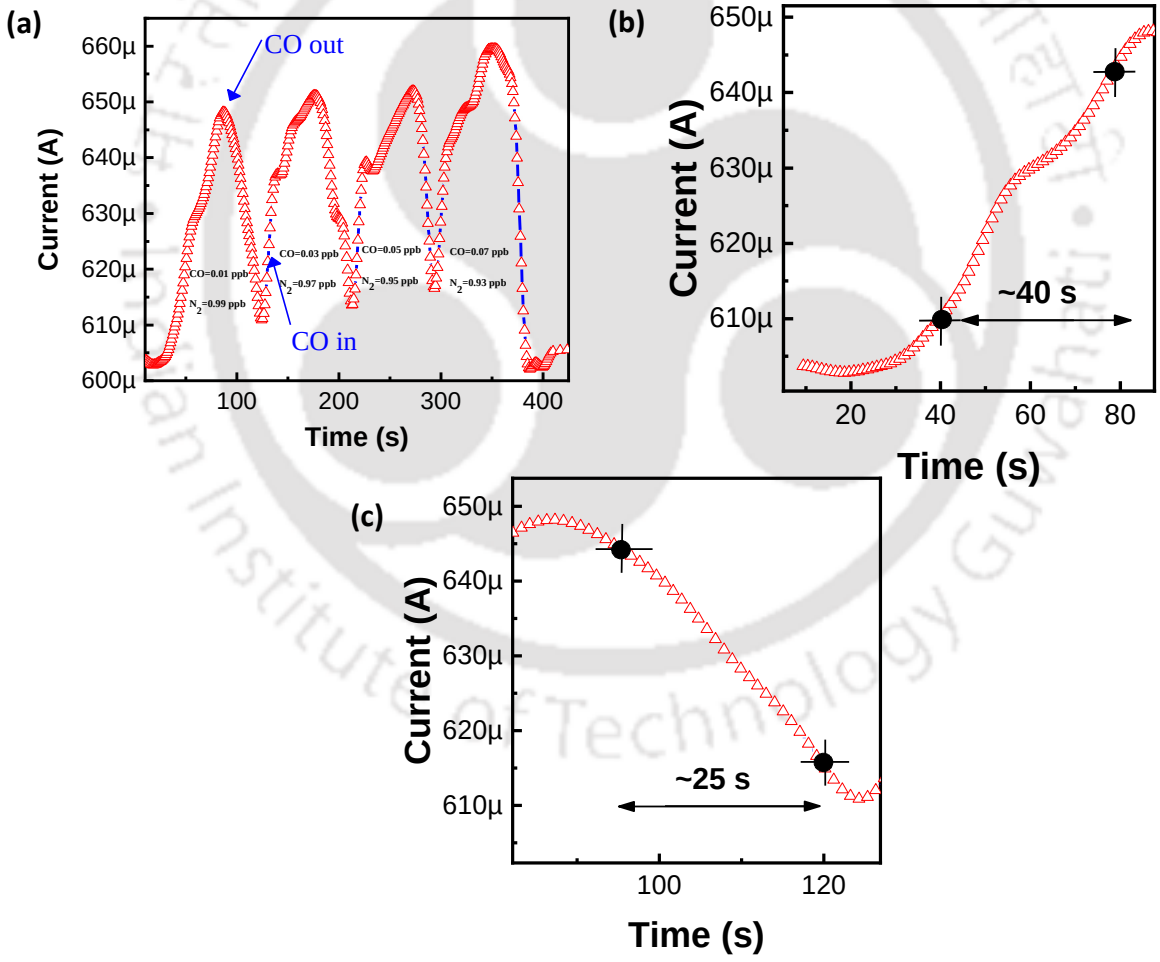

Figure 5.4: (a) Transient Response of the PFPT printed sensor device towards various concentrations of CO gas and (b-c) Response and recovery time of the CO gas sensor.

The valuation of response and recovery times stands as crucial parameters for any gas-sensing devices. The response time is defined as the duration required for a sensing device to achieve 90% of the total current change following the introduction of analyte gas. Whereas, the recovery time is the duration for the device to return 90% of the current change to its original position after deactivating the analyte gas source. In the case of the device's response to 0.07 ppb of CO gas, the calculated response time was remarkably low at 45 s, while the recovery time was found to be 25 s. These quick response and recovery times underscore the efficiency of the device in rapidly detecting and recovering from the presence of CO gas (**Figure: 5.4 (b-c)**). To the best of our knowledge, such low-cost stability devices have not been reported yet with such a remarkable response/recovery time for CO gas detection and high sensitivity making the current protocol highly reliable and useful for the rapid detection of CO gas. To validate the selectivity of the device, similar sensing experiments were also performed with five volatile organic solvents (acetone, toluene, hexane, DMF and DMSO). The device responses to common organic analytes were very low in comparison to maximum concentration of CO. To date, such outstanding selectivity and reusability of CO gas sensors with remarkably low detection limits have marked this sensor device as a rare example available in the literature. However, the device barely produces notable current responses toward VOCs, even at higher concentrations. This may be due to the difference in magnitude of electronic doping or redox exchange between the p-type semiconductor and analyte exposed, which in turn depends on the electron-donating or accepting ability of analyte gas. To further explore the selectivity of this system, the device was also exposed to CO gas since this gas has environmental consequences from **Figure: 5.5 (a**)

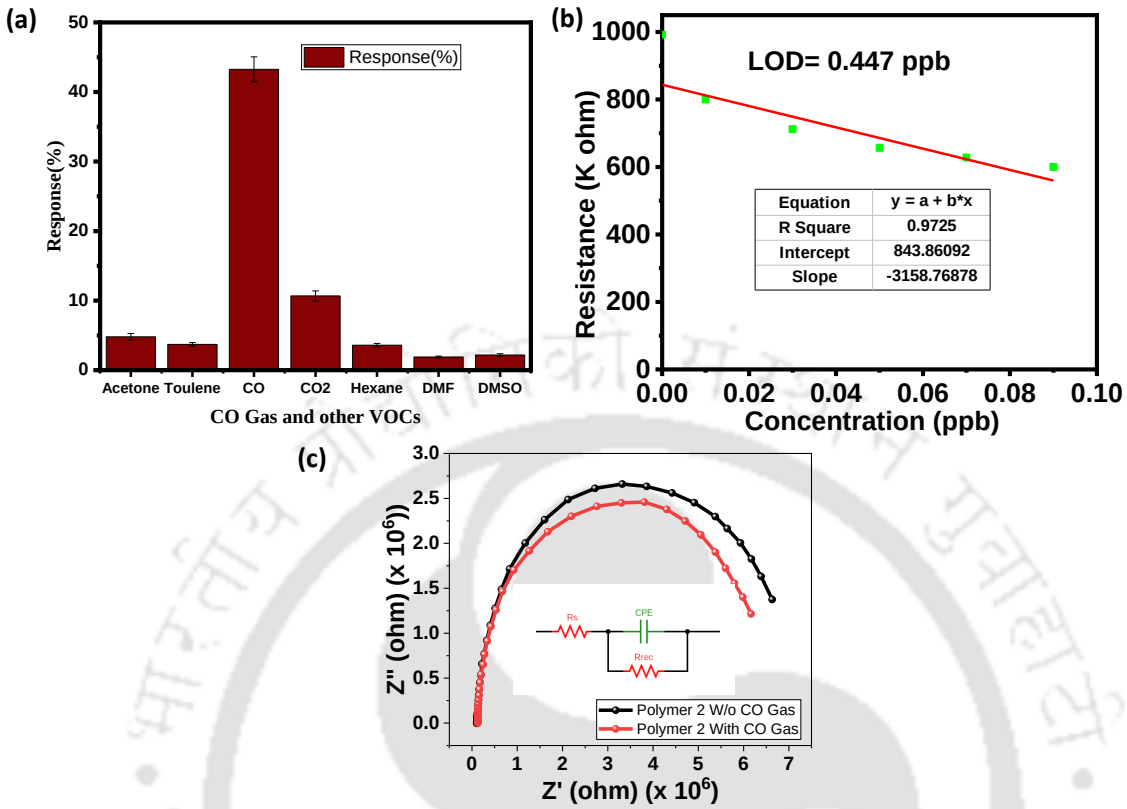

Figure 5.5: (a) Selectivity studies with CO_2 and other VOCs (b) calibration curve for calculating the detection limit and (c) Electro-chemical impedance spectroscopic (EIS) studies with and without CO gas.

The LOD is another vital parameter to be determined for a sensor device. To calculate the LOD, a calibration curve was constructed by plotting the maximum current intensity against the concentration of CO gas (**Figure: 5.5 (b)**). The curve demonstrates a good linear relationship with the correlation coefficient (R^2) value of 0.9725. To assess the sensor's sensitivity, the LOD was calculated using the formula LOD = 3 × |σ| / slope, where 'σ' represents the average of the standard deviation of the baseline readings, and 'slope' corresponds to the slope of the average electrical resistance with varying concentrations of CO gas. This LOD calculation method allows for a quantitative evaluation of the sensor's ability to detect low concentrations of CO gas. Applying this approach, the sensor demonstrated a calculated LOD of 0.447 ppb for CO gas detection. This LOD value underscores the sensor's capability to reliably identify trace amounts of CO gas in the tested

environment. From **Figure: 5.5 (c)**, EIS study performed with and without analyte gas (CO). This study is a powerful technique used to analyze the electrical properties of materials and systems. This method involves applying a small alternating current to a system across a range of frequencies and measuring the resulting impedance. In this study, observed the reduction in impedance after exposure of CO analyte gas. This is strongly supporting to the transient response and other electrical studies. EIS study is provided valuable information about various electrochemical processes, including charge transfer resistance (R_{rec}), double-layer capacitance (C_{PE}), and solution resistance (R_s).The R_{rec}, reflects the resistance encountered by charge carriers (electrons or ions) as they transfer across the interface between the sensing material and the gas environment. A higher R_{rec} typically indicates slower charge transfer kinetics, which can result from factors such as insufficient surface reaction sites, adsorption barriers, or slow reaction kinetics with the target gas. Conversely, a lower R_{rec} (2.47 M Ω) suggests faster charge transfer and more efficient gas sensing performance. The $C_{PE,}$ represents the capacitance of the electrical double layer formed at the interface between the sensing material and the gas environment. It arises from the accumulation of charges at the electrode-electrolyte interface. Changes in C_{PE} can be indicative of alterations in the surface area, morphology, or composition of the sensing material, as well as variations in the dielectric properties of the gas environment. Typically, an increase in C_{PE} may suggest enhanced surface area or increased adsorption of gas molecules, while a decrease (18.35 pF) may indicate changes in the interfacial properties or the depletion of active sites. The R_s (7756 Ω) refers to the resistance encountered by the electrical current as it passes through the electrolyte or solution in contact with the sensing material. This resistance is influenced by factors such as the conductivity and thickness of the electrolyte layer, as well as the presence of any contaminants or impurities. All the typical values are as shown in the **Table 5.1**.

Table 5.1: Equivalent Circuit Fitting Values Obtained for with and without CO gas.

Element	Without CO gas	With CO gas
R_s (Ω)	7892	7756
C_{PE} (pF)	22.14	18.35
R_{rec} (MΩ)	8.65	2.47

Sensing mechanism: Generally, the electrical properties of semiconducting polymers are dramatically sensitive to molecular-level perturbations such as adsorption, charge transfer complexation or electronic doping, and conformational change target gas exposure. Such physical or chemically induced changes in semiconductor polymer can ultimately modulate the charge carrier density or bulk mobility of charge carrier, which could be reflected as multiple order changes in conductivity or current response of semiconducting polymer fabricated device. As in this case, the PFPT fabricated two terminal device showed significant enhancement in current intensity after introducing the CO gas. This could be accounted to the electron transfer process between p-type semiconductor PFPT and electronically deficient CO molecule resulting in the carrier density and, subsequently, the current output of the device.

Mathematical modeling:

The measured I-V Characteristics of the fabricated devices show, a back-to-back Schottky behavior.

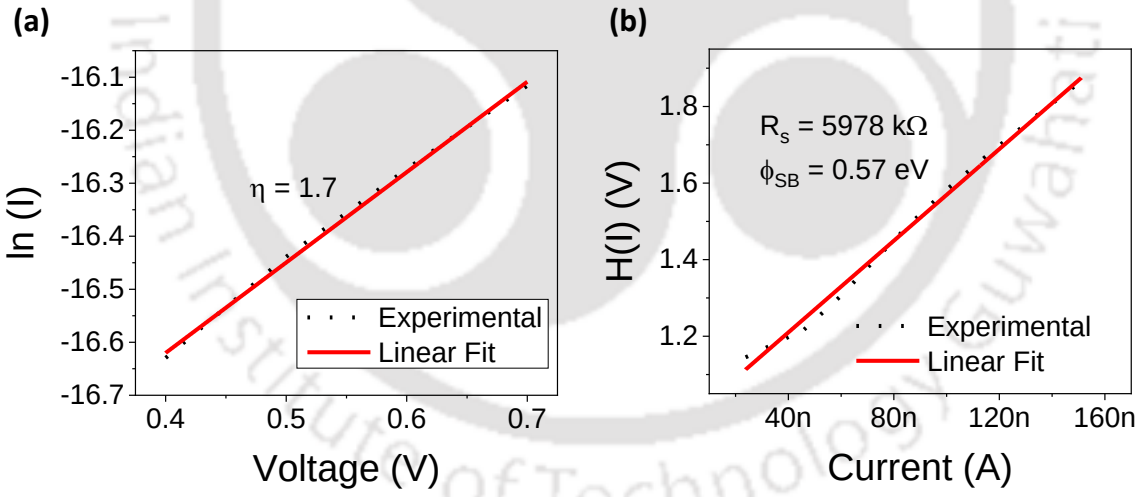

Figure 5.6: (a) Plot for ideality factor extraction and (b) Plot for SBH and R_S extraction.

The thermionic emission–based diode current model has been used to verify the experimental results as expressed below:

$$I_{SD} = SA^* T^2 e^{\frac{-q\Phi_B}{kT}} \left[e^{\frac{-qV}{\eta kT}} - 1 \right]$$-------equation (1)

The ideality factor, η of the diode is obtained as 1.7 from the ln (I)-V plot as shown in **Figure: 5.6 (a-b)**. A high ideality factor value of 1.7 suggests that the diode's series resistance may be elevated, which consequently leads to a reduction in the Schottky barrier height. To verify the same, we have re-derive a function H(I) depending on the current of the diode from equation (1), which is expressed as :

$$H\,(I) = V - \frac{\eta kT}{q}\ln\frac{I_{SD}}{SA^{*}T^{2}} = \eta\,\Phi_B + I_{SD}R_S \quad \text{-----equation (2)}$$

The primary consideration behind deriving H(I) is that, a linear fit of plot between H(I) versus I_{SD} gives a straight line. The slope of this straight line gives the value of series resistance of the diode, while the intercept is equal to $\eta\varphi_{SB}$. Now we can easily calculate the value of φ_{SB} from the η value derived from ln (I)-V plot. A very high series resistance of 5978 kΩ and a SBH of 0.57 eV is obtained. A higher value anomalous to our previous assumption, therefore further investigations Schottky-diode parameters extraction which are based on high temperature I-V characteristics is required. A φ_{SB} the SBH value of 0.57 eV hints to the fact that the fabricated devices show a rectifying behavior at room temperature. This implies that the diode current is still an exponential function of Schottky-barrier height and thermionic emission is the dominant transport mechanism for the fabricated sensor. This shows that CO sensor based on this Schottky diode can sense CO even at room temperature as even a minimal variation in SBH after exposure of sensor at room temperature can bring an exponential and measurable change in diode current. Therefore, this parametric analysis based on measured electrical response of the device is quite helpful towards development of low-cost room temperature CO sensor.

5.4 Conclusion

In summary, a significant milestone has been achieved through the development of a highly sensitive CO gas sensor capable of detecting minute concentrations (LOD) down to 0.447 ppb at room temperature. This accomplishment was realized by leveraging the PFPT polymer as the sensing material. The sensor's selectivity has been thoroughly evaluated, affirming its robust performance. Notably, this device exhibits a remarkable response (%) when detecting CO gas, indicating its efficacy in this specific application. Beyond CO detection, comprehensive tests involving various VOCs and CO_2

have been conducted, thereby expanding the sensor's versatility and potential range of applications. Furthermore, this research delved into the characterization of Schottky barrier diode parameters, yielding insightful values for the η=1.7, φ_{SB}=0.57 eV, and Rs =5978 kΩ. These findings were derived through mathematical modelling techniques, enriching our understanding of polymer diode performance in sensing applications. The derivation of key Schottky diode parameters underscores the scientific rigor of this approach. Ultimately, we present a printed, cost-effective, and remarkably sensitive solution for CO sensing, which highlights the immense potential of PFPT polymer-based sensor technology.

References

(1) Onyancha, R. B.; Ukhurebor, K. E.; Aigbe, U. O.; Osibote, O. A.; Kusuma, H. S.; Darmokoesoemo, H.; Balogun, V. A. A Systematic Review on the Detection and Monitoring of Toxic Gases Using Carbon Nanotube-Based Biosensors. Sens. BioSensing Res. 2021, 34 (100463), 100463.

(2) Saxena, P.; Shukla, P. A Review on Recent Developments and Advances in Environmental Gas Sensors to Monitor Toxic Gas Pollutants. Environ. Prog. Sustain. Energy 2023, 42 (5).

(3) Bibi, S.; Ullah, H.; Ahmad, S. M.; Ali Shah, A.-U.-H.; Bilal, S.; Tahir, A. A.; Ayub, K. Molecular and Electronic Structure Elucidation of Polypyrrole Gas Sensors. J. Phys. Chem. C Nanomater. Interfaces 2015, 119 (28), 15994–16003.

(4) Ming-Ru, Y.; Ren-Jang, W.; Murthy, C. Effect of 'Pt' Loading in ZnO–CuO Hetero-Junction Material Sensing Carbon Monoxide at Room Temperature. Sens. Actuators B Chem. 2011, 153 (2), 321–328.

(5) Zhang, D.; Sun, Y.; Jiang, C.; Yao, Y.; Wang, D.; Zhang, Y. Room-Temperature Highly Sensitive CO Gas Sensor Based on Ag-Loaded Zinc Oxide/Molybdenum Disulfide Ternary Nanocomposite and Its Sensing Properties. Sens. Actuators B Chem. 2017, 253, 1120–1128.

(6) Liu, X.; Li, N.; Li, M.; Chen, H.; Zhang, N.; Wang, Y.; Zheng, K. Recent Progress in Fluorescent Probes for Detection of Carbonyl Species: Formaldehyde, Carbon Monoxide and Phosgene. Coord. Chem. Rev. 2020, 404 (213109), 213109.

(7) Basu, A. K.; Chauhan, P. S.; Awasthi, M.; Bhattacharya, S. α-Fe2O3 Loaded rGO Nanosheets Based Fast Response/Recovery CO Gas Sensor at Room Temperature. Appl. Surf. Sci. 2019, 465, 56–66.

(8) Hjiri, M.; El Mir, L.; Leonardi, S. G.; Pistone, A.; Mavilia, L.; Neri, G. Al-Doped ZnO for Highly Sensitive CO Gas Sensors. Sens. Actuators B Chem. 2014, 196, 413–420.

(9) Majder-Łopatka, M.; Węsierski, T.; Dmochowska, A.; Salamonowicz, Z.; Polańczyk, A. The Influence of Hydrogen on the Indications of the Electrochemical Carbon Monoxide Sensors. Sustainability 2019, 12 (1), 14

(10) Dey, S.; Dhal, G. C. Materials Progress in the Control of CO and CO2 Emission at Ambient Conditions: An Overview. Mater. Sci. Energy Technol. 2019, 2 (3), 607–623.

(11) Luo, N.; Zhang, B.; Zhang, D.; Xu, J. Enhanced CO Sensing Properties of Pd Modified ZnO Porous Nanosheets. Chin. Chem. Lett. 2020, 31 (8), 2033–2036.

(12) Neethirajan, S.; Jayas, D. S.; Sadistap, S. Carbon Dioxide (CO2) Sensors for the Agri-Food Industry—A Review. Food Bioproc. Tech. 2009, 2 (2), 115–121.

(13) Molina, A.; Escobar-Barrios, V.; Oliva, J. A Review on Hybrid and Flexible CO2 Gas Sensors. Synth. Met. 2020, 270 (116602), 116602.

(14) Onyancha, R. B.; Ukhurebor, K. E.; Aigbe, U. O.; Osibote, O. A.; Kusuma, H. S.; Darmokoesoemo, H.; Balogun, V. A. A Systematic Review on the Detection and Monitoring of Toxic Gases Using Carbon Nanotube-Based Biosensors. Sens. BioSensing Res. 2021, 34 (100463), 100463.

(15) Wang, C.; Wang, Y.; Yang, Z.; Hu, N. Review of Recent Progress on Graphene-Based Composite Gas Sensors. Ceram. Int. 2021, 47 (12), 16367–16384.

(16) Gao, N.; Yu, J.; Tian, Q.; Shi, J.; Zhang, M.; Chen, S.; Zang, L. Application of PEDOT:PSS and Its Composites in Electrochemical and Electronic Chemosensors. Chemosensors (Basel) 2021, 9 (4), 79.

(17) Graef, E. W.; Munje, R. D.; Prasad, S. A Robust Electrochemical CO2 Sensor Utilizing Room Temperature Ionic Liquids. IEEE Trans. Nanotechnol. 2017, 16 (5), 826–831.

(18) Wu, M.; Hou, S.; Yu, X.; Yu, J. Recent Progress in Chemical Gas Sensors Based on Organic Thin Film Transistors. J. Mater. Chem. C Mater. Opt. Electron. Devices 2020, 8 (39), 13482–13500.

(19) Rebber, M.; Willa, C.; Koziej, D. Organic-Inorganic Hybrids for CO2 Sensing, Separation and Conversion. Nanoscale Horiz 2020, 5 (3), 431–453.

(20) Ying, S.; Ma, Z.; Zhou, Z.; Tao, R.; Yan, K.; Xin, M.; Li, Y.; Pan, L.; Shi, Y. Device Based on Polymer Schottky Junctions and Their Applications: A Review. IEEE Access 2020, 8, 189646–189660.

(21) Meng, J.; Li, Z. Schottky-Contacted Nanowire Sensors. Adv. Mater. 2020, 32 (28), e2000130.

(22) Mathew, M.; Rout, C. S. Schottky Diodes Based on 2D Materials for Environmental Gas Monitoring: A Review on Emerging Trends, Recent Developments and Future Perspectives. J. Mater. Chem. C Mater. Opt. Electron. Devices 2021, 9 (2), 395–416.

Appendix

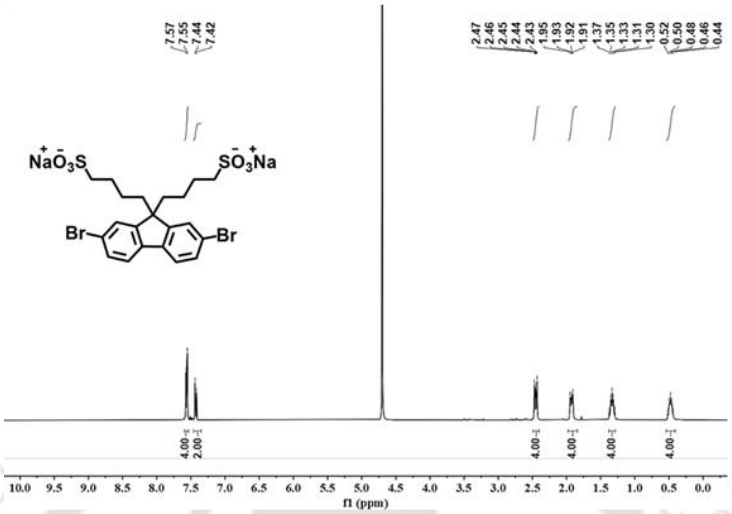

Figure A5.1: ^{1}H NMR of M.

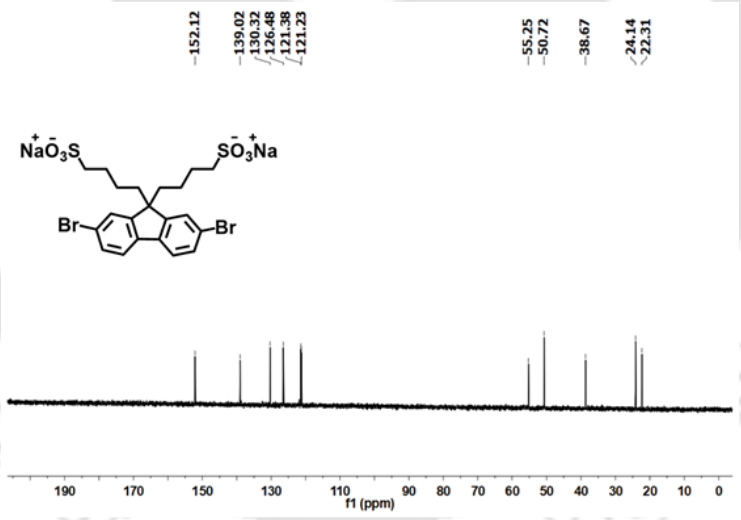

Figure A5.2: ^{13}C NMR of M.

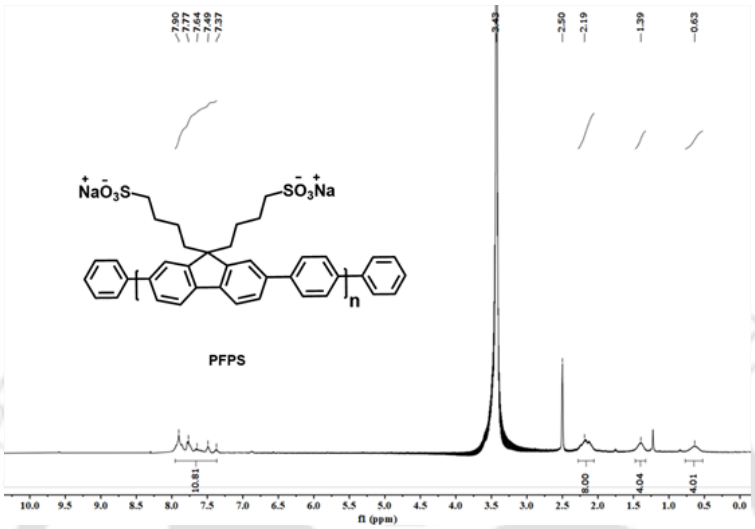

Figure A5.3: ^{1}H NMR of PFPT.

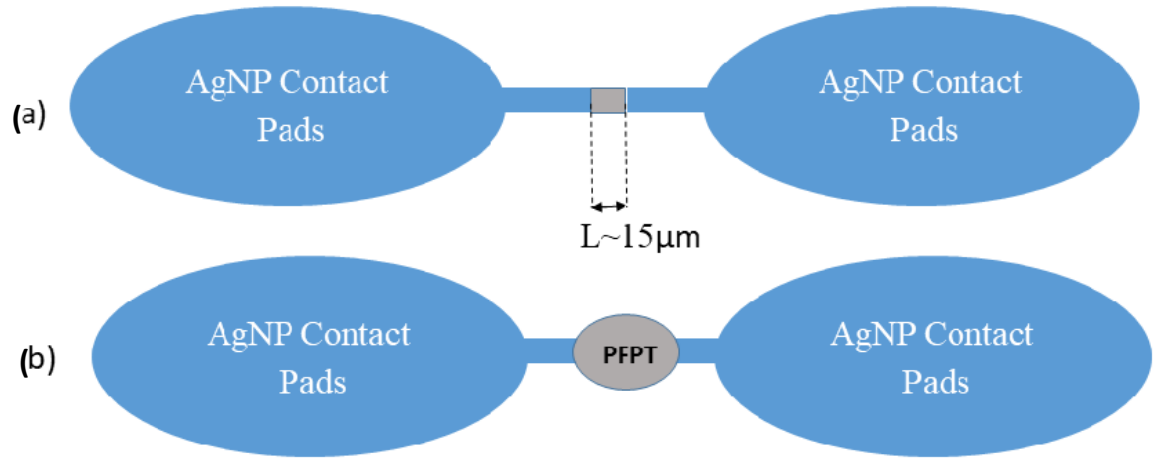

Figure A5.4: (a) Printed device with channel gap ~15 µm and (b) Printed device after PFPT polymer drop-casted.

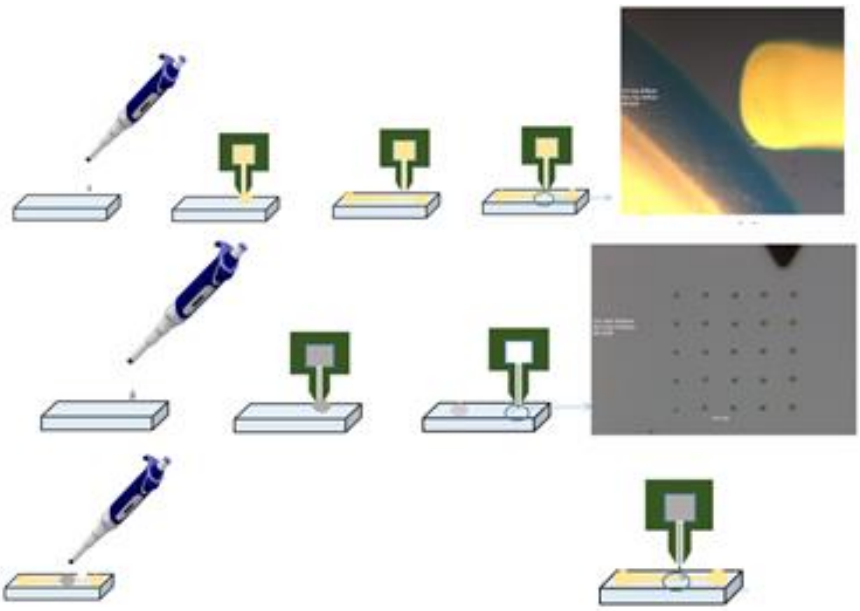

Figure A5.5: Fabrication steps of printed device**.**

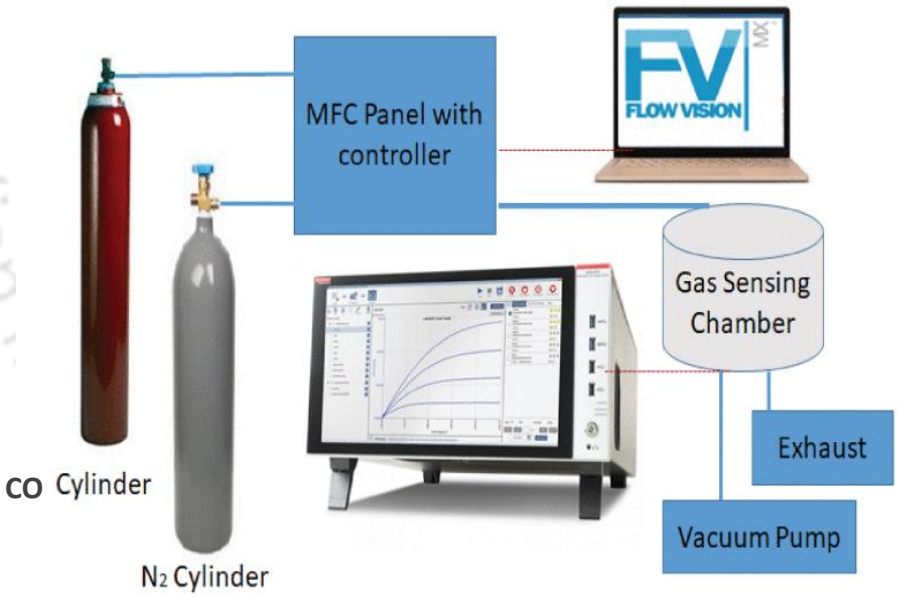

Figure A5.6: Gas sensing chamber set-up with 4200A SCS (Semiconductor Characterization System).

[This page was intentionally left blank]

Outcomes

Publications

1. **Yathirajula, R. B**, Gupta, R. K, M Afroz, M. A , Choudhury, A, Iyer, P. K., Modulating carrier injection through rational control of hole transport layer for perovskite light-emitting diodes.[Published: Journal of Materials Science: Materials in Electronics, Springer, 03, 2023. (https://doi.org/10.1007/s10854-023-10066-w)
2. **Yathirajula, R. B**, Gupta, R. K, M Afroz, M. A , Choudhury, A, H. Baishya, Iyer, P. K., Dual hole transport layer facilitated efficient perovskite light emitting diode Published :physica status solidi (a). (2023). (https://doi.org/10.1002/pssa.202300247)
3. **Yathirajula, R. B**, A. S. Tanwar, S Raveesh, T.T. Daniel, Iyer, P. K., Conjugated PFIM Polymer-based High Sensitive Ammonia Electrical Sensor Fabricated Using Lithography and Schottky Barrier Diode Modeling. [Manuscript Prepared].
4. **Yathirajula, R. B**, Zehra N, S Raveesh, T. T. Daniel, Iyer, P. K., Printed PFPS Polymer based CO Electrical Sensor with Schottky Diode Mathematical Modelling. [Manuscript Prepared].
5. **Yathirajula, R. B**, Chanu A, Sharma T, S Raveesh Iyer, P. K., Printed Novel Polymer based Ethane Electrical Sensor with Schottky Barrier Diode Modeling.[Manuscript Under Preparation].
6. **Yathirajula, R. B**, Adil L. R, Chanu A, S Raveesh Iyer, P. K., Novel Monomer based H_2O_2 Electrical Sensor with Schottky Barrier Diode Modeling. [Manuscript Under Preparation].
7. Murananand P**, Yathirajula, R. B**, Alam A , Iyer, P. K., Fabrication of Novel Blue Organic Light Emitting Diodes with Novel Monomers [Manuscript Under Preparation].
8. Arup K**, Yathirajula, R. B**, Bhaiya B , Iyer, P. K, G K Murthy Fabrication of Novel Blue Organic Light Emitting Diodes with Novel Monomer. [Manuscript Under Communication].
9. Singh R, **Yathirajula, R. B**, Himangshu Baishya S Raveesh, Iyer, P. K., Dual Application of organe OLED and CO_2 Electrical Sensor with novel mono-CS monomer. [Manuscript Under Communication].
10. Das, D., Gopikrishna, P., Barman, D., **Yathirajula, R.B**. and Iyer, P.K., 2022. Substantial efficiency enhancement in solution processed phosphorescent light emitting diode with polymer host: Efficient optimization of charge balance and processing conditions. (Journal of Physics and Chemistry of Solids, p.110577).
11. Arunagirinathan R. N, Hossain M, **Yathirajula, R.B**, Iyer, P. K., Compliance and electroforming free analog resistive switching device mimicking a biological synapse through the ion migration in a polymer memory device. (Under Communication)
12. Mondal, S.; Arunagirinathan R. N .; **Yathirajula, R. B**.; Methi, I.; Iyer, P. K.,Chapter-2: Emerging Technology for point -of-care diagnostics: Recent Developments; (D.O.I. 10.1016/B978-0-323-85725-3.00021-0; Elsevier: 2022).

13. Sarala, L.; **Yathirajula, R.B**.; Gopikrishna, P.; Elaiyappilla, E.; Bella, A.; S, M. N.; Iyer, P. K**.** Johnson P. M.; Pronounced Luminescence Efficiency and Thermal Stability of Small Imidazole Architect 2-[1, 4, 5-triphenyl-1H-imidazol-2-yl] phenol for Efficient Non-doped Blue OLEDs. (*Journal of Photochemistry & Photobiology A: Chemistry,* **[2018]**, *365*, 232-237).

14. Das, D., Gopikrishna, P., Barman, D., **Yathirajula, R.B**. and Iyer, P.K., 2019. White light emitting diode based on purely organic fluorescent to modern thermally activated delayed fluorescence (TADF) and perovskite materials. (Nano convergence, 6(1), pp.1-28).

15. Gupta, R. K.; Rahul Narasimhan Arunagirinathan.; Afroz, M. A.; Garai, R.; Choudhury, A.; Hossain, M.; **Yathirajula, R. B**.; Iyer, P. K., Chapter 4 - Functional materials for various organic electronic devices. In Chemical Solution Synthesis for Materials Design and Thin Film Device Applications, Das, S.; Dhara, S., Eds.(Elsevier: 2021; pp 119-165).

Conference and Workshop

- Attended INUP Familiarization workshop on Nanofabrication Technologies during 28-29, January 2019 at NIT Silchar.
- Training program on Basis VLSI Design training Tools like NGSPICE, Magic VLSI and Mentor Graphics on 25, September 2019 at IIT Guwahati.
- Attended 5th National Workshop on MEMS/NEMS and Theranostic Devices (NWNTD2017) organized by Centre for Nanotechnology, IIT Guwahati, Assam during February 21-23, 2017.
- Attended Research Conclave during 14-17 March 2019 at IIT Guwahati.
- Attended National Conference on ASTM 2018 at IIT(ISM) Dhanbad during March 14-16, 2018.
- Attended 5th International Conference on Advanced Nanomaterial's and nanotechnology (ICANN) during 18-21 Dec 2017 at IIT Guwahati.
- Attended six days "short course on Flexible Electronics" organized jointly by Samtel Centre for Display Technology, IIT Kanpur and Ministry of Electronics & Information Technology (MeitY) Govt. of India, Kanpur, UP, July 3-8, 2016.
- Attended LATEX work shop during 1-2 April 2018 at IIT Guwahati.
- Attended MATLAB course during 30-31st March 2018 at IIT Guwahati
- Attended 7th International Conference on Advanced Nanomaterial's and nanotechnology (ICANN) during 14-17, Dec 2021 at IIT Guwahati.
- Attended GIAN Course titled "Modeling and Simulation in Energy Storage" January 3 - 9, 2022 at IIT Guwahati.
- Attended National workshop on "Implementation of MSME Innovative Scheme-Intellectual Property Right (IPR) "on 22nd February, 2023 at IIT Guwahati with collaboration with MSME, Govt.of India.
- Attended National workshop on "Introduction to Machine Learning with Python "on 26th March, 2023 at IIT Guwahati offered by IEEE Student Branch, IITG.
- Attended and Presented an Oral Talk at Research & Industrial Conclave- Integration'23 14th to 16th May, 2023 at IIT Guwahati with collaboration with IIT Guwahati Research Park.
- Attended 8th International Conference on Advanced Nanomaterial's and nanotechnology (ICANN) during November 29th, 30th and 1st December, 2023 at IIT Guwahati.
- Attended IEEE Sensor Council Winter School on MEMS and Nano Devices" December 4 - 5, 2023 at IIT Guwahati, under IEEE chapter Kolkata region, India.

Awards

- BEST POSTER AWARD in "India Nano-electronic User Program-Idea to Innovation (INUP-i2i)", at National Work Shop, April, 2022.
- BEST ORAL PRESENTATION AWARD (RSC Sponsored) in 8th International Conference on Advanced Nanomaterial's and nanotechnology (ICANN-2023) during November 29th, 30th and 1st December,2023. (@ International Conference).